

UCSF

UC San Francisco Electronic Theses and Dissertations

Title

Functional roles of chromatin recruitment to the nuclear periphery

Permalink

<https://escholarship.org/uc/item/9tv1b0dm>

Author

Marin, Harold Cesar

Publication Date

2024

Peer reviewed|Thesis/dissertation

Functional roles of chromatin recruitment to the nuclear periphery

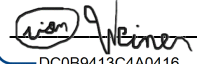
by
Harold Cesar Marin


DISSERTATION
Submitted in partial satisfaction of the requirements for degree of
DOCTOR OF PHILOSOPHY

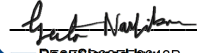
in
Biochemistry and Molecular Biology

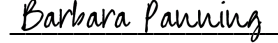
in the
GRADUATE DIVISION
of the
UNIVERSITY OF CALIFORNIA, SAN FRANCISCO

Approved:

DocuSigned by:

DC0B9413C4A0416... Orion Weiner
Chair

DocuSigned by:

DC0B9413C4A0416... Abigail Buchwalter

DocuSigned by:

DC0B9413C4A0416... Geeta Narlikar

DocuSigned by:

B18F20197C95417... Barbara Panning

Committee Members

Copyright 2024

by

Harold Cesar Marin

ALL RIGHTS RESERVED

Para mi abuelita Virginia Roman Esquivel, my favorite person in the world

ACKNOWLEDGEMENTS

First and foremost, I would like to acknowledge my thesis advisor Dr. Abigail (Abby) Buchwalter PhD. This PhD could not have happened without all your unwavering support all these years. Being your first graduate student means the world to me. You have always believed in my abilities and my potential for growth. I have learned many things from you but one that I want to highlight is your intentional mentorship. This is a skill that I will carry on for the rest of my life. Thank you.

I would like to thank my thesis committee Dr. Orion Weiner PhD, Dr. Geeta Narlikar PhD, and Dr. Barbara Panning PhD for our insightful scientific discussions. I always felt better about my abilities as a scientist after each committee meeting. You taught me to think critically but also ambitiously, and to believe in my strongest data.

I am very grateful to the members of the Buchwalter lab: Yewande, Katie, Jess, Tracy, Charlie, Eric, and Valeria. Special shout out to former members John and Yana, and our neighbors from Dr. Elphege Nora's lab, extra shout out to Elphege, Karissa, Erika and Rini. What a ride. We have had quite the dynamic range of experiences at UCSF, but I would do it again if it meant meeting all of you all over again.

I would like to thank my family both here and in Peru for all their support in raising me and supporting my goals. I dedicate this dissertation to my abuelita Virginia who helped my parents with raising me since the day I was born and who passed away while I was in graduate school. Abuelita visited me at UCSF a year before I started graduate school. Abuelita was the most compassionate person I knew, and I try to embrace this quality in my own life. She was also a great cook and I try to embrace that as well. I would also like to acknowledge my paternal grandparents: abuelita Raquel who also helped raise me, and abuelito Rodolfo, who passed away while I was in graduate school and without whom I would not have been able to immigrate to the United States.

Next, I would like to acknowledge my parents, Juan and Carmen, although I would never refer to them by their first names. My parents have always believed in me, and I am thankful for all their sacrifices and patience in raising me. My dad taught me patience from a very early age, always repeating the phrase “las cosas apuradas salen mal” (“rushed things turn out bad”) which fits quite well to my graduate school experience. Thank you for this virtue, Pa. I believe I get my drive from my mom. My mom always pushed me to try new experiences like riding public transit to school in Lima by myself at the age of 7. As a first-generation immigrant, the first in my family to graduate from college in the U.S., and the first to obtain a PhD in my extended family, I have had to navigate many things by myself without a familiar roadmap. But I have learned to keep my own drive just like my mom’s drive to achieve her goals. This year she also graduated as a certified X-ray technician which has been her life-long passion. Thank you and congratulations to you too, Ma. Next, I would like to thank my brother Jeffrey and my primos Andre and Renzo. I am very fortunate to have you all in my life. Our game nights are always happy times, especially when we could not see each other during pandemic times. I would also like to thank my cousins here: Cami, Fati, Nena. And my cousins in Peru: Liz, Kadel and Jorge (and his daughter Dayana) for keeping me connected to my family over there.

I am thankful for both sides of my extended family. First, I want to thank my paternal family who all except for tio Enrique lived in the same city when I was growing up in the U.S (la colonia Marin): tia Sara, tia Doris, tia Chita, tio Rodo, and tio Oscar. Tio Rodo passed away right before I started graduate school and I miss him dearly. Special shout out to my second parents, tia Sara and to Wil, who helped raise me after I moved to the U.S. Second, I want to thank my maternal family who all still live in Peru: tia Yrma, tia Esther, tio Ernesto, and tio Efrain. Tio Efrain passed away when I was in college, but I always remember him as my adventurous uncle who lived all over South America. Special shout out to tia Yrma who is like a second mother. Tia Yrma helped raise me, taught me discipline and my multiplication tables. Thank you, family; you have all taught me the positive value of growing up around a big community.

I would like to acknowledge the UCSF community that I found here. First, I would like to acknowledge Dr. D'Anne Duncan PhD who made me feel welcomed from day one of graduate school and supported me throughout my time here. Next, I would like to acknowledge Alece Alderson, Tiffany Lam and the FG2C community which always hosted great community events and made me feel cared for. I would like to thank members of the SACNAS chapter at UCSF who made me feel welcomed and reminded me of my Latino identity. I would like to thank the Tetrad program coordinators Toni Hurley, Danny Dam, Veena Mohan and Billy Luh.

I would like to acknowledge my former and current mentors: Abigail Zoger, Nick Anast, Beth Johnstone, Dr. Mark McCormick PhD, Dr. Francis (Frank) McNally PhD, Dr. Michelle Panzica PhD, Dr. David (Dave) Toczyski PhD, Dr. Frances Hundley PhD, and Dr. Carrie Graham PhD. All of you had a positive impact on my journey as a scientist.

I would like to express my most extra acknowledgments to the friends that I made here at UCSF. Special shout out to Dr. Jesslyn Park PhD for being the kindest person I know, Dr. Evelyn Hernandez PhD for being so cool that she joined my family and now we will never be apart, Dr. Jocelyne (Jocy) Lopez PhD for always keeping it real and for being there for me during my quals studying rut, Dr. Natasha Puri PhD for all the dance parties, soon-to-be PhD Hayden Saunders for all the life and sports talks, and Dr. Nilsa La Cunza PhD not only for being the other Peruvian graduate student at UCSF but also for being my friend.

I would also like to acknowledge non-UCSF friends that have supported me during my grad school years: Peter, Lovepreet, Sharendeeep, Lily, and Kitan.

Finally, I would like to acknowledge my fiancée Dr. Shradha (Sony) Biradar DO MPH who has been with me since day one of my scientific journey, when I did not even know about graduate school. How poetic that you were there for me for my first lab meeting and now you are here at the culmination of my formal scientific training. You are the most important person in my life. Your ability to both hype me up and ground me have been very valuable for me before, during and probably after graduate school.

CONTRIBUTIONS

Chapter 2 is adapted from an unpublished manuscript with the following authors: Harold Marin, Eric Simental, Charlie Allen, Eric Martin, Barbara Panning, Bassem Al-Sady, and Abigail Buchwalter.

Chapter 3 is unpublished work including experiments performed with the help of Charlie Allen, Valeria Virrueta and Abigail Buchwalter.

Functional Roles of Chromatin Recruitment to the Nuclear Periphery

Harold Cesar Marin

ABSTRACT

The eukaryotic nucleus houses deoxyribonucleic acid (DNA) along with scaffolding proteins which together form chromatin. Cells organize their chromatin as transcriptionally silent, compacted heterochromatin and active, relaxed euchromatin. Heterochromatin is enriched at the nuclear periphery in metazoans and peripheral position correlates with transcriptional repression. Here, we remove three nuclear lamins and lamin B receptor (LBR) in mouse embryonic stem cells (mESCs) and show that heterochromatin detaches from the nuclear periphery. Heterochromatic loci marked by histone H3 lysine 9 di-methylation (H3K9me₂) are enriched at the nuclear periphery; however, the effect of spatial position on H3K9me₂-modified genes has not been defined. Chapter 1 is a brief overview of genome organization and the major players studied in this dissertation. Chapter 2 focuses on the effect of heterochromatin spatial position on the transcription and chromatin state of H3K9me₂-modified genes in naïve mESCs and differentiated Epiblast-like cells (EpiLCs). Chapter 3 shows preliminary work on the effects of heterochromatin spatial position on nuclear shape, on heterochromatin-associated factors such as H3K9me₃, HP1 α and HP1 β , on a degron system to rapidly deplete LBR, and on structure-function rescue experiments to identify regions in LBR that are important for peripheral enrichment of H3K9me₂. This work shows that the nuclear periphery controls the spatial position and repressive functions H3K9me₂, as well as potentially other heterochromatin marks.

TABLE OF CONTENTS

| | |
|--|-----------|
| CHAPTER 1: INTRODUCTION | 1 |
| The Spatial Organization of the Genome | 1 |
| The Nuclear Periphery | 2 |
| Histone H3 Lysine 9 Methylation | 4 |
| CHAPTER 2: THE NUCLEAR PERIPHERY CONFERS REPRESSION ON H3K9ME2- MARKED GENES AND TRANSPOSONS TO SHAPE CELL FATE | 6 |
| Abstract | 6 |
| Introduction | 6 |
| Results | 8 |
| The Lamins and LBR Recruit Heterochromatin to the Nuclear Periphery in Pluripotent Cells | 8 |
| The Genomic Distribution of H3K9me2 is Preserved in the Absence of the Lamins and LBR..... | 10 |
| Spatial Displacement Dysregulates H3K9me2-marked Genes | 11 |
| Heterochromatin Displacement Causes Widespread De-repression of Transposons..... | 12 |
| Heterochromatin Positioning Enables the Transition from Naïve to Primed Pluripotency | 14 |
| Heterochromatin Positioning Influences Remodeling of H3K9me2 in Primed Pluripotency..... | 16 |
| Heterochromatin Positioning Silences Transposons and Alternative Cell Fate Genes in EpiLCs | 17 |
| Discussion | 19 |
| The Lamins and LBR Exert Broad Influence on Heterochromatin Organization and Function | 19 |
| The Nuclear Periphery Influences the Repressive Capacity of H3K9me2 | 20 |
| The Nuclear Periphery Maintains Repression of Transposons | 21 |
| The Nuclear Periphery Regulates H3K9me2 During Differentiation..... | 23 |
| Figures | 25 |
| Materials and Methods | 50 |

| | |
|---|-----------|
| Generation of Knockout and miR-E Expressing mESCs..... | 50 |
| mESC culture and EpiLC differentiation | 51 |
| RNA Isolation and Library Preparation for RNA-seq | 52 |
| RNA-seq Analysis..... | 53 |
| CUT&RUN and Library Preparation | 54 |
| CUT&RUN Analysis..... | 55 |
| Immunoblot Assay | 56 |
| Cholesterol Quantification Assay..... | 57 |
| Immunofluorescence and Halo Tag Staining..... | 57 |
| Image Acquisition and Analysis | 58 |
| Transmission Electron Microscopy and Image Analysis..... | 58 |
| Data Availability | 59 |
| CHAPTER 3: PRELIMINARY RESULTS, SPECULATIONS, AND FUTURE DIRECTIONS | 60 |
| Abstract | 60 |
| Results | 60 |
| Nuclear Size and Shape in Lamin + Lbr KO mESCs..... | 60 |
| Measurements of H3K9me3, HP1 α And HP1 β foci in Lamin + Lbr Knockout mESCs..... | 61 |
| Tagging the Endogenous Locus of LBR with the dTAG Degron System..... | 62 |
| H3K9me2 Radial Distribution Rescued by Different LBR Constructs..... | 63 |
| Discussion, Speculations and Future Directions | 63 |
| Materials and Methods | 66 |
| Immunofluorescence | 66 |
| Image Acquisition and Analysis | 67 |
| Immunoblot assay | 67 |
| Endogenous Tagging of LBR with Inducible dTAG Degron | 67 |

| | |
|-------------------------|-----------|
| Figures | 70 |
| REFERENCES | 78 |

LIST OF FIGURES

Chapter 2

| | |
|--|----|
| Figure 1. The lamins and LBR localize H3K9me2-marked chromatin to the nuclear periphery in mESCs. | 25 |
| Figure 2. Genomic distribution of H3K9me2 is preserved after removal of the lamins and LBR. | 27 |
| Figure 3. Removal of the lamins and LBR derepresses H3K9me2-marked and other genes. .. | 28 |
| Figure 4. Ablation of the lamins and LBR allows pervasive transcription of transposons in spite of H3K9me2 modification. | 30 |
| Figure 5. Heterochromatin positioning by the lamins and LBR is essential for EpiLC survival.. | 31 |
| Figure 6. Abnormal deposition of H3K9me2 in Lamin + LBR KO EpiLCs. | 33 |
| Figure 7. Removal of the lamins and LBR derepresses genes and transposons and impairs lineage restriction in EpiLCs. | 35 |
| Supplementary Figure 1. Validation of knockout mESCs. | 37 |
| Supplementary Figure 2. Microscopy of knockout mESCs. | 38 |
| Supplementary Figure 3. Displacement of H3K9me2 from the nuclear periphery is reversible. | 39 |
| Supplementary Figure 4. Replicate clustering and analysis of H3K9me2 CUT & RUN in mESCs. | 41 |
| Supplementary Figure 5. Analysis of transcription after inducible knockdown of LBR in mESCs. | 43 |
| Supplementary Figure 6. Additional phenotypic profiling of mESCs. | 44 |
| Supplementary Figure 7. Fluorescence and electron microscopy of EpiLCs. | 45 |
| Supplementary Figure 8. Uncropped TEM images of WT, TKO, LBRKO, and QKO EpiLCs. .. | 46 |
| Supplementary Figure 9. Replicate clustering and analysis of H3K9me2 CUT & RUN in EpiLCs. | 47 |

Supplementary Figure 10. Analysis of TE expression in WT, TKO, LBRKO, and QKO EpiLCs. 49

Chapter 3

Figure 1. Nuclear shape analysis in Lamins + Lbr KO mESCs and EpiLCs after plating for 8 hours. 70

Figure 2. Nuclear shape analysis in Lamins + Lbr KO mESCs after plating for 24 hours..... 72

Figure 3. H3K9me3 foci analysis. 73

Figure 4. HP1 α and HP1 β foci analysis. 74

Figure 5. N-terminal tagging of FKBPV degron to the endogenous locus of mouse LBR. 75

Figure 6. H3K9me2 radial distribution in Lamin + Lbr quadruple knockout mESCs stably expressing different LBR constructs. 76

LIST OF ABBREVIATIONS

EpiLC: Epiblast-like cell

H3K9me2: Di-methylated Histone H3 at lysine 9

H3K9me3: Tri-methylated Histone H3 at lysine 9

H4K20me2: Di-methylated Histone H4 at lysine 20

HP1 α : Heterochromatin protein alpha isoform

HP1 β : Heterochromatin protein beta isoform

HP1 γ : Heterochromatin protein gamma isoform

LAD: Lamina-associated domain

LBR: Lamin B Receptor

mESC: mouse embryonic stem cell

RNAi: RNA interference

TEM: Transmission electron microscopy

CHAPTER 1: INTRODUCTION

The Spatial Organization of the Genome

The nucleus is a defining feature of all eukaryotic cells. As the largest organelle of the cell, the nucleus also contains the largest biological macromolecule, the genome.

Compartmentalization of eukaryotic genomes away from the cytoplasm leads to new regulatory layers of gene expression when compared to prokaryotic genomes, from the decoupling of transcription from translation to the spatial organization of chromosomes. Cell biologists have always had a keen eye for studying subcellular structures and the genome is not exempt from its cellular environment.

There are many levels of genome organization. The nucleosome is the smallest unit of genome organization which consists of 147bp of DNA wrapped around an octamer, barrel-like structure composed of two copies of core histone proteins H2A, H2B, H3, and H4¹. In a strand of linear DNA, multiple nucleosomes form a chromatin fiber which display different levels of compaction depending on different chemical modifications on their histones. The chromatin fiber exists in two states of compaction: heterochromatin and euchromatin. Coined by the German scientist Emil Heitz, heterochromatin is classically defined as compacted, transcriptionally inactive chromatin, while euchromatin refers to uncompacted, transcriptionally active chromatin². Ideas on large-scale genome organization began to be published at the turn of the 19th century but these ideas lacked rigorous testing until the 1970s. Through new technologies such as laser microbeams and 3-dimensional imaging of whole chromosomes, evidence began to support a model of chromosomes occupying distinct territories inside the nucleus (reviewed in Cremer et al., 1993)³. Currently, it is widely accepted that the eukaryotic genome is not randomly organized.

The Nuclear Periphery

The nucleus is a double phospholipid bilayer. The outer membrane is contiguous with the endoplasmic reticulum, and it joins the inner membrane through the nuclear pores. Facing the inside of the nucleus, the inner membrane has many proteins and complexes that are enriched on its surface. In mammals, one of these complexes is the nuclear lamina which is composed of a meshwork of intermediate proteins called lamins. The general structure of lamin proteins is characterized by a polypeptide containing an N-terminal head domain, followed by a rod domain composed of two alpha-helical coiled-coil domains separated by two short flexible linker sequence, a nuclear localization sequence, an immunoglobulin-like Ig beta globular fold domain, and an unstructured C-terminal domain⁴. Mammals have four lamin isoforms encoded by three lamin genes, Lamin B1 encoded by the *LMNB1* gene, Lamin B2 encoded by the *LMNB2* gene, and the splice isoforms Lamin A and Lamin C encoded by the *LMNA* gene⁴.

Many eukaryotic nuclei have a layer of heterochromatin beneath their inner nuclear membrane. Arguably, this might be a universal phenomenon as it has been observed in humans⁵, mouse⁶, plants⁷, and even the slime mold amoeba⁸. Over the years, it has become apparent that this layer of peripheral heterochromatin is recruited by proteins that reside on or beneath the inner nuclear membrane⁹.

The nuclear lamina associates with peripheral heterochromatin⁶. Lamins can bind specific DNA sequences and histone proteins *in vitro*¹⁰, but which specific regions of the genome bound to the nuclear lamina remained a mystery until the early 2000s. Using a technology called DamID, the genomic regions that associate with the nuclear lamina were first identified in *Drosophila* and then in human cells^{11,12}. These so-called "lamina associated domains," or LADs, harbor many markers of heterochromatin such as low transcription and high H3K9me2 and H3K9me3^{12,13}. LADs vary across cell types and dynamically shift as cells differentiate¹⁴. The molecular mechanism of heterochromatin recruitment to the nuclear periphery is unknown. The nuclear lamina interacts with other nuclear membrane proteins which have also been linked to

genome organization⁹. In mammals, it has been shown that Lamin A/C and Lamin B Receptor (LBR) recruit peripheral heterochromatin in a redundant manner although the molecular mechanism remains unknown¹⁵.

LBR is a lamina interacting protein that has roles in genome organization. First cloned in the late 1990s, LBR gets its name from biochemical studies that found it to preferentially bind B-type lamins over A-type lamins¹⁶. However, LBR has other binding partners of the nuclear envelope. The name “receptor” could be considered a misnomer as LBR has not been shown to have any roles in cell signaling. LBR is an eight-pass transmembrane protein of the inner nuclear membrane with an N-terminal domain that faces the nucleoplasm. This nucleoplasmic domain is structured in three parts: Tudor domain, arginine-serine rich (RS) domain, and a second globular domain (globular II domain). LBR’s transmembrane domain has C-14 sterol reductase activity which suggest a role in cholesterol synthesis. LBR is highly conserved in vertebrates, and it might have evolved in early metazoans as there are potential LBR orthologs in some invertebrate species although this analysis is limited by the lack of sequenced genomes^{17,18}.

LBR binds chromatin through its Tudor and Globular II domains. Tudor domains are classified by their ability to bind to methyl-arginine or methyl-lysine¹⁹. The domain gets its name from the *Tudor* gene in *Drosophila* which has 10 repeats of this domain. Homozygous mutations in the *Drosophila Tudor* gene result in maternal-effect lethality which inspired its naming from the many miscarriages of the wives of English king, Henry Tudor (a.k.a. Henry VIII)²⁰. Chromatin immunoprecipitation studies show that the nucleoplasmic domain of LBR can pull down H4K20me2 and H3K9me3 modified nucleosomes²¹ as well as the associated heterochromatin proteins HP1 α and HP1 γ ²². However, *in vitro* studies with modified histone peptides show that the nucleoplasmic domain of LBR binds H4K20me2 but not H3K9me2 nor H3K9me3, and that its Tudor domain is necessary for this binding²³. Interestingly, LBR’s Tudor domain alone is not sufficient for binding to H4K20me2 and can only bind unmodified histone H4²⁴ suggesting that

other parts of LBR's nucleoplasmic domain are required for binding to H4K20me2. LBR can bind the chromoshadow domain of HP1 isoforms through an HP1 binding motif in the globular II domain²⁵. All mammalian HP1 isoforms (HP1 α , HP1 β , and HP1 γ) can bind H3K9me2 and H3K9me3^{26,27} which provokes a potential model for linking LBR to the peripheral enrichment of LADs containing those histone marks. However, LBR's HP1-binding motif is a variant from the canonical sequence (PxVxL) and the motif varies between human (VxVxL) and mouse (LxVxL) LBR²⁸. Models that represent an LBR-HP1 complex recruiting H3K9me2/3 must reconcile these inconsistencies in binding motif variants and the role of H4K20me2 which has not been convincingly shown to be enriched at the nuclear periphery and is more associated with DNA repair²⁹. In summary, the nuclear periphery is a sub-compartment of the nucleus that harbors lamins and lamin-associated proteins that interact with heterochromatin factors.

Histone H3 Lysine 9 Methylation

Methylation of histone H3 lysine 9 is one of the hallmarks of heterochromatin. In mammals, this methylation is catalyzed by six different methyltransferases: Suv39h1, Suvh2, Setdb1 (or Eset1), Setdb2 (or Eset2), G9a (or Ehmt2), GLP (or Ehmt1)³⁰⁻³⁶. Suv39h1 and Suv39h2 are paralogs that perform redundant functions; single knockout mice are viable but double knockout mice have severely impaired viability³⁷ and either protein can methylate H3 histones at lysine 9 *in vitro*³⁰. Setdb1 and Setdb2 are also paralogs³⁴ but there are more studies on the role of Setdb1 in retrotransposon silencing^{32,33}. Moreover, double knockout of Setdb1 and Setdb2 does not reduce the global levels of H3K9 methylation, but it results in nuclear deformations as judged by Lamin B1 localization³⁸. G9a and GLP are obligate heterodimers and are both required for H3K9 di-methylation³⁶. Although biochemically G9a/GLP can methylate all the way to H3K9me3³⁹, they are primarily responsible for most of the H3K9me2 in the cell³⁶. H3K9me2 and H3K9me3 are widely considered repressive histone marks, but there is evidence from *S. pombe* that H3K9me2 is slightly less repressive than H3K9me3 and that H3K9me2 can co-occur with transcriptionally active histone marks⁴⁰. A compelling study dissected the

redundant and specific roles of H3K9 methyltransferases in heterochromatin formation, gene repression and transposon silencing by knocking out all six genes in mouse embryonic fibroblast cells³⁸. These sextuple knockout cells lack all H3K9 methylation states, lose their electron dense heterochromatin by transmission electron microscopy (TEM), and derepresses nearly all families of transposable elements. This demonstrates the critical role of H3K9 methylation in genome stability.

In mammals, there is increasing evidence for a specialized role of H3K9me2 in the recruitment of heterochromatin to the nuclear periphery. H3K9me2 can be visualized at the nuclear periphery by immunofluorescence while H3K9me3 does to a lesser extent⁴¹. Additionally, LADs correlate with H3K9me2 occupancy in the genome more than with H3K9me3¹³. Reduction of H3K9me2 levels by G9a RNAi or pharmacological inhibition of G9a/GLP releases several LADs from the nuclear periphery⁴². Targeting of endogenous loci with the catalytic domain of G9a moves them to the nuclear periphery⁴³. New studies that focus on perturbations of nuclear lamina proteins or H3K9 methyltransferases will be critical to uncover the role of H3K9me2 in heterochromatin recruitment to the nuclear periphery.

CHAPTER 2:

THE NUCLEAR PERIPHERY CONFERS REPRESSION ON H3K9ME2-MARKED GENES AND TRANSPOSONS TO SHAPE CELL FATE

Abstract

Heterochromatic loci marked by histone H3 lysine 9 dimethylation (H3K9me2) are enriched at the nuclear periphery in metazoans. While peripheral position correlates with transcriptional repression, the effect of spatial position on H3K9me2-modified genes has not been defined. Here, we remove three nuclear lamins and lamin B receptor (LBR) in mouse embryonic stem cells (mESCs) and show that heterochromatin detaches from the nuclear periphery. Quadruple knockout (QKO) mESCs sustain naïve pluripotency and maintain H3K9me2 across the genome but cannot repress H3K9me2-marked genes or transposons. QKO cells have impaired capacity to differentiate into epiblast-like cells (EpiLCs). While normal EpiLCs expand H3K9me2 across the genome, QKOs exhibit abnormal H3K9me2 patterning. QKO cells can exit naïve pluripotency and activate epiblast-stage genes but also aberrantly express markers of alternative fates, including primitive endoderm. We conclude that the nuclear periphery controls the spatial position, dynamic remodeling, and repressive capacity of H3K9me2 to shape cell fate decisions.

Introduction

Eukaryotic genomes are organized into compartments of transcriptionally active euchromatin and silent heterochromatin. Heterochromatin shapes cell fate decisions by restricting gene expression and safeguards genome integrity by inhibiting transposon activity⁴⁴. Across eukaryotes, heterochromatin is abundant at the nuclear periphery while euchromatin resides in the nuclear interior^{45–48}. In mammals, the peripheral position of heterochromatin is established in embryonic nuclei shortly after fertilization and before other features of genome folding, such as topologically associating domains, appear⁴⁹. The nuclear periphery appears to have an intrinsic and conserved capacity to repress transcription. In *S. pombe*, heterochromatin

recruitment to the nuclear periphery enables the long-term epigenetic memory of cell state by antagonizing nucleosome turnover⁵⁰. In mammals, artificial tethering of loci to the nuclear periphery induces silencing^{51–53}. Association to the nuclear periphery and transcriptional repression are strongly correlated, and many lineage-irrelevant genes are recruited to the nuclear periphery during differentiation processes^{54,55}. These observations have led to the prevailing model that peripheral heterochromatin positioning promotes the establishment of cell fate by repressing alternative fate genes. However, this model has not yet been tested, and the mechanism by which the nuclear periphery confers repression on associated chromatin remains unknown.

Recently, it has become clear that histone H3 lysine 9 di- and/or tri-methylation (H3K9me2/3) is uniquely enriched on peripheral heterochromatin in many eukaryotes^{50,56–59} and is required for the formation of this compartment^{59–61}. H3K9me2 is predominantly deposited by the heterodimeric G9a/GLP enzyme (also known as EHMT2 and EHMT1)^{62,63}. H3K9me2 promotes the repression of both genes and transposons^{62,64–68} and is essential for mammalian pre-implantation development^{62,63,67}. However, H3K9me2-modified chromatin is permissive to transcription in some contexts^{69–71}, which implies that H3K9me2 alone is not sufficient to induce repression.

The receptor proteins that tether H3K9me2/3-marked loci to the nuclear periphery vary across eukaryotes and include components of the inner nuclear membrane (INM) and of the nuclear lamina, a meshwork formed by lamin proteins that underlies the INM. For instance, the INM protein Amo1 tethers H3K9me3 to the nuclear periphery in *S. pombe*⁵⁰. In *C. elegans*, the INM protein CEC-4 tethers H3K9me2/3-marked chromatin in embryos but is dispensable for this process in differentiated tissues, perhaps due to compensation by other proteins^{56,72}. In mammals, the lamin isoform lamin A/C and the nuclear membrane protein lamin B receptor (LBR) each contribute to the spatial position of heterochromatin⁷³, although it is unknown whether they recognize H3K9me2/3. H3K9me2 is highly enriched in lamina-associated domains

(LADs) of chromatin in mammals^{57,61,74–76}, raising the possibility that the nuclear lamins and/or LBR control the peripheral positioning of heterochromatin bearing this modification.

Here, we disrupt the lamins and LBR in mouse embryonic stem cells (mESCs) to dissect the functions of heterochromatin positioning during early mammalian development. We show that these proteins control the spatial positioning of heterochromatin and discover that H3K9me2 is unable to effectively repress either transposons or lineage-specific genes when displaced from the nuclear periphery, indicating that heterochromatin positioning enhances the repression of H3K9me2-modified chromatin. Finally, we show that displacing heterochromatin from the nuclear periphery impairs the timely restriction of gene expression that shapes cell fate during differentiation.

Results

The Lamins and LBR Recruit Heterochromatin to the Nuclear Periphery in Pluripotent Cells

A strong correlation between LADs and H3K9me2-marked chromatin has been reported in a range of mammalian cell types^{57,76}. However, mESCs lacking all lamin isoforms are viable and pluripotent, retain peripheral heterochromatin positioning, and exhibit modest changes to genome folding and gene expression^{77–79}. We noted that both wild type (WT) and lamin triple knockout (TKO) mESCs cultured in naïve conditions (2i + LIF) express high levels of LBR which remains enriched at the nuclear periphery even in the absence of the lamin proteins in TKO mESCs (Fig. S1B), while H3K9me2-marked chromatin also remains enriched at the nuclear periphery in both WT and TKO mESCs (Fig. 1A-B). These observations led us to hypothesize that LBR sustains heterochromatin organization in this context⁷³, and to propose that lamin TKO mESCs are a useful sensitized system in which to dissect the functions of heterochromatin positioning in mammals.

We generated lamin + LBR quadruple knockout (QKO) and LBR knockout (LBR KO) mESCs by introducing frameshift indels into both alleles of the *Lbr* locus in lamin TKO mESCs and in WT littermate control mESCs, respectively (Fig. S1A, S1C-F). LBR KO, lamin TKO, and

lamin + LBR QKO mESCs are each viable, pluripotent, and exhibit normal mESC colony morphology, albeit with a modest decrease in proliferation rate in QKO mESCs (Figure S1G-I). We evaluated the effect of ablating the lamin and LBR proteins on the spatial organization of heterochromatin by quantifying the radial distribution of H3K9me2 (Fig. 1A-E, 1H) and compacted DNA (Fig. S2A-E), as well as by transmission electron microscopy (TEM) (Fig. 1I-M). These analyses revealed that H3K9me2-marked chromatin is displaced from the nuclear periphery and coalesces into nucleoplasmic foci in QKO mESCs (Fig. 1D, 1H), but not in lamin TKO (Fig. 1B, 1H) or LBR KO mESCs (Fig. 1C, 1H). Regions of more compacted chromatin can be visualized as regions of high relative intensity of DNA stain within the nucleus; while brightly stained, compacted chromatin is detectable at the nuclear periphery in WT, LBR KO, and TKO mESCs, compacted chromatin shifts away from the nuclear periphery and into the nucleoplasm in QKO mESCs (Fig. S2D,E). Further, while an electron-dense layer of heterochromatin is readily visible underneath the nuclear envelope in WT (Fig. 1I, 1M), lamin TKO (Fig. 1J, 1M), and LBR KO (Fig. 1K, 1M) mESCs, heterochromatin is undetectable underneath the NE in QKO mESCs (Fig. 1L-M) and is instead more prominent in the nucleoplasm (Fig. S2I).

To understand the timescale of H3K9me2-marked chromatin displacement from the nuclear periphery in the absence of the lamins and LBR, we used a tetracycline-inducible RNAi system⁸⁰ to induce the depletion of LBR to undetectable levels within 48 hours in TKO mESCs (Fig. S3F). Disorganization of H3K9me2-marked chromatin also became apparent within 48 hours (Fig. S3G-J). Re-establishment of H3K9me2 positioning could be rescued within 48 hours by expressing exogenous Halo-tagged LBR in QKO mESCs (Fig. 1G,H), but not by expressing the nucleoplasmic domain or transmembrane domain of LBR alone (Fig. S3C-E), which indicates that displacement of H3K9me2-marked chromatin from the nuclear periphery of lamin-depleted cells depends on LBR and is reversible.

The Genomic Distribution of H3K9me2 is Preserved in the Absence of the Lamins and LBR

We noted that ablating the lamins and LBR appears to affect the spatial distribution, but not the total abundance, of H3K9me2 (Fig. 1E). This observation suggests that deposition of H3K9me2 onto genomic loci occurs independently of its enrichment at the nuclear periphery.

²⁸Since QKO mESCs have internalized their H3K9me2-marked chromatin, we asked whether this change in chromatin positioning affects the genomic position and abundance of H3K9me2. We used a monoclonal antibody with validated selectivity for this mark in genome-binding assays^{57,58} to perform CUT & RUN (cleavage under targets and release using nuclease) with spike-in control⁸¹. We then applied a four-state hidden Markov model (HMM)⁸², which identified domains lacking H3K9me2, domains with intermediate (class 1) H3K9me2 density, and domains with high (class 2) H3K9me2 density, as well as excluded blacklisted regions (Fig. 2A; Fig. S4; Table S1; see Methods). Altogether, we identified H3K9me2 domain-resident genes in WT mESCs that are closely concordant with previously published analyses of H3K9me2 (74% overlap; Fig. S4F-H) and LAD-resident genes (determined by LB1 ChIP-seq; 70% overlap; Fig. S4I-K) in mESCs in 2i + LIF culture conditions⁵⁷. H3K9me2 domains appear similar across the genomes of WT, lamin TKO, LBR KO, and QKO mESCs (Fig. 2A), with similar numbers of class 1 and class 2 domains (Fig. 2B) that cover approximately 60% of the genome in kilobase- to megabase-long tracts (Figure 2C; Fig. S4B-C; ~59%, ~65%, ~61%, and ~57% of the genome covered in WT, LBR KO, TKO, and QKO mESCs, respectively). Approximately 66% of H3K9me2 domains are shared across all four genotypes (Fig. 2D), and over 70% are present in both WT and QKO mESCs (Fig. S4L). We noted modestly higher density of H3K9me2 within both class 1 and class 2 domains in QKO mESCs compared to other genotypes (Fig. 2E-F). Taken together, these data indicate that ablating the lamins and LBR disrupts the spatial positioning of H3K9me2 within the nucleus (Figure 1) but does not affect its deposition on the genome (Figure 2).

Spatial Displacement Dysregulates H3K9me2-marked Genes

Association of genes with the nuclear periphery is correlated with repression of transcription^{51,52,54,83,84}. Consistently, we find a strong correlation between H3K9me2 modification, LAD residence, and low transcription (Fig. S4F-K, Fig. 2G); genes found within H3K9me2-marked domains are more likely to be repressed than genes found outside these regions, and the strength of repression correlates with the density of H3K9me2 (Fig. 2G). Transcriptional activation often correlates with displacement of genes from the nuclear periphery^{55,57,85,86}, which suggests that positioning of genes at the nuclear periphery promotes repression. If this prediction is correct, heterochromatin displacement should weaken repression. Global transcriptional profiling by total RNAseq indicates that LBR ablation and lamin ablation each deregulate modest numbers of genes; in contrast, removal of both the lamins and LBR has a major synergistic effect on gene expression, with a bias toward upregulation (Fig. 3A; Table S2). We focused on changes in gene expression between lamin TKO mESCs (where heterochromatin positioning is intact) versus lamin + LBR QKO mESCs (where heterochromatin positioning is disrupted) (Fig. 3B); here, nearly twice as many genes are upregulated as are downregulated (983 genes > 2-fold up, 501 genes > 2-fold down). This outcome indicates that recruitment of heterochromatin to the nuclear periphery bolsters repression.

Genes involved in development, differentiation, signaling, and stress responses are dysregulated in QKO mESCs (Fig. 3C, Table S3), although expression of core pluripotency genes is maintained in all genotypes (Fig. S11). H3K9me2 is enriched on dysregulated genes compared to unchanged genes (Fig. 3D), indicating that the transcriptional regulation of H3K9me2-marked genes is altered when heterochromatin is displaced. Further, inspection of derepressed loci in QKO mESCs reveals transcription within intact class 1 H3K9me2 domains (e.g. the class 1 resident upregulated gene *Slamf6*, Fig. 3E) and class 2 H3K9me2 domains (e.g. the class 2 resident upregulated gene *Mfap3l*, Fig. 3F). This de-repression occurs even

though H3K9me2 domains are generally preserved in QKO mESCs (Fig. 2F) and are in fact accumulating even higher levels of H3K9me2 than in WT mESCs (Fig. 2D-E). These data indicate that some H3K9me2-marked genes are less effectively repressed when they are displaced from the nuclear periphery. In addition, some H3K9me2-marked genes are further repressed (Fig. 3D) while some non-H3K9me2-modified genes are also dysregulated (Fig. S5A), perhaps as secondary effects of heterochromatin disorganization.

To explore the initial consequences of heterochromatin displacement on gene expression, we analyzed the transcriptomes of lamin TKO mESCs after acute RNAi-mediated depletion of LBR for 2 or 4 days. These data revealed very few deregulated genes at day 2 (Fig. 3G; Fig. S5B; Table S4), when H3K9me2 disorganization is already apparent (Fig. S3); however, after 4 days of LBR depletion, 102 genes were upregulated more than 2-fold, while only 21 genes were downregulated more than 2-fold (one of which was *Lbr*) (Fig. 3G,H; Table S4), indicating a strong bias toward de-repression. These upregulated genes are significantly enriched for H3K9me2 compared to unaffected or downregulated genes (Fig. 3I). Altogether, we conclude that removal of the lamins and LBR causes the spatial displacement of H3K9me2-marked genes, followed by their de-repression.

Heterochromatin Displacement Causes Widespread De-repression of Transposons

Deposition of H3K9me2 by G9a/GLP in mESCs^{19,20} promotes the effective repression of retrotransposons, including long interspersed elements (LINE1s) and endogenous retroviruses flanked by long terminal repeats (ERV LTRs)⁶⁴⁻⁶⁸. The role of heterochromatin positioning in repression of repeat elements is less clear, although LINE1s, ERV LTRs, and other transposable elements (TEs) reside within LADs^{76,87}. As our data indicated that H3K9me2 is less able to repress a variety of genes when displaced from the nuclear periphery, we explored whether repression of TEs is also impaired. We applied Tetrascripts⁸⁸ to detect and analyze the differential expression of multi-mapping RNAseq reads originating from ~1200 distinct TE families that are integrated at numerous sites across the genome. LBR ablation had a minor

effect on TE expression, with 7 TE families (0.5% of all) de-repressed at least 2-fold in LBR KO mESCs (Fig. 4A-B), while lamin ablation moderately induced TE expression, with 27 TE families (2% of all) de-repressed at least 2-fold in TKO mESCs (Fig. 4A,4C, Table S5). TEs that are de-repressed by lamin disruption alone include the ERV1 LTRs MMERGLN and MMERGLN-int and the L1MdA_I and L1MdA_II families of LINE1s (Fig. 4C). Co-depletion of the lamins and LBR dramatically elevated TE expression, with 338 TE families (27% overall) upregulated at least 2-fold in QKO mESCs compared to WT mESCs (Fig. 4A,4D, Table S5). TE classes including SINEs, LINEs, and satellites were affected in QKO mESCs, with LTR-containing retrotransposons the most widely de-repressed (38% of LTRs de-repressed; Fig. 4A). Within the LTR class, ERV-Ks including ERVB4_2-I and RLTR45-int are potently upregulated in QKO mESCs compared to both WT and TKO mESCs (Fig. 4C-D). Notably, ERV-K family members are similarly de-repressed when H3K9me2 is depleted via G9a/GLP inactivation in mESCs^{67,68}. Depletion of the lamins and LBR appears to have a synergistic effect on LINE1 expression, as L1M3a, L1MdA_I, and L1MdA_II are further upregulated in QKO mESCs compared to TKO mESCs (Fig. 4C-D).

Each TE family is present in numerous identical copies across the genome, but the expression of individual copies can be evaluated by searching for uniquely mapped transcripts that contain flanking genomic sequence. We used this approach to evaluate the expression of the large L1MdA_I LINE1 family⁸⁹, which is present in 3586 copies in the mouse genome. While L1MdA_I copies remain lowly transcribed in WT and LBR KO mESCs (Fig. 4E), 550 individual L1MdA_I copies are upregulated at least 10-fold in TKO mESCs (Fig. 4F), while 684 copies are upregulated at least 10-fold in QKO mESCs (Fig. 4G). These data indicate that a significant proportion of the L1MdA_I LINE1 family is derepressed by depleting the lamins and LBR in mESCs.

To determine how quickly TEs become de-repressed when heterochromatin is displaced, we analyzed TE expression after acute RNAi-mediated depletion of LBR in lamin TKO mESCs

for 2 or 4 days. This comparison is useful in spite of the fact that some TEs are de-repressed in lamin TKO mESCs, as an additional 52 TE families are derepressed in lamin + LBR QKO mESCs compared to lamin TKOs (Fig. 4A). Strikingly, 42 uniquely mapped TE copies were potentially derepressed greater than 5-fold within 4 days of LBR depletion in TKO mESCs (Fig. S5C-D), indicating that TE de-repression follows H3K9me2 displacement.

The effects of heterochromatin displacement on TE expression are reminiscent of the effects of deleting H3K9 methyltransferases, which reduces H3K9me2/3 on TEs and allows their transcription^{66–68,90,91}. However, our analyses indicate that H3K9me2 is generally maintained on the same genomic loci when displaced from the nuclear periphery (Fig. 2). To evaluate H3K9me2 on TEs in the absence *versus* presence of the lamins and LBR, we analyzed uniquely mapped H3K9me2 CUT & RUN reads that included L1MdA_I LINE1 sequences. This analysis indicated that (i) L1MdA_I copies that are sensitive to the loss of the lamins and LBR are significantly more highly modified by H3K9me2 than unaffected L1MdA_I copies (Fig. 4H, 4I); and (ii) that these same L1MdA_I copies remain densely decorated by H3K9me2 in TKO and QKO mESCs and in fact gain even more H3K9me2 in mutant mESCs compared to WT mESCs (Fig. 4H, 4I). Therefore, similarly to our analyses of genes (Fig. 3), heterochromatin displacement allows the transcription of TEs in spite of their persistent H3K9me2 modification.

Heterochromatin Positioning Enables the Transition from Naïve to Primed Pluripotency

Our data indicate that H3K9me2 loses the capacity to repress the transcription of protein-coding genes (Fig. 3) and of TEs (Fig. 4) when displaced from the nuclear periphery. These observations lead us to hypothesize that the recruitment of H3K9me2-marked chromatin to the nuclear periphery strengthens H3K9me2-mediated repression. To further test the influence of heterochromatin positioning on the function of H3K9me2, we asked whether it is required for the transition from naïve to primed pluripotency, a developmental transition that can only be completed if G9a and GLP are upregulated to expand H3K9me2 across the genome^{67,92}. *In vivo*, this transition occurs when the inner cell mass of an embryo exits naïve

pluripotency and enters the epiblast state. While naïve pluripotency is approximated in culture by mESC growth in 2i + LIF conditions, induction of epiblast-like cells (EpiLCs) can be achieved by treatment of mESCs with FGF and Activin A growth factors for 24-48 hours^{93,94} (Fig. 5A).^{24,48} LBR KO and lamin TKO mESCs each exhibited a moderate defect in growth and/or survival during the transition to EpiLCs, lamin + LBR QKO mESCs were severely impaired in their ability to differentiate (Fig. 5B,5C), and only ~20% completed this transition. Further, EpiLC loss is an immediate consequence of lamin + LBR co-depletion, as acute depletion of LBR by RNAi in lamin TKOs impaired EpiLC differentiation (Fig. 5D).

In addition to their shared role in heterochromatin positioning, LBR and the lamins perform other important functions that could potentially be required to sustain EpiLC survival. We tested the relevance of these other functions to EpiLC survival as follows. Because LBR participates in cholesterol biosynthesis⁹⁵, we evaluated cholesterol levels in WT and mutant mESCs and EpiLCs. Cholesterol levels are unaffected by LBR ablation (Fig. S6A), likely because of the redundant activity of the TM7SF2 enzyme⁹⁵. The effect of deleting LBR on EpiLC survival is thus not a consequence of cholesterol depletion. mESCs flatten, migrate, and proliferate as they transform into EpiLCs (Fig. 5B). Because the lamins and heterochromatin each absorb forces on the nucleus⁹⁶, it is possible that mutant nuclei might not be able to endure the forces that arise from cellular flattening during differentiation. To test whether cellular flattening impairs survival of lamin + LBR QKO mESCs, we compared the viability of mESCs growing on a low-attachment substrate (gelatin), where cells form rounded colonies, to a higher-attachment substrate (Cultrex), where cells form more flattened and adherent colonies (Fig. S6B-C). We found no difference in cell viability between these conditions, indicating that cellular flattening itself does not impair survival of QKO mESCs.

We re-evaluated the spatial positioning of heterochromatin within EpiLC nuclei and found that similarly to QKO mESCs (Fig. 1), heterochromatin displacement from the nuclear periphery of QKO EpiLCs is apparent by H3K9me2 immunostaining (Fig. 5E-I), by Hoechst

staining of DNA compaction (Fig. S7A-D, E), and by TEM (Fig. 5K-L; Fig. S7F-J). Altogether, these data confirm that the lamins and LBR are also required for peripheral heterochromatin positioning in EpiLCs and demonstrate that H3K9me2 positioning is required for EpiLC viability.

Heterochromatin Positioning Influences Remodeling of H3K9me2 in Primed Pluripotency

While our microscopy analyses indicate that H3K9me2 is displaced from the nuclear periphery in QKO EpiLCs (Fig. 5H,I), we noted that H3K9me2 abundance appears to increase during the transition from naïve to primed pluripotency in all genotypes (Fig. 5E-H'; Fig. 5J). To quantify H3K9me2 abundance across the genome in EpiLCs, we again applied spike-in-controlled H3K9me2 CUT & RUN and identified domains of absent, intermediate (class 1), or high (class 2) H3K9me2 intensity with a 4-state HMM (Fig. 6). This spike-in-controlled analysis demonstrated expansion of H3K9me2 across the genome in WT EpiLCs *versus* mESCs that was apparent by visual inspection (Fig. 6A), by quantifying total genome coverage (Fig. S9C vs Fig. S4B; ~66% of genome within H3K9me2 domains in EpiLCs vs. ~59% in ESCs), by quantifying the median contiguous length of H3K9me2 domains in WT ESCs vs. EpiLCs (Fig. 6B; 130 kb in WT ESCs vs 190 kb in WT EpiLCs), and by tracking the net flow of genes into H3K9me2 domains in WT EpiLCs *versus* ESCs (Fig. 6C; 18729 genes move into H3K9me2 domains in EpiLCs; Table S6). Interestingly, the establishment of EpiLC-specific H3K9me2 domains is not accompanied by widespread repression of these newly modified genes; instead, most EpiLC H3K9me2 genes are unchanged in expression, while small numbers of genes are upregulated or downregulated (Fig. 6D). While a lower proportion of genes within constitutive H3K9me2 domains (those shared between mESCs and EpiLCs) are transcribed, a high proportion of genes within EpiLC H3K9me2 domains are transcribed (Fig. 6E). These observations suggest that H3K9me2 is overall less repressive and performs a distinct function in EpiLCs compared to mESCs. Altogether, these data indicate that H3K9me2 rapidly expands during the transition into primed pluripotency without immediately inducing widespread repression of newly modified loci.

We next applied spike-in-controlled CUT & RUN to mutant EpiLCs. Similarly to WT EpiLCs, expansion of H3K9me2 across the genome was readily apparent in LBR KO, lamin TKO, and lamin + LBR QKO EpiLCs (Fig. 6F). Our domain calling approach indicated that in WT, LBR KO and lamin TKO EpiLCs, H3K9me2 domains increase in median length and incorporate new genes (Fig. 6B-C; Fig. S9G-I) that remain transcriptionally active (Fig. 6E). However, domain calling identified short and fragmented H3K9me2 domains in QKO EpiLCs, even across genomic regions with high overall H3K9me2 signal (Fig. S9C,E,F). To avoid the confounding effects of variable HMM performance across samples, we compared H3K9me2 density within H3K9me2 domains identified in WT EpiLCs. Within these domain borders, QKO EpiLCs accumulate H3K9me2 to significantly higher levels than do other genotypes (Fig. 6G,H). In addition, H3K9me2 signal variance is significantly greater both genome-wide and within WT H3K9me2 domain borders in QKO EpiLCs compared to other genotypes (Fig. S9B; Fig. 6I,J). We surmise that the abnormally variable pattern of H3K9me2 deposition across the genome in QKO EpiLCs interferes with HMM domain calling. Taken together, these analyses indicate that heterochromatin displacement alters both the level and the pattern of H3K9me2 deposition along the genome during the transition from naïve to primed pluripotency.

Heterochromatin Positioning Silences Transposons and Alternative Cell Fate Genes in EpiLCs

We next evaluated the consequences of H3K9me2 displacement on the dynamic transcriptional landscape of EpiLCs. QKO EpiLCs exhibit widespread de-repression of TEs, with 298 TEs (24% overall) upregulated at least 2-fold compared to WT EpiLCs, and 224 TEs (18% overall) upregulated at least 2-fold compared to TKO EpiLCs (Fig. S10A, Table S7). In contrast, LBR KO and lamin TKO EpiLCs maintain repression of most TEs (Fig. 7A; Fig. S10A; Table S7). LINEs, satellites, and ERV LTRs are broadly de-repressed in QKO EpiLCs (Fig. 7A; Fig. S10D). To further explore the extent of TE de-repression, we analyzed unique transcripts originating from the L1MdA_I LINE1 family; while this family remains repressed in LBR KO EpiLCs (Fig. S10E), 96 copies were upregulated at least 10-fold in lamin TKO EpiLCs (Fig. S10F), while 229

copies were upregulated at least 10-fold in QKO EpiLCs compared to WT EpiLCs (Fig. S10G). Overall, L1MdA_I expression was more moderate in EpiLCs compared to mESCs (Fig. 4), suggesting that additional TE repressive mechanisms may be induced in primed pluripotency, or that only EpiLCs expressing moderate levels of TEs survive. Nevertheless, derepressed L1MdA_I copies are highly H3K9me2-modified in both wild type and mutant EpiLCs, while unaffected L1MdA_I copies are not (Fig. S10H-I), indicating that some TEs reside in constitutive H3K9me2 domains in both mESCs and EpiLCs, and that spatial displacement of H3K9me2 allows the selective de-repression of these TEs.

LBR KO and lamin TKO EpiLCs each exhibit modest changes to gene expression, while co-depletion of the lamins and LBR has a synergistic effect on gene expression (Fig. 7B; Table S8), similarly to our observations in naïve mESCs (Fig. 3). Lamin + LBR QKO EpiLCs exhibit a bias toward de-repression of genes compared to lamin TKO EpiLCs (Fig. 7B, 7C), with 2573 genes upregulated at least 2-fold and 1243 genes downregulated at least 2-fold. These dysregulated genes are enriched for the H3K9me2 modification compared to unaffected genes, indicating that disrupting heterochromatin recruitment affects the regulation of H3K9me2-modified genes (Fig. 7D). Inspection of transcription within H3K9me2 domains revealed examples of genes that are de-repressed in QKO EpiLCs yet reside within H3K9me2 domains, such as the transcription factor *Gata6* (Fig. 7E) and the morphogen *Wnt5a* (Fig. 7F). Genes dysregulated in QKO EpiLCs include components of immune response, host defense, stress, and apoptosis pathways (Fig. 7G; Table S9). Notably, genes involved in the innate immune response to viral RNA are upregulated, including *Ifit1* and *Rigi*; transcription of these genes is induced by TE activity^{97,98} and can drive apoptosis⁹⁹. Dysregulated genes also participate in a range of cell fate determination, morphogenesis, and differentiation networks, suggesting that developmental progression is abnormal (Fig. 7G; Table S9). We investigated the regulation of cell fate in mutant EpiLCs more closely (Fig. 7H), which indicated that QKO EpiLCs succeed in silencing naïve pluripotency genes and activating primed/epiblast stage pluripotency

genes. Therefore, QKO mESCs can undergo a cell state change in response to a pro-differentiation stimulus. However, we noted that in addition to appropriately inducing epiblast-stage genes, QKO EpiLCs abnormally express various alternative cell fate genes (Fig. 7H). These include markers of the primitive endoderm, such as *Fgfr2*, *Gata6*, and *Pdgfra*; this extra-embryonic lineage should be mutually exclusive with the epiblast fate^{100,101} (Fig. 7H). QKO EpiLCs also abnormally express a range of other lineage-specific morphogens and transcription factors, such as *Wnt5a*, *Wnt6*, *Wnt8a*, *Tgfb1*, and *Eomes* (Fig. 7H). This outcome suggests that while recruitment of heterochromatin to the nuclear periphery is not required for the transition from naïve to primed pluripotency *per se*, it enables the effective specification of a lineage-specific gene expression program. Altogether, we conclude that the lamins and LBR control both the spatial positioning and the repressive capacity of H3K9me2 to shape cell fate decisions during early mammalian development.

Discussion

The Lamins and LBR Exert Broad Influence on Heterochromatin Organization and Function

The parallel roles of lamin A/C and LBR in heterochromatin organization were first described over 10 years ago⁷³. Our data indicate that the lamins and LBR together exert broad control on heterochromatin organization and function in pluripotent cells. Strikingly, we observe that the dense layer of compacted, electron-dense heterochromatin that is a hallmark of most eukaryotic cells disperses when the lamins and LBR are ablated (Fig. 1L). H3K9me2-marked loci are also displaced from the nuclear periphery and into nucleoplasmic foci in cells lacking these proteins (Fig. 1D, 1F). This phenotype bears some similarity to the gradual intranuclear coalescence of heterochromatin that occurs in several types of neurons that downregulate lamin A/C and LBR as they differentiate^{71,73,102}. In this context, chromatin inversion takes place over several weeks after cell cycle exit⁷³ without any disruption to heterochromatin-mediated repression^{71,102}, in contrast to our observations. We surmise that the high proliferation rate of mESCs prevents the complete coalescence of heterochromatin into a single intranuclear focus

within one cell cycle. Alternatively, additional chromatin changes such as relabeling of H3K9me2 loci with H3K9me3 and/or presence of distinct H3K9me2/3 binding proteins may promote heterochromatin coalescence in neurons⁷¹ but not in mESCs (Fig. 2). Nevertheless, our findings indicate that heterochromatin reorganization can be induced by the removal of the lamins and LBR in pluripotent cells. Further, our data establish for the first time that the unique enrichment of H3K9me2-marked chromatin underneath the nuclear periphery is maintained by the redundant function of the lamin and LBR proteins.

Our data indicate that the lamins can sustain chromatin organization in the absence of LBR and vice versa. While LBR is much more highly expressed than lamin A/C in pluripotent cells, low levels of lamin A/C have been recently shown to influence gene expression in naïve pluripotency¹⁰³. LBR alone can drive peripheral heterochromatin positioning when ectopically expressed in various cell types, while ectopically expressed Lamin A/C cannot⁷³; this implies that Lamin A/C's heterochromatin tethering function is mediated by additional factors with variable expression levels across tissues, while LBR can either directly tether heterochromatin, or alternatively work through ubiquitously expressed intermediary protein(s). Various lamin-bound proteins such as LAP2b, HDAC3, PRR14, and others are candidates that could promote lamin-mediated heterochromatin tethering^{52,57,104,105}, while LBR binds to the H3K9me2/3-binding protein HP1¹⁰⁶ and can also interact with histone tails via its Tudor domain^{107,108}. In the future, we will dissect how these interactions contribute to heterochromatin tethering in the sensitized background of lamin-null or LBR-null mESCs.

The Nuclear Periphery Influences the Repressive Capacity of H3K9me2

Our data indicate that disruption of the lamin and LBR heterochromatin tethering proteins weakens the repression of H3K9me2-modified loci even though their H3K9me2 modification is preserved (Fig. 3B,D). While H3K9me2 has a well-established capability to repress transcription^{62,63}, our data demonstrate that nuclear spatial position influences the function of H3K9me2 and is consistent with recent indications that the repressive capacity of

H3K9me2 is context-dependent. For instance, chromatin bearing H3K9me2 alone is relatively more permissive to transcription than H3K9me2-modified and lamina-associated regions of the genome⁷⁰. The function of H3K9me2 also appears to change during the differentiation of photoreceptor neurons, where pre-existing repressive H3K9me2 is gradually converted to H3K9me3 to preserve repression, while euchromatic regions of the genome acquire H3K9me2 but remain transcribed⁷¹. Notably, this shift in H3K9me2's function is accompanied by the downregulation of the lamin A/C and LBR heterochromatin tethers⁷³; similarly, we demonstrate that removal of the lamins and LBR decreases the repressive capacity of H3K9me2. By using an inducible RNAi system to acutely remove LBR in lamin-null mESCs, we determined that detachment of H3K9me2 is followed by de-repression of H3K9me2-marked genes within days (Fig. 3G-I). Based on these observations, we propose that recruitment to the nuclear periphery favors repression of H3K9me2-marked loci, while displacement from the nuclear periphery enables expression of H3K9me2-marked loci.

Heterochromatin tethering could enhance repression by several potential mechanisms. Repression may be induced by steric occlusion if binding of H3K9me2 and oligomerization of tethering proteins together promote compaction of chromatin domains. Similarly, tethering to the nuclear periphery may limit turnover of nucleosomes to enable long-term memory of chromatin state, as has been demonstrated in *S. pombe*⁵⁰. Finally, repression at the periphery may be achieved by the addition or removal of other chromatin marks to consolidate repression. For instance, tethering of a locus to the nuclear periphery is often accompanied by histone deacetylation^{52,83}.

The Nuclear Periphery Maintains Repression of Transposons

TEs are enriched in LADs in both pluripotent and differentiated cells^{76,87}, and our data indicate that lamin disruption allows the expression of some TE families, particularly in naive pluripotency (Fig. 4A, C). While altered gene expression was previously reported in lamin TKO mESCs, the expression of TEs in these cells was not evaluated⁷⁹. Intriguingly, alterations to the

lamina that occur in aged and senescent cells have been linked to displacement and/or activation of retrotransposons^{109–112}, suggesting that the lamina may also repression of TEs in differentiated cells.

H3K9me2 and H3K9me3 each play a major role in repression of TEs⁹¹, and we find that displacement of H3K9me2 from the nuclear periphery by ablation of both the lamins and LBR leads to pervasive activation of both retrotransposons and DNA transposons. By analyzing individual genomic copies of the large L1MdA_I LINE1 family, we determined that H3K9me2-marked TEs are sensitive to activation upon H3K9me2 displacement, while TEs that lack H3K9me2 are not affected (Fig. 4H-I). Strikingly, the effect of H3K9me2 displacement on TE expression is comparable to the effect of preventing the deposition of H3K9me2. For instance, ablating the H3K9me2/3-depositing enzyme SETDB1 activates a subset of ERV LTRs⁹⁰ while ablating the H3K9me2 enzyme G9a/GLP or ablating all H3K9me2 enzymes together (SETDB1, SETDB2, G9a, and GLP) de-represses many ERV LTRs as well as LINE1s^{64–68,91}. We find that acute depletion of LBR in lamin TKO mESCs induces TE expression within 2-4 days (Fig. S5C-D), indicating that TE activation is a rapid response to heterochromatin displacement. Therefore, we conclude that peripheral positioning is required for the effective repression of H3K9me2-modified TEs in pluripotent cells.

TE activation can have wide-ranging effects on genome function and stability (reviewed in¹¹³). TEs can act as alternative enhancers, promoters, or exons to create novel lncRNAs or protein-coding genes^{65,90,114}. Younger TE families that retain the ability to undergo transposition will be unleashed to do so if they become transcriptionally active and will perturb the loci they insert into. Several young and mobile TE families are derepressed when heterochromatin is displaced in QKO cells. These include the L1MdA_I LINE1 family, which is the youngest LINE1 family in the mouse genome⁸⁹; and ERV LTRs, many of which undergo transposition in the mouse genome¹¹⁵. The mobilization of autonomous TEs (such as LINE1s) can in turn induce the activity and/or transposition of non-autonomous TEs such as SINEs¹¹³. Altogether, this cascade

of effects initiated by TE activation may explain why we observe changes in both gene and TE expression that include but are not limited to H3K9me2-modified loci.

Mechanisms of TE repression change as cells exit naïve pluripotency and differentiate. Naïve pluripotent cells have low levels of DNA methylation and instead rely more heavily on H3K9me2/3 for the establishment and/or maintenance of TE silencing⁶⁴. DNA methyltransferases are upregulated as cells exit from naïve pluripotency and contribute to repression of TEs. We noticed that lamin TKO mESCs exhibit moderate activation of TEs, but this activation subsides as TKO cells enter primed pluripotency, which suggests that alternative mechanisms for establishing and/or maintaining TE repression are still functional in lamin-null cells. In contrast, we noted pervasive expression of TEs in both QKO mESCs and EpiLCs. Pluripotent and differentiated cells also differ in their sensitivity to TE expression: differentiated cells express innate immune RNA-sensing proteins that can be activated by TE-derived RNA to induce apoptosis⁹⁷⁻⁹⁹ while pluripotent cells do not express these proteins¹¹⁶. We noted upregulation of RNA sensors such as *Rig-I* and *Ifit1* in QKO EpiLCs (Fig. 7G), leading us to speculate that TE expression may induce interferon-mediated apoptosis and prevent these cells from surviving the transition to primed pluripotency.

The Nuclear Periphery Regulates H3K9me2 During Differentiation

We have shown that H3K9me2 density increases during the transition from naïve to primed pluripotency. While some earlier reports questioned whether H3K9me2 expands across the genome during differentiation^{117,118}, we observed this phenomenon with both immunofluorescence and spike-in-controlled CUT & RUN (Fig. 5J; Fig. 6A-C). Further, we demonstrate that the nuclear periphery regulates the density of H3K9me2 deposition during EpiLC differentiation. When H3K9me2 is displaced from the nuclear periphery by the removal of the lamins and LBR, its density increases to even higher levels in QKO EpiLCs (Fig. 6F-H) but is more disorganized across the genome than in normal EpiLCs (Fig. 6I-J). The levels of the G9a/GLP methyltransferase are known to increase during EpiLC differentiation⁶⁷, but we do not

observe further transcriptional upregulation of G9a or GLP in QKO EpiLCs that could explain the abnormally high levels of H3K9me2 observed. We cannot rule out the possibility that the activity of the G9a/GLP enzyme is increased in the absence of the lamins and LBR. We conclude that heterochromatin tethering influences the deposition of H3K9me2 and/or its perdurance on modified loci in primed pluripotency.

Many loci that gain H3K9me2 in EpiLCs are actively transcribed (Fig. 6D-E), which suggests that H3K9me2 performs a distinct function during this developmental transition that is not obligately linked to repression. While the function of H3K9me2 at this stage is poorly understood, recent work indicates that in the epiblast, H3K9me2 expands into actively transcribed regions of the genome that retain chromatin marks associated with active transcription on enhancers and promoters, such as H3K27ac^{67,94}. This transitory co-occupation of *cis*-regulatory elements with H3K27ac and H3K9me2 has been proposed to prime these loci for future differentiation-linked silencing^{67,94}. The function of H3K9me2 is disrupted in QKO EpiLCs, as H3K9me2 is enriched on dysregulated genes (Fig. 7D). Further, genes associated with various cell fates are discordantly co-expressed (Fig. 7E-H). Therefore, we conclude that recruitment of heterochromatin to the nuclear periphery enables the repression of lineage-irrelevant genes and is required for the normal orchestration of development.

Figures

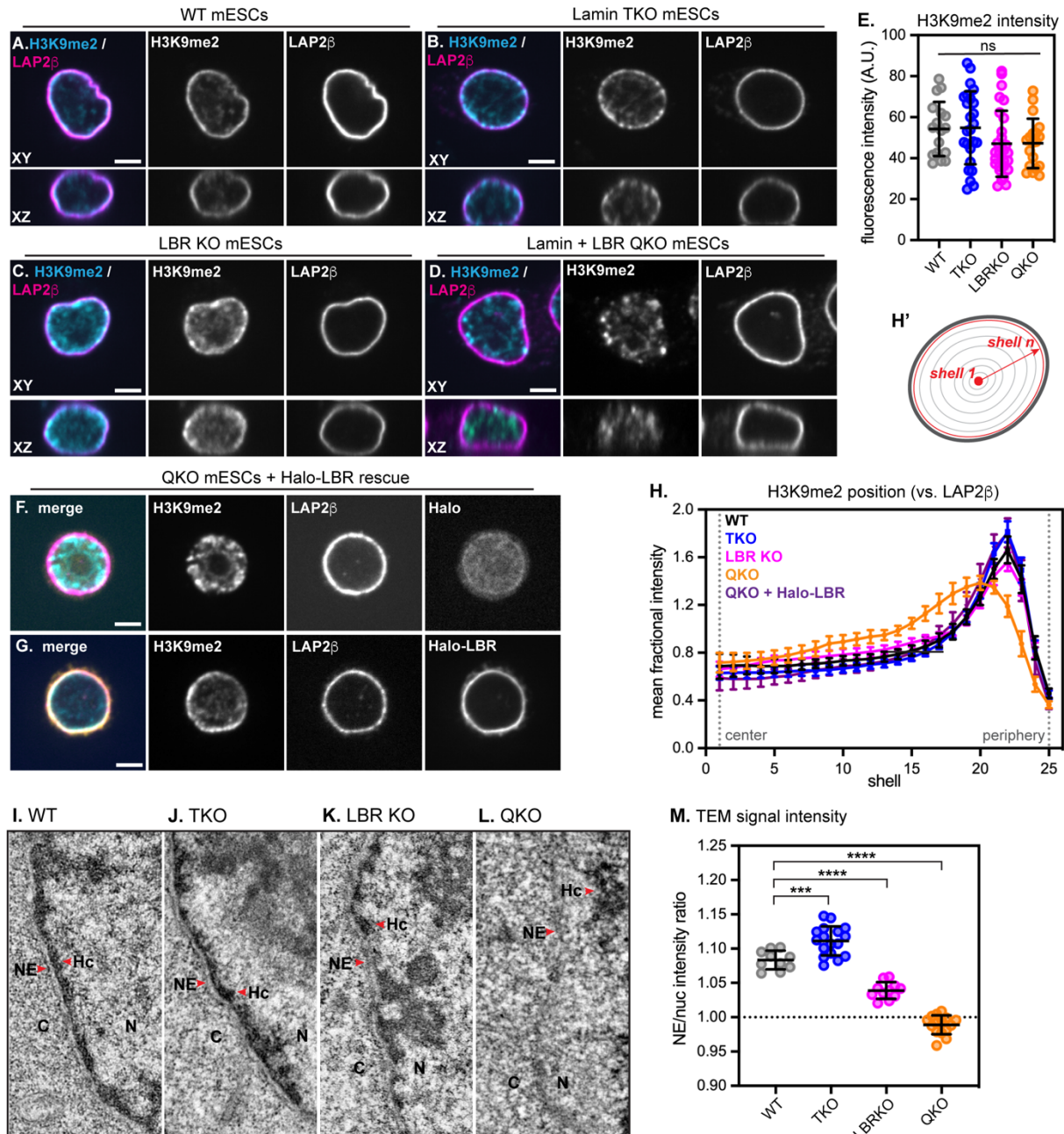


Figure 1 The lamins and LBR localize H3K9me2-marked chromatin to the nuclear periphery in mESCs.

Immunofluorescence of H3K9me2 localization compared to the INM protein LAP2b in WT (A), lamin TKO (B), LBR KO (C), and lamin + LBR QKO (D) mESCs. A central z-slice (XY) and a central Y-slice (XZ) are shown. Scale bar, 5 mm. (E) H3K9me2 total fluorescence intensity per nucleus in WT (n = 17), TKO (n = 25), LBR KO (n = 28), and QKO mESCs (n = 19), p > 0.05 by one-way ANOVA. Bars indicate mean and standard deviation. (F) Immunofluorescence of H3K9me2 localization compared to the INM protein (LAP2 β) in lamin + LBR QKO mESCs expressing Halo-NLS (F) or Halo-LBR (G) for 48 hours. (H, H') Radial intensity analysis of H3K9me2 position (continued on next page)

(continued from previous page) in WT, TKO, LBR KO, and QKO mESCs (n = 25 nuclei per condition) and in QKO mESCs expressing Halo-LBR (n = 16 nuclei). **** p < 0.0001, WT vs QKO, shells 9-19, 22-24; * p < 0.05, WT vs TKO, shells 21-22; * p < 0.05, WT vs LBR KO, shells 14, 15, 16. Unpaired t-test used for all comparisons. Points indicate mean and error bars indicate 95% confidence intervals. See Figure S3 for full Halo-LBR rescue analysis and statistics. (I-L) Transmission electron microscopy showing 1.3 mm by 2.6 mm section of the nuclear periphery in WT (I), lamin TKO (J), LBR KO (K), and lamin + LBR QKO (L). C, cytoplasm; N, nucleus; NE, nuclear envelope; Hc, heterochromatin. (M) Quantification of relative TEM signal intensity ratio at the NE versus nucleoplasm (nuc), for WT (n = 10), LBRKO (n = 11), TKO (n = 17) and QKO (n = 15) mESCs. **** indicates $p_{\text{adj}} < 0.0001$ for WT vs LBRKO and WT vs QKO; *** indicates $p_{\text{adj}} = 0.0002$ for WT vs TKO by one-way ANOVA followed by Dunnett's multiple comparisons test. Bars indicate mean and standard deviation.

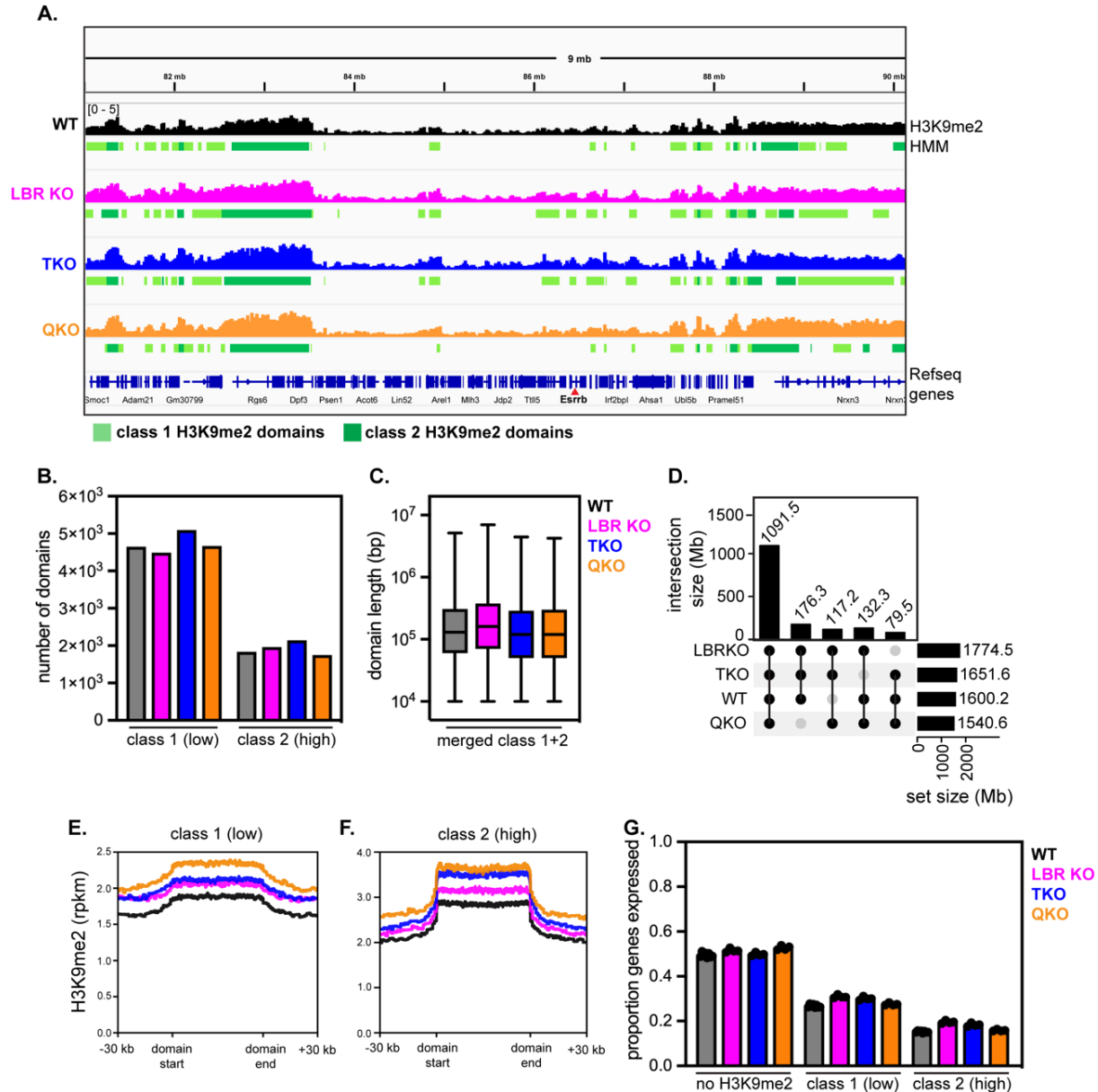


Figure 2 Genomic distribution of H3K9me2 is preserved after removal of the lamins and LBR.

(A) Representative genome tracks and domain calls for H3K9me2 in WT, LBR KO, TKO, and QKO ESCs on a 9 Mb section of chromosome 12, including the *Esrrb* gene. Y axis range indicated at top left is the same for all tracks shown. Low K9me2 density “class 1” domains are marked in light green and high K9me2 density “class 2” domains are marked in dark green. (B) Number of HMM class 1 (low K9me2 density) and class 2 (high K9me2 density) domains called across genotypes. (C) Size of contiguous HMM class 1 (low K9me2 density) and class 2 (high K9me2 density) domains called across genotypes. (D) UpSet plot showing intersections of H3K9me2 domains between genotypes; the majority of domains are shared across all 4 genotypes, and a minority of domains are uniquely found in other 3-member groups of genotypes. Averaged density of H3K9me2 in all class 1 (E) and all class 2 (F) domains across genotypes. (G) Proportion of genes expressed (minimum of 5 TPMs) outside of H3K9me2 domains, within H3K9me2 class 1 domains, or within H3K9me2 class 2 domains across genotypes.

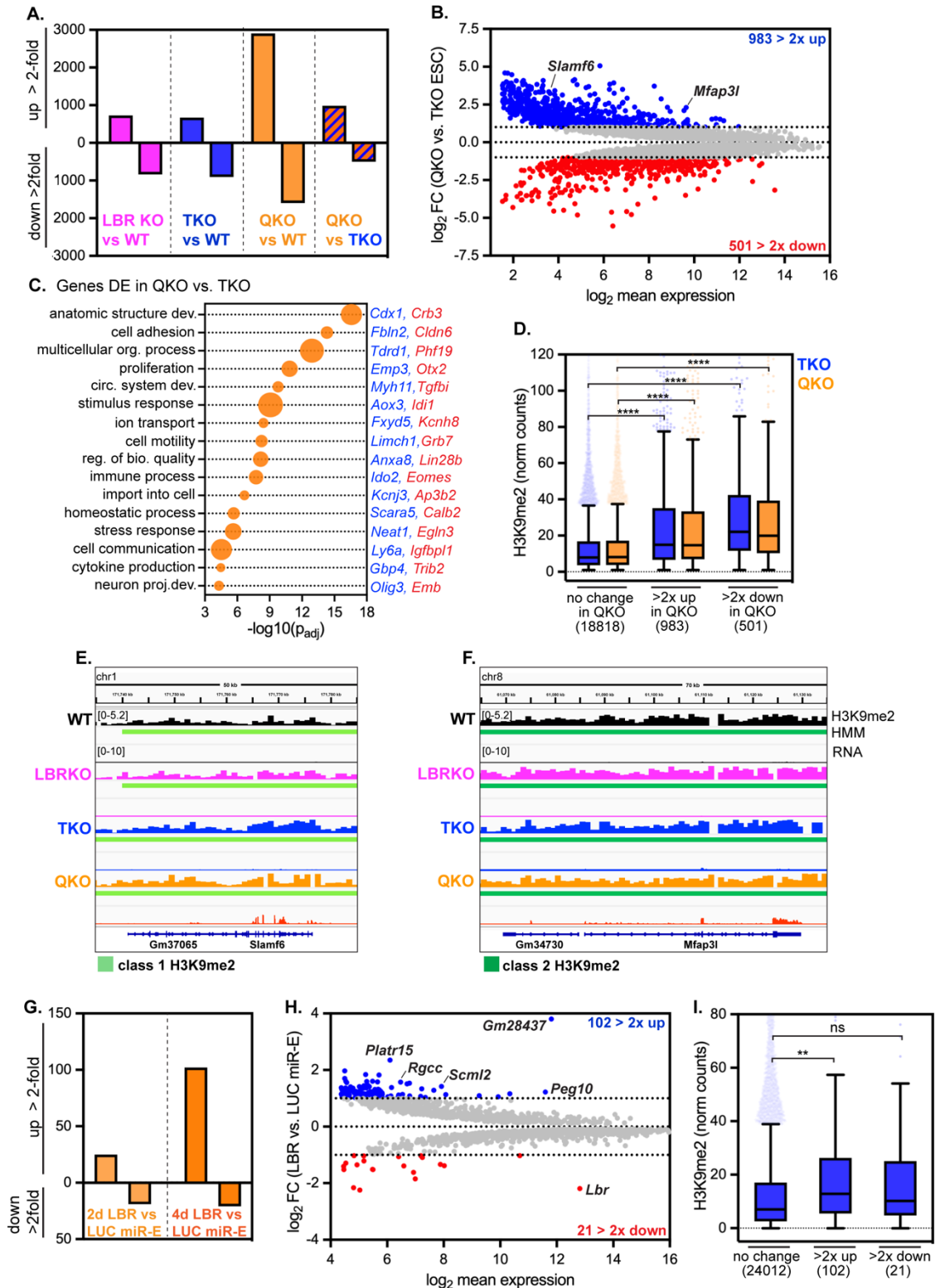


Figure 3 Removal of the lamins and LBR derepresses H3K9me2-marked and other genes.
(Figure caption continued on the next page.)

(Figure caption continued from the previous page.)

(A) Number of genes significantly differentially expressed at least 2-fold in all genotypes compared to wildtype mESCs, and in lamin + LBR QKO mESCs compared to lamin TKO mESCs. (B) MA plot comparing gene expression in QKO *versus* TKO mESCs. 5128 genes with a minimum p_{adj} of 0.05 shown; 983 genes are upregulated at least 2-fold, while 501 genes are downregulated at least 2-fold. (C) Gene ontology analysis of all genes significantly differentially expressed by at least 2-fold in QKO vs. TKO mESCs. Biological process GO terms identified with gProfiler and reduced by ReVIGO. Selection of list shown as bubble plot where size corresponds to number of DE genes associated with that term (ranging from 60 to 459 genes). Representative upregulated and downregulated genes that intersect with each GO term are highlighted in blue and red, respectively. See also Supplementary Table 1 for full list of GO terms. (D) H3K9me2 levels (normalized counts) on genes with unchanged expression ($p_{adj} > 0.05$, $n=18818$), genes upregulated at least 2-fold ($n = 983$) and genes downregulated at least 2-fold ($n = 501$) in QKO vs. TKO mESCs. **** indicates that comparisons indicated are significantly different ($p < 0.0001$) by Kruskal-Wallis multiple comparisons test with Dunn's correction. Box (Tukey) plot center line indicates median; box limits indicate 25th to 75th percentiles; whiskers indicate 1.5x interquartile range; points indicate outlier values. (E) H3K9me2 and RNA levels of class 1 domain-resident gene *Slamf6* (E) and class 2 domain-resident gene *Mfap3l* (F) across genotypes. Y axis range indicated at the top left of each panel is the same for all tracks shown within panel. (G) Number of genes significantly differentially expressed at least 2-fold in lamin TKO mESCs expressing LBR versus LUC miR-E for 2 or 4 days. (H) MA plot comparing gene expression in lamin TKO mESCs expressing LBR or LUC miR-E for 4 days. 2055 genes with a minimum p_{adj} of 0.05 shown; 102 genes are upregulated at least 2-fold, while 21 genes are downregulated at least 2-fold. (I) H3K9me2 levels (normalized counts) in TKO mESCs on genes with unchanged expression ($p_{adj} > 0.05$, $n=24012$), genes upregulated at least 2-fold ($n = 102$) and genes downregulated at least 2-fold ($n = 21$) in TKO mESCs expressing LBR miR-E for 4 days. ** indicates significant difference ($p = 0.0029$) by Kruskal-Wallis multiple comparisons test with Dunn's correction. Box (Tukey) plot center line indicates median; box limits indicate 25th to 75th percentiles; whiskers indicate 1.5x interquartile range; points indicate outlier values.

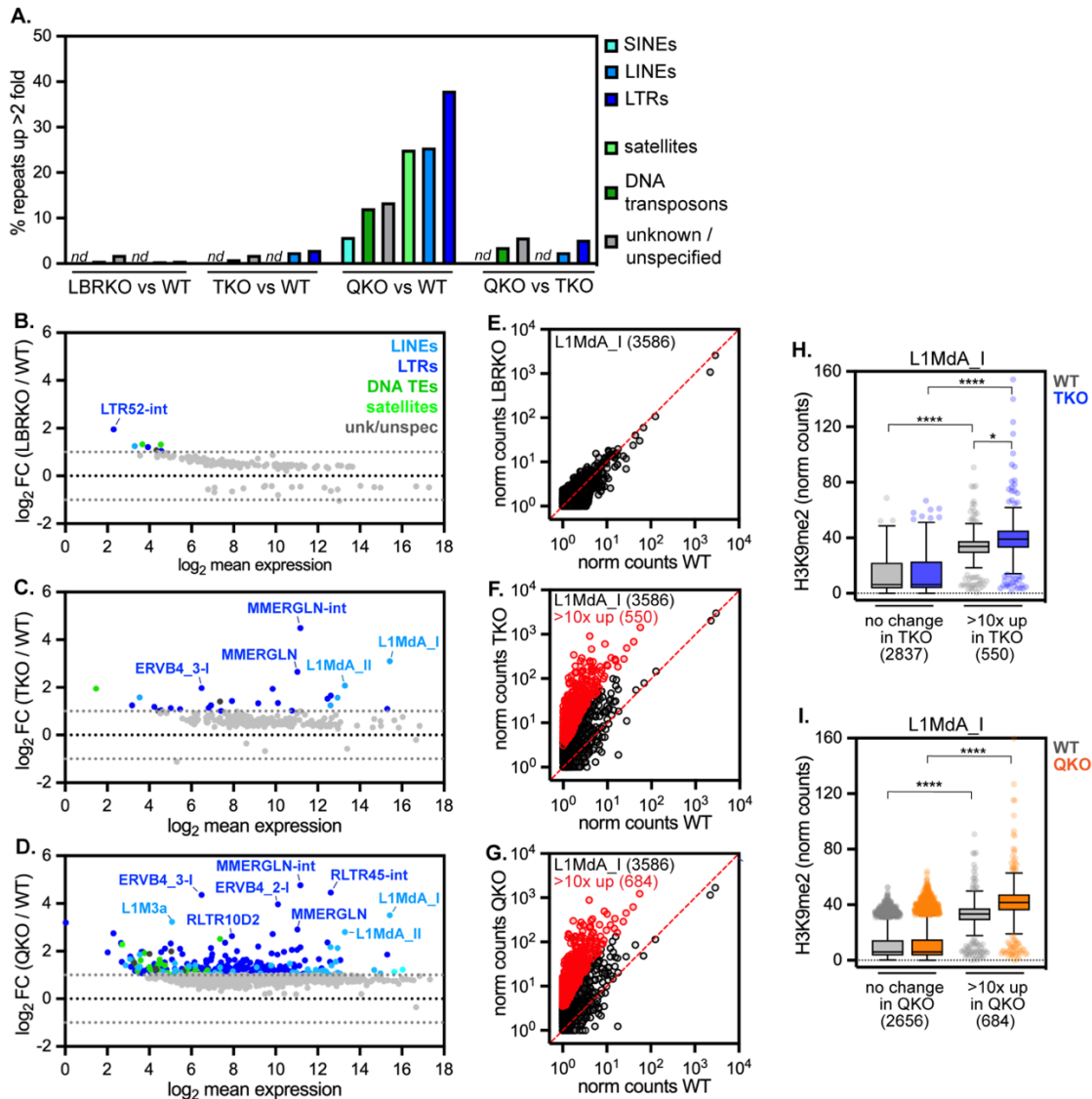


Figure 4 Ablation of the lamins and LBR allows pervasive transcription of transposons in spite of H3K9me2 modification.

(A) Percentage of transposable element families de-repressed at least 2-fold in all genotypes compared to WT mESCs, determined by Tetrascripts. *nd* indicates not detected. MA plots comparing expression of ~1200 TEs detected by Tetrascripts in (B) LBRKO versus WT mESCs, (C) TKO versus WT mESCs, and (D) QKO versus WT mESCs. All repeats without a significant change in between genotypes are gray; significantly differentially expressed TEs (minimum 2-fold change) are colored correspondingly to TE family. Normalized counts for 3586 uniquely mapped L1MdA_I LINE element genomic copies in (E) LBRKO versus WT mESCs, (F) TKO versus WT mESCs, and (G) QKO versus WT mESCs (plotted as $\log_{10}(\text{average} + 1)$). L1MdA_I copies with >10-fold change and significant difference in expression ($p_{adj} < 0.05$) in are colored in red. (H-I) Normalized counts from uniquely mapped reads of H3K9me2 on L1MdA_I LINE elements with unchanged expression versus those upregulated >10-fold in TKO mESCs (H) and in QKO mESCs (I). **** indicates $p < 0.0001$ and * indicates $p = 0.0105$ by one-way Kruskal-Wallis multiple comparisons test with Dunn's correction. Box (Tukey) plot center line indicates median; box limits indicate 25th to 75th percentiles; whiskers indicate 1.5x interquartile range; points indicate outlier values.

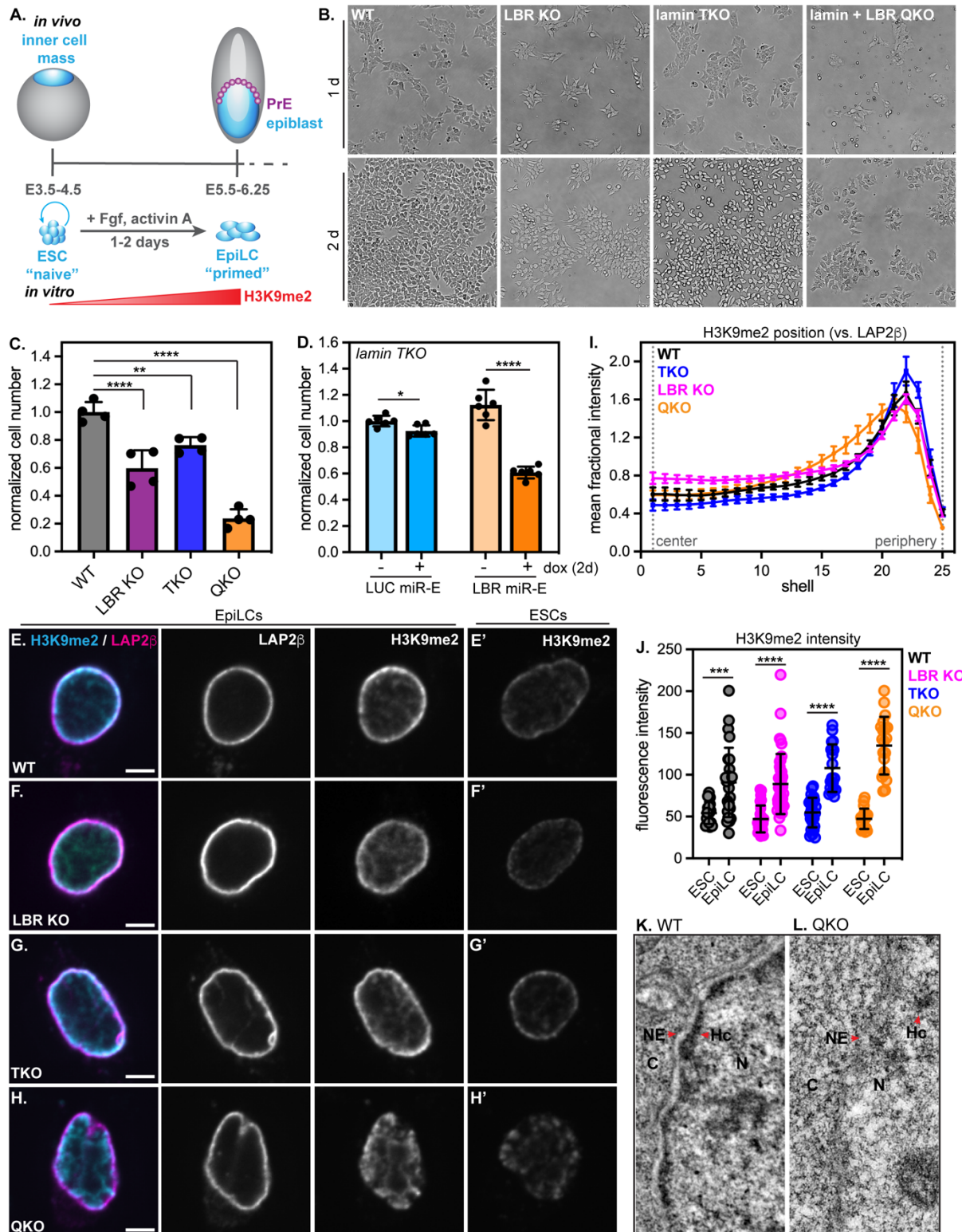


Figure 5 Heterochromatin positioning by the lamins and LBR is essential for EpiLC survival.

(Figure caption continued on the next page.)

(Figure caption continued from the previous page.)

(A) Diagram of naïve (ICM / mESC) to primed (epiblast / EpiLC) developmental transition *in vivo* and its approximation *in vitro*. (B) Representative brightfield microscopy images of WT, LBR KO, lamin TKO, and lamin + LBR QKO mESCs after 1 day (top panel) or 2 days (bottom panel) of culture in EpiLC differentiation conditions. (C) Normalized cell numbers after 2 days of culture in EpiLC differentiation conditions (normalized to WT; n = 4 replicates per genotype); columns indicate mean, error bars indicate standard deviation. **** indicates $p_{\text{adj}} < 0.0001$ for WT vs LBRKO and WT vs QKO; ** indicates $p_{\text{adj}} = 0.0058$ for WT vs TKO by one-way ANOVA followed by Dunnett's multiple comparisons test. (D) Normalized cell numbers of lamin TKO mESCs after 2 days of culture in EpiLC differentiation with (+) or without (-) co-induction of LUC or LBR miR-E. Columns indicate mean and error bars indicate standard deviation. n = 6 replicates from 2 independent clones shown. *, $p < 0.05$ and ****, $p < 0.0001$ by unpaired t-test. Immunofluorescence of H3K9me2 localization compared to the INM protein LAP2b in WT (E-E'), LBR KO (F-F'), lamin TKO (G-G'), and lamin + LBR QKO (H-H') cells. (E-H) show EpiLC samples while (E'-H') show mESC samples stained and imaged in parallel. Central z-slices (XY) shown. Scale bar, 5 μm . (I) Radial intensity analysis of H3K9me2 position *versus* LAP2b in WT, TKO, LBR KO, and QKO EpiLCs. **** $p < 0.0001$, WT vs QKO, shells 14-19, 24-25. (J) H3K9me2 total fluorescence intensity per nucleus in WT (n = 26), TKO (n = 18), LBR KO (n = 41), and QKO (n = 20) EpiLCs. *** $p < 0.001$, **** $p < 0.0001$, unpaired t-test. Transmission electron microscopy showing 1.3 μm by 2.6 μm section of the nuclear periphery in WT (K) and lamin + LBR QKO (L) EpiLCs. C, cytoplasm; N, nucleus; NE, nuclear envelope; Hc, heterochromatin.

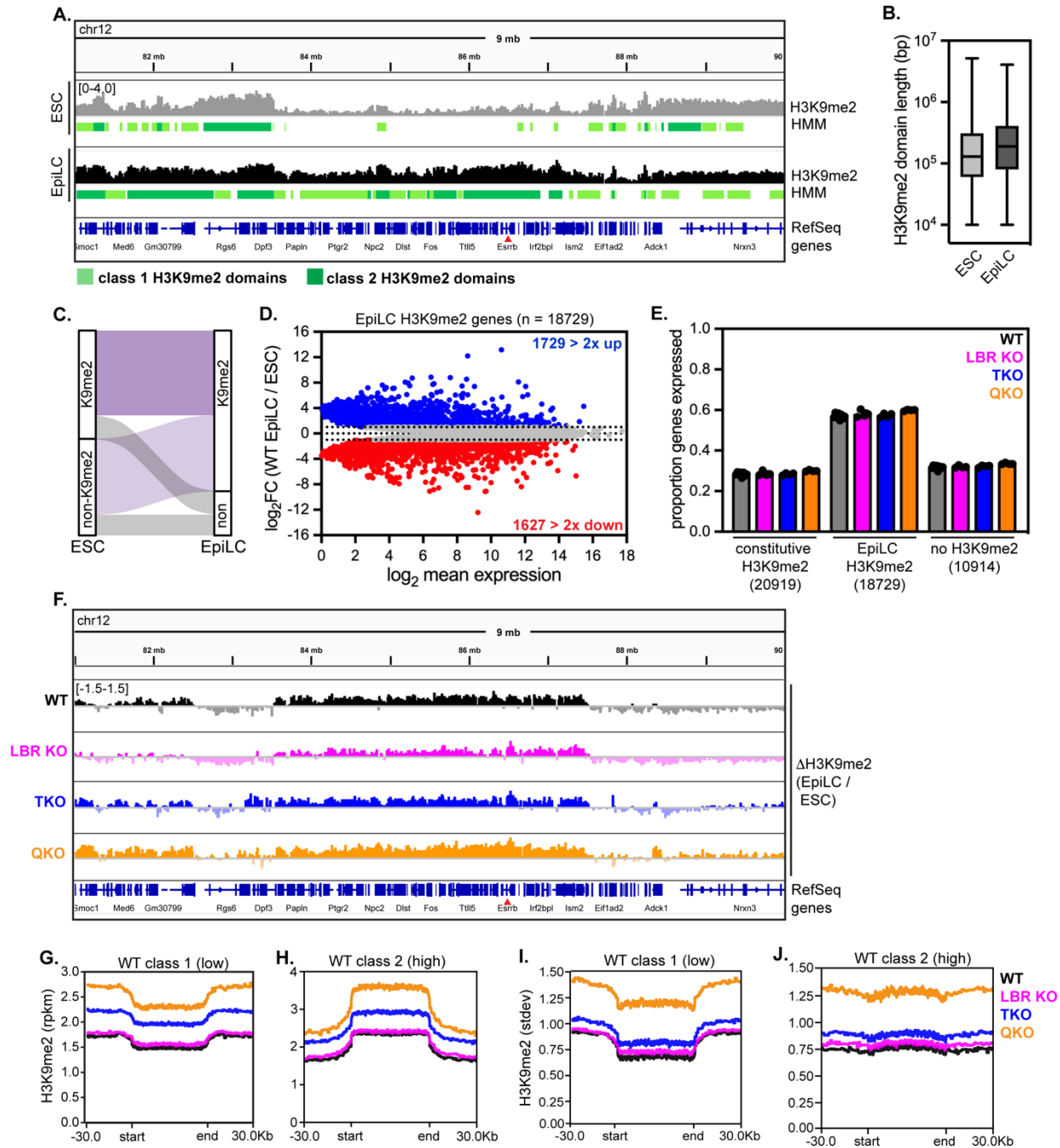


Figure 6 Abnormal deposition of H3K9me2 in Lamin + LBR KO EpiLCs.

(A) Representative genome tracks and domain calls for H3K9me2 in WT ESCs and EpiLCs on a 9 Mb section of chromosome 12, including the *Esrrb* gene. Y-axis range indicated at top left is the same for all tracks shown. Low K9me2 density “class 1” domains are marked in light green and high K9me2 density “class 2” domains are marked in dark green. (B) Median contiguous size of HMM class 1 (low K9me2 density) and class 2 (high K9me2 density) domains in WT ESCs versus EpiLCs. (C) Alluvial plots showing movement of genes into and out of H3K9me2 domains as WT ESCs differentiate into EpiLCs. Genes found in H3K9me2 domains in both ESCs and EpiLCs are referred to as “constitutive” (dark purple, 20919 genes) while genes that move into H3K9me2 domains in EpiLCs are referred to as “EpiLC H3K9me2” (light purple, 18729 genes). 10914 genes are not included in (continued on next page)

(continued from previous page) H3K9me2 domains in EpiLCs. (D) MA plot comparing expression of EpiLC H3K9me2 genes in WT EpiLCs versus mESCs. Of 18729 genes that move into EpiLC H3K9me2 domains, 7590 with $p_{adj} < 0.05$ are plotted; of these, 1729 genes are upregulated at least 2-fold and 1627 are downregulated at least 2-fold. (E) Proportion of genes expressed (minimum of 5 TPMs) within constitutive H3K9me2 domains, within EpiLC H3K9me2 domains, or outside of H3K9me2 domains across genotypes. (F) Difference maps of H3K9me2 signal in EpiLCs vs. ESCs across a 9 Mb section of chromosome 12. Y-axis range indicated at top left is the same for all tracks shown. (G-H) Averaged density of H3K9me2 in class 1 (G) and class 2 (H) domains (domain coordinates identified in WT EpiLCs). (I-J) Standard deviation of H3K9me2 signal in class 1 (I) and class 2 (J) domains (domain coordinates identified in WT EpiLCs).

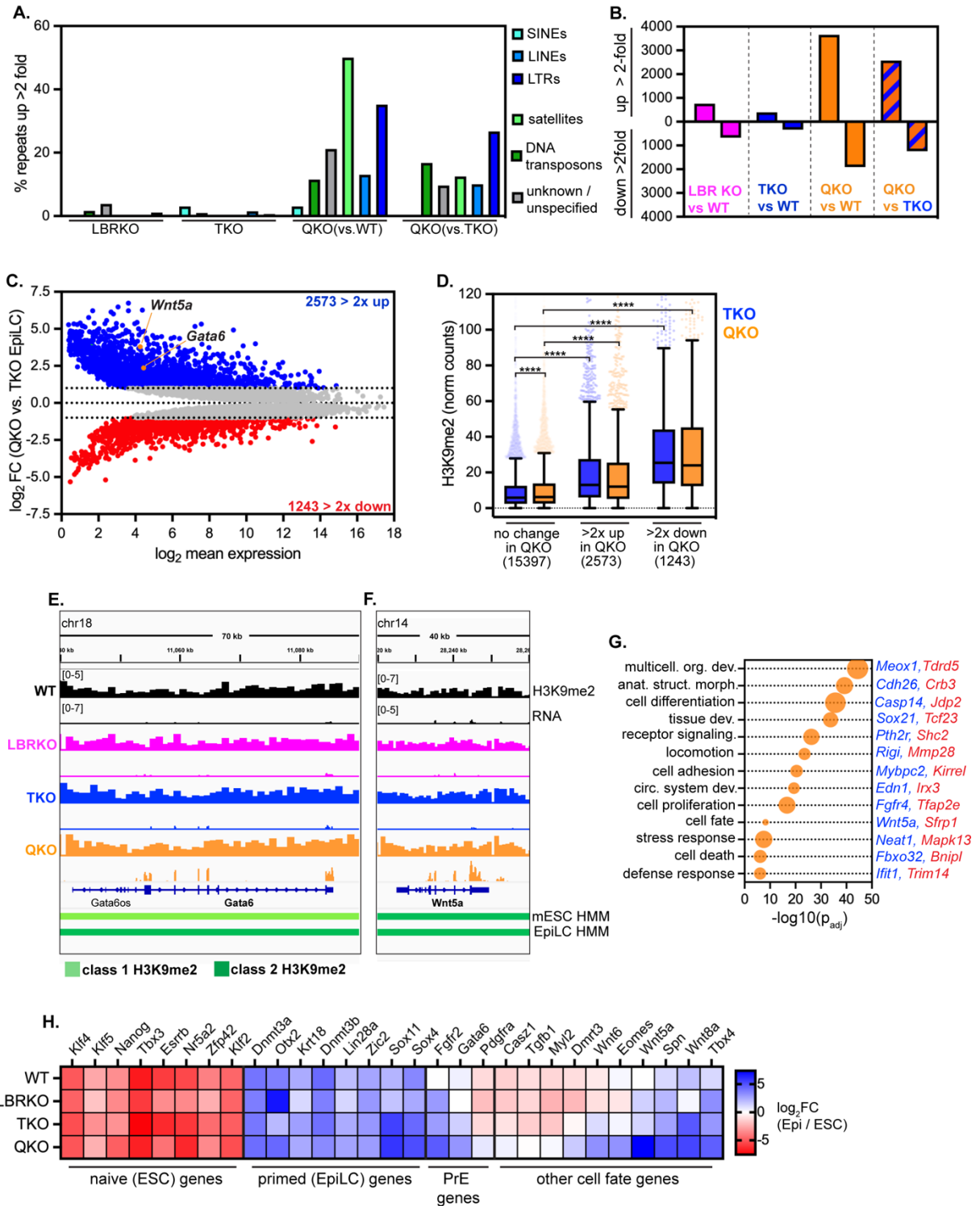
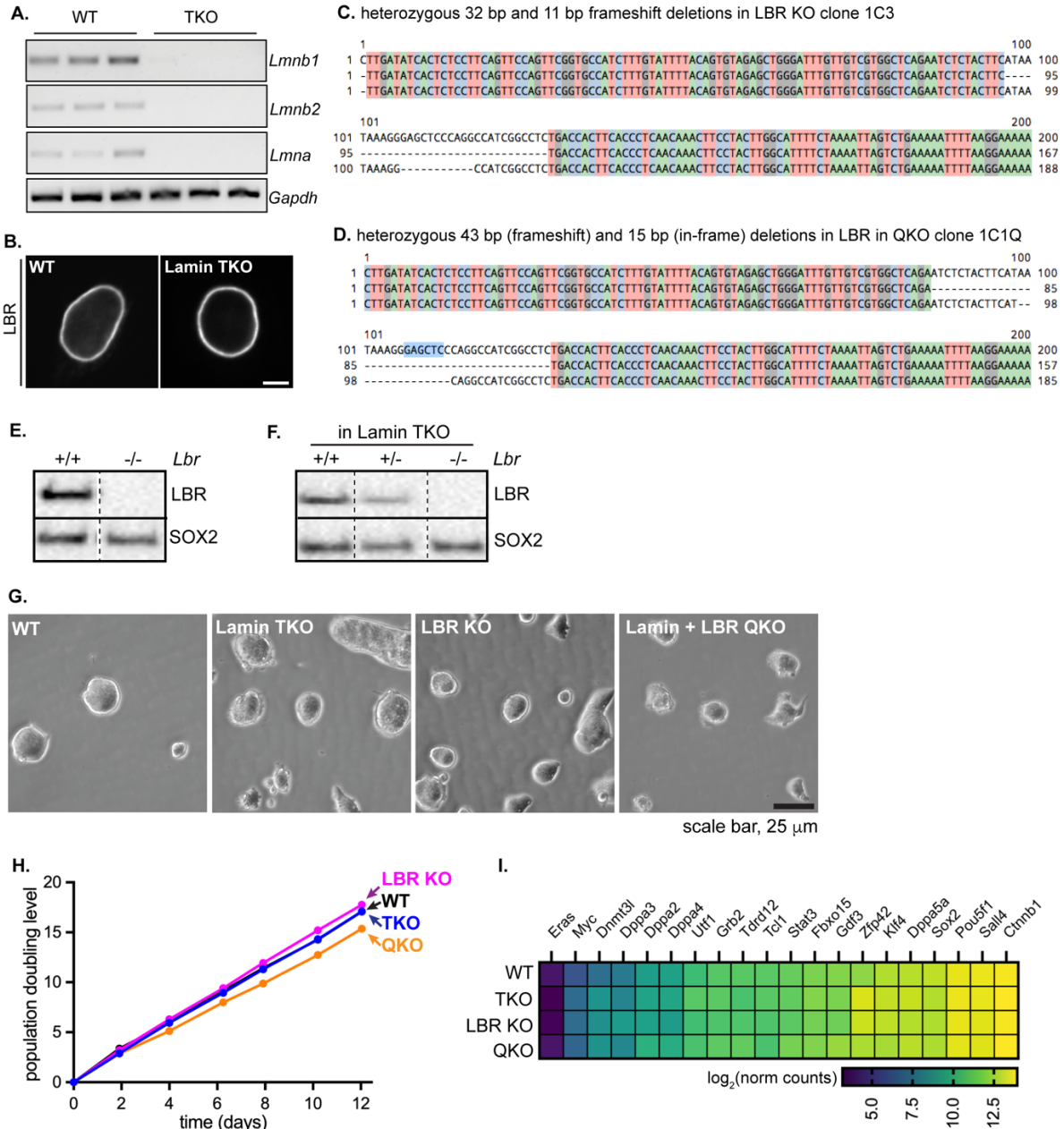


Figure 7 Removal of the lamins and LBR derepresses genes and transposons and impairs lineage restriction in EpiLCs.

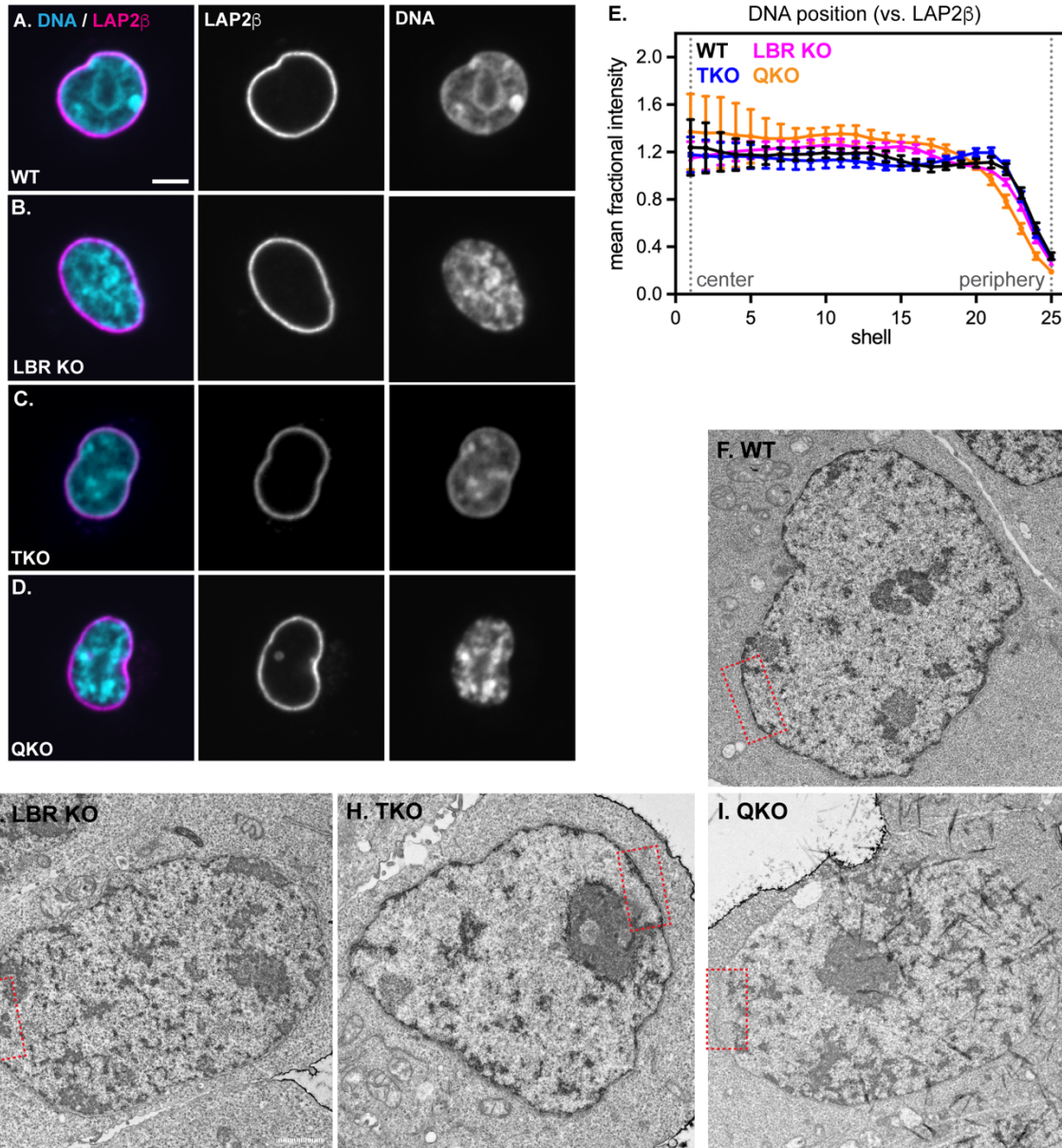
(A) Percentage of TE families de-repressed at least 2-fold in LBR KO, lamin TKO, and lamin + LBR QKO EpiLCs versus WT EpiLCs, and in lamin + LBR QKO EpiLCs versus TKO EpiLCs. (B) Number of genes significantly differentially expressed at least 2-fold in all genotypes compared to wildtype EpiLCs, (continued on next page)

(continued from previous page) and in lamin + LBR QKO EpiLCs compared to lamin TKO EpiLCs. (C) MA plot comparing gene expression in QKO versus TKO EpiLCs. 10051 genes with a minimum p_{adj} of 0.05 shown; 2573 genes are upregulated at least 2-fold, while 1243 genes are downregulated at least 2-fold. Representative H3K9me2-modified and de-repressed genes *Wnt5a* and *Gata6a* highlighted. (D) Analysis of H3K9me2 modification levels (normalized counts) on genes unchanged in expression between TKO and QKO EpiLCs (n = 15397), genes upregulated at least 2-fold in QKO EpiLCs (n = 2573), and genes downregulated at least 2-fold in QKO EpiLCs (n = 1243). **** indicates that comparisons indicated are significantly different ($p < 0.0001$) by Kruskal-Wallis multiple comparisons test with Dunn's correction. Box (Tukey) plot center line indicates median; box limits indicate 25th to 75th percentiles; whiskers indicate 1.5x interquartile range; points indicate outlier values. (E-F) H3K9me2 and RNA levels of H3K9me2 domain genes *Gata6* (E) and *Wnt5a* (F) across genotypes. Y axis ranges indicated at the top left of each panel are the same for all lower tracks within panel. (G) Gene ontology analysis of all genes significantly differentially expressed by at least 2-fold in QKO vs. TKO EpiLCs. Biological process GO terms identified with gProfiler and reduced by ReVIGO. Selection of list shown as bubble plot where size corresponds to number of DE genes associated with that term (ranging from 64 to 697 genes). Representative upregulated and downregulated genes that intersect with each GO term are highlighted in blue and red, respectively. See also Supplementary Table 2 for full list of GO terms. (H) Heatmap showing expression of selected genes associated with naïve pluripotency, primed pluripotency, primitive endoderm, or other cell fates in each genotype. Heatmap values indicate log₂(fold change) in expression between EpiLCs and ESCs.



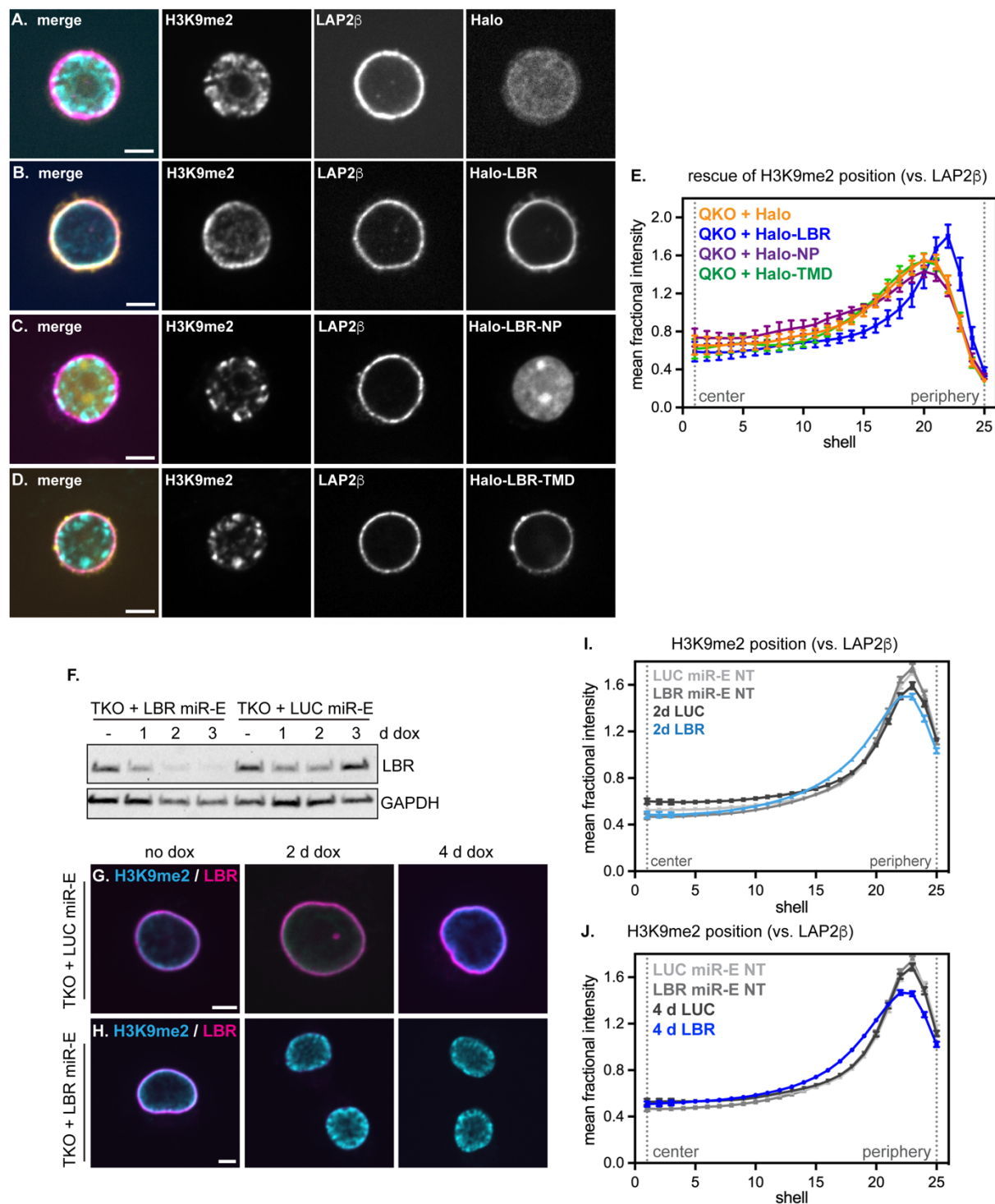
Supplementary Figure 1 Validation of knockout mESCs.

(A) PCR validation of *Lmna*, *Lmnb1*, and *Lmnb2* knockout in lamin TKO mESCs. (B) Immunofluorescence of LBR in WT and lamin TKO mESCs. Scale bar, 5 μm. Sanger sequencing and CRISP-ID tool analysis showing frameshift indels in LBR KO clone 1C3 (C) and lamin + LBR QKO clone 1C1Q (D). Western blot validation of LBR KO in WT ESC background (E) and in lamin TKO background (F). 10 mg of total protein lysate was loaded for all samples. (G) Colony morphology of WT, lamin TKO, LBR KO, and lamin + LBR QKO mESCs. Scale bar, 25 mm. (H) Growth rate analysis of WT, LBR KO, lamin TKO, and lamin + LBR QKO mESCs. (I) Expression of core pluripotency genes.



Supplementary Figure 2 Microscopy of knockout mESCs.

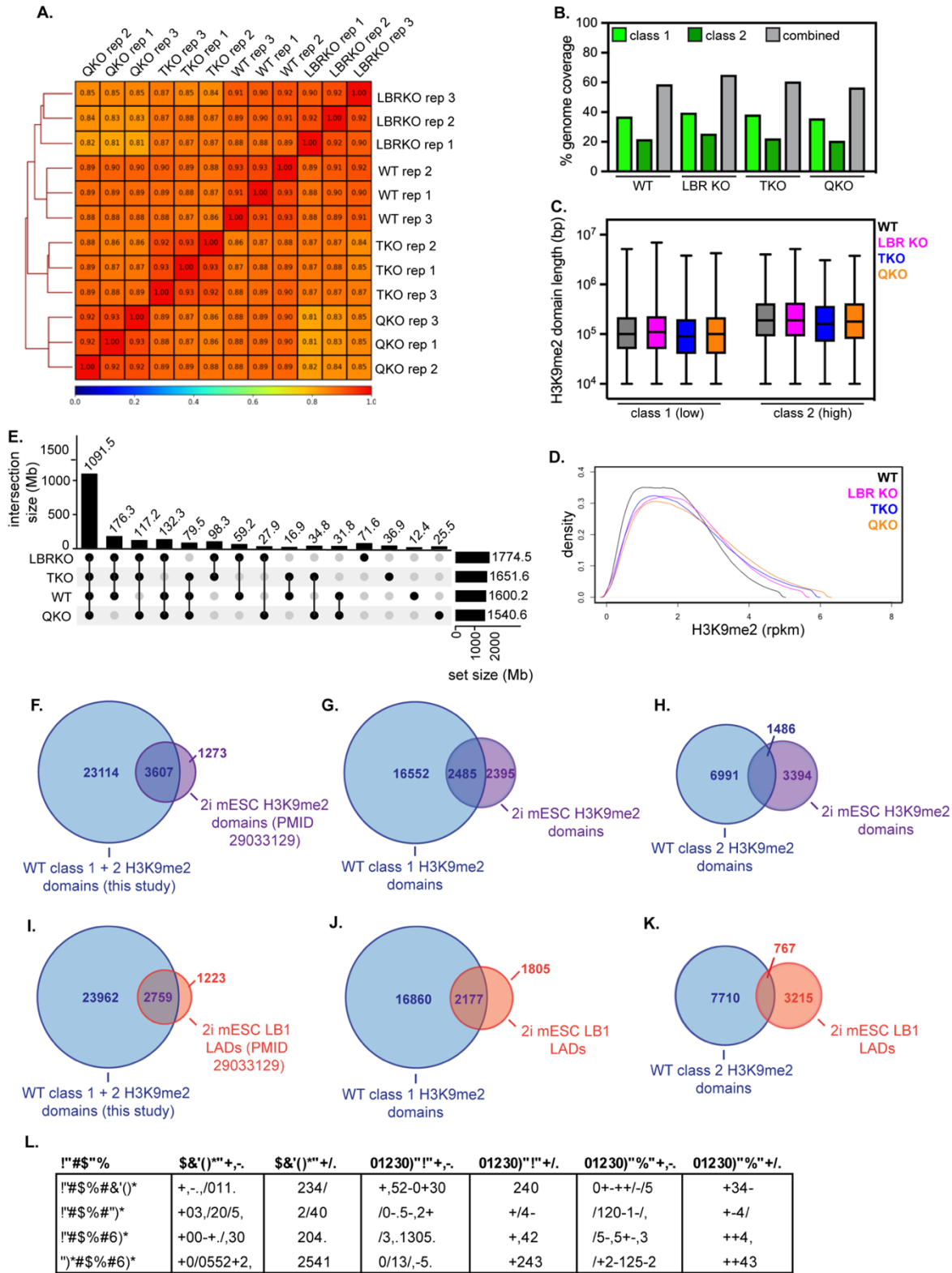
Immunofluorescence of DNA localization (Hoechst stain) compared to the INM protein (LAP2b) in WT (A), LBR KO (B), lamin TKO (C), and lamin + LBR QKO (D) mESCs. Central z-slices (XY) are shown. Scale bar, 5 μ m. (E) Radial intensity analysis of DNA position (Hoechst stain) in WT, TKO, LBR KO, and QKO mESCs. ** $p < 0.01$, WT vs QKO shells 8-19, **** $p < 0.0001$, WT vs QKO shells 21-25; * $p < 0.05$, WT vs LBR KO shells 14-18, ** $p < 0.01$, WT vs LBR KO shells 21-25; * $p < 0.05$, WT vs TKO shells 18-21. Transmission electron microscopy images showing full fields of view corresponding to Figure 1 for WT (F), LBR KO (G), lamin TKO (H), and lamin + LBR QKO (I) mESCs. Inset positions that appear in Figure 1 are shown in red dashed boxes.



Supplementary Figure 3 Displacement of H3K9me2 from the nuclear periphery is reversible.

Immunofluorescence of H3K9me2 localization compared to the INM protein (LAP2b) in lamin + LBR QKO mESCS expressing Halo-NLS (A), Halo-LBR (B), Halo-LBR nucleoplasmic domain (NP) (C), and Halo-LBR transmembrane domain (TMD) (D). Central z-slices (XY) shown. Scale bar, 5 μ m. (E) Radial intensity analysis of H3K9me2 position in QKO + Halo-NLS (n=27), QKO + Halo-LBR (n=16), QKO + Halo-TMD (n=17), (continued on next page)

(continued from previous page) and QKO + Halo-NP (n=26) 2 days after electroporation of plasmids. ** $p < 0.05$, Halo vs. Halo-LBR, shells 12-19; **** $p < 0.0001$, Halo vs. Halo-LBR, shells 22-25, unpaired t-test. ns, $p > 0.05$, Halo vs. Halo TMD and Halo vs. Halo NP in all shells. Points indicate mean and error bars indicate 95% confidence intervals. (F) Western blot showing LBR knockdown in lamin TKO mESCs expressing doxycycline-inducible LBR miR-E. Immunofluorescence of H3K9me2 (cyan) and LBR (magenta) in lamin TKO mESCs expressing LUC miR-E (G) or LBR miR-E (H). Scale bar, 5 μ m. (I) Radial intensity analysis of H3K9me2 position in TKO + LUC miR-E untreated (NT) (n=107), TKO + LUC miR-E + dox 2d (n=140), TKO + LBR miR-E NT (n=102), TKO + LBR miR-E + dox 2d (n=83), unpaired t-test. **** $p < 0.0001$, 2d LBR vs 2d LUC miR-E, shells 1-13, 16-21, 23-25. **** $p < 0.0001$, LBR NT vs 2d LBR miR-E, shells 11-20, 22-24, unpaired t-test. Points indicate mean and error bars indicate 95% confidence intervals. (J) Radial intensity analysis of H3K9me2 position in TKO + LUC miR-E NT (n=107), TKO + LUC miR-E + dox 4d (n=97), TKO + LBR miR-E NT (n=102), TKO + LBR miR-E + dox 4d (n=95), unpaired t-test. **** $p < 0.0001$, 4d LBR vs 4d LUC miR-E, shells 14-20, 22-25. **** $p < 0.0001$, LBR NT vs 4d LBR miR-E, shells 4-20, 22-24, unpaired t-test. Points indicate mean and error bars indicate 95% confidence intervals.

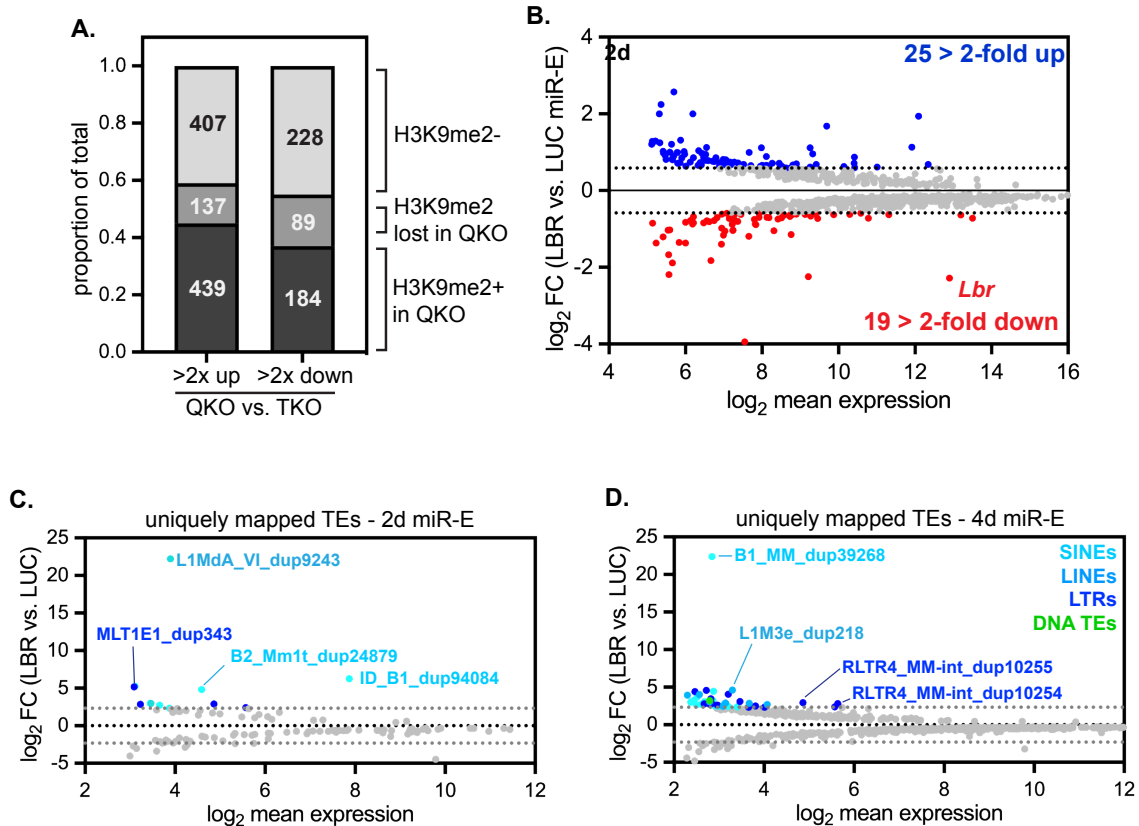


Supplementary Figure 4 Replicate clustering and analysis of H3K9me2 CUT & RUN in mESCs.

(Figure caption continued on the next page.)

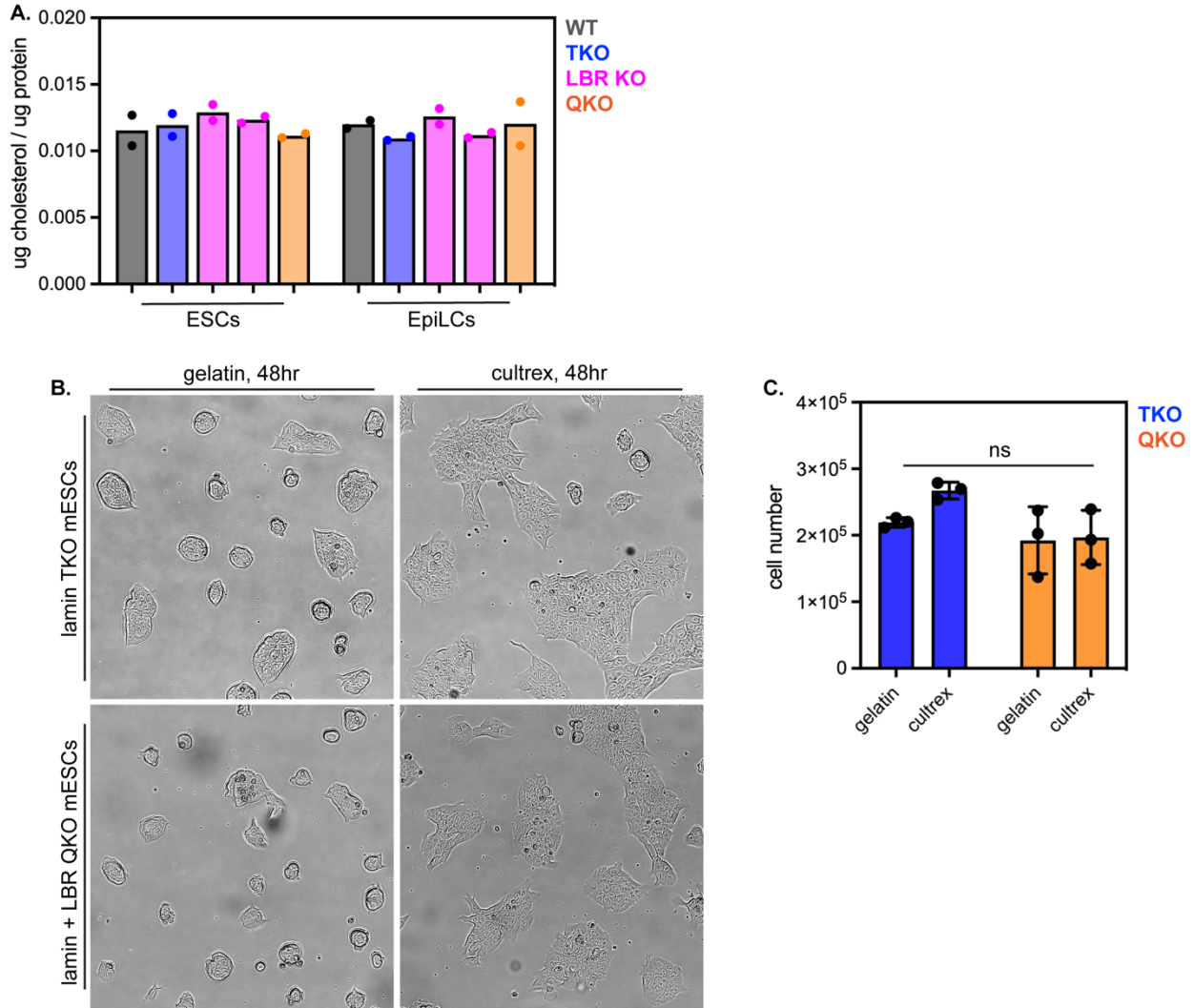
(Figure caption continued from the previous page.)

(A) Dendrogram and heatmap of individual H3K9me2 CUT & RUN replicates (3 per condition) showing similarity of replicates for each genotype. (B) Total genome coverage statistics for class 1 H3K9me2 domains, class 2 H3K9me2 domains, and merged H3K9me2 domains in each genotype of mESCs. (C) Genomic length of class 1 and class 2 H3K9me2 domains across genotypes. (D) Histogram of H3K9me2 signal intensity (rpkm) across genotypes. (E) UpSet plot showing all unique overlaps between datasets. (F) Overlap of genes within all merged H3K9me2 domains defined in this study versus in a previous analysis of H3K9me2 in mESCs in 2i + LIF culture conditions (PMID 29033129); 74% of the H3K9me2 genes identified in that study are also found in our dataset. (G) Overlap of genes within class 1 H3K9me2 domains defined in our study versus in PMID 29033129; 51% of the H3K9me2 genes identified in that study are also found in our class 1 H3K9me2 domains. (H) Overlap of genes within class 2 H3K9me2 domains defined in our study versus in PMID 29033129; 30% of the H3K9me2 genes identified in that study are also found in our class 2 H3K9me2 domains. (I) Overlap of genes within all merged H3K9me2 domains defined in our study versus in previously defined LADs (determined by LB1 ChIP-seq) in mESCs in 2i + LIF culture conditions (PMID 29033129); 70% of LB1 LAD genes are also found in H3K9me2 domains in our dataset. (J) Overlap of genes within class 1 H3K9me2 domains defined in our study versus in PMID 29033129; 55% of LB1 LAD genes are also found in our class 1 H3K9me2 domains. (K) Overlap of genes within class 2 H3K9me2 domains defined in our study versus in PMID 29033129; 20% of LB1 LAD genes are also found in our class 2 H3K9me2 domains. (L) Summary of overlapping and unique H3K9me2 domains in pairwise comparisons between genotypes.



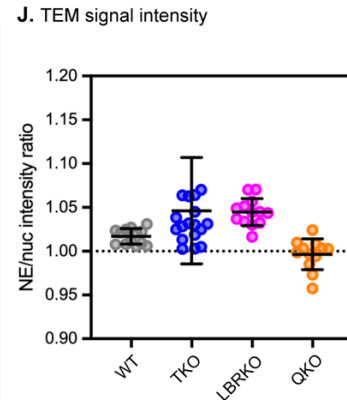
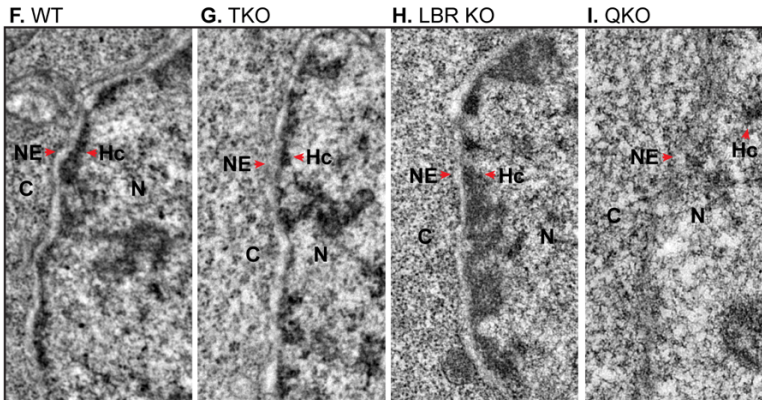
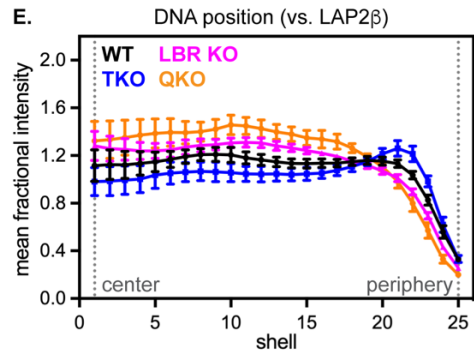
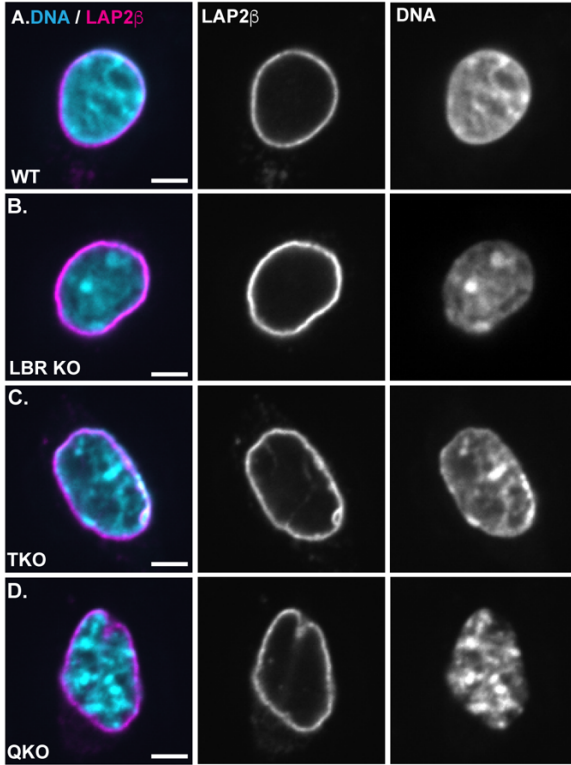
Supplementary Figure 5 Analysis of transcription after inducible knockdown of LBR in mESCs.

(A) Analysis of H3K9me2 modification status of genes that are significantly upregulated or downregulated in QKO vs. TKO mESCs, scored as H3K9me2+ (within H3K9me2 domain in QKO), H3K9me2 lost (within H3K9me2 domain in TKO but not QKO) or H3K9me2- (outside of H3K9me2 domains in both genotypes). (B) MA plot comparing gene expression in lamin TKO mESCs expressing LBR or LUC miR-E for 2 days; 778 genes with a minimum p_{adj} of 0.05 shown; 25 genes are upregulated at least 2-fold, while 19 genes are downregulated at least 2-fold. (C-D) MA plots comparing expression of unique TE copies in LBR miR-E versus LUC miR-E after 2 days (C) or 4 days (D). (C) 116 TEs with $p_{adj} < 0.05$ shown; 13 TEs were upregulated at least 5-fold, while 12 TEs were downregulated at least 5 fold. (D) 760 TEs with $p_{adj} < 0.05$ shown; 42 TEs were upregulated at least 5-fold, while 20 TEs were downregulated at least 5-fold. All repeats without a significant change between conditions are gray; significantly differentially expressed TEs (minimum 5-fold change) are colored correspondingly to TE family.



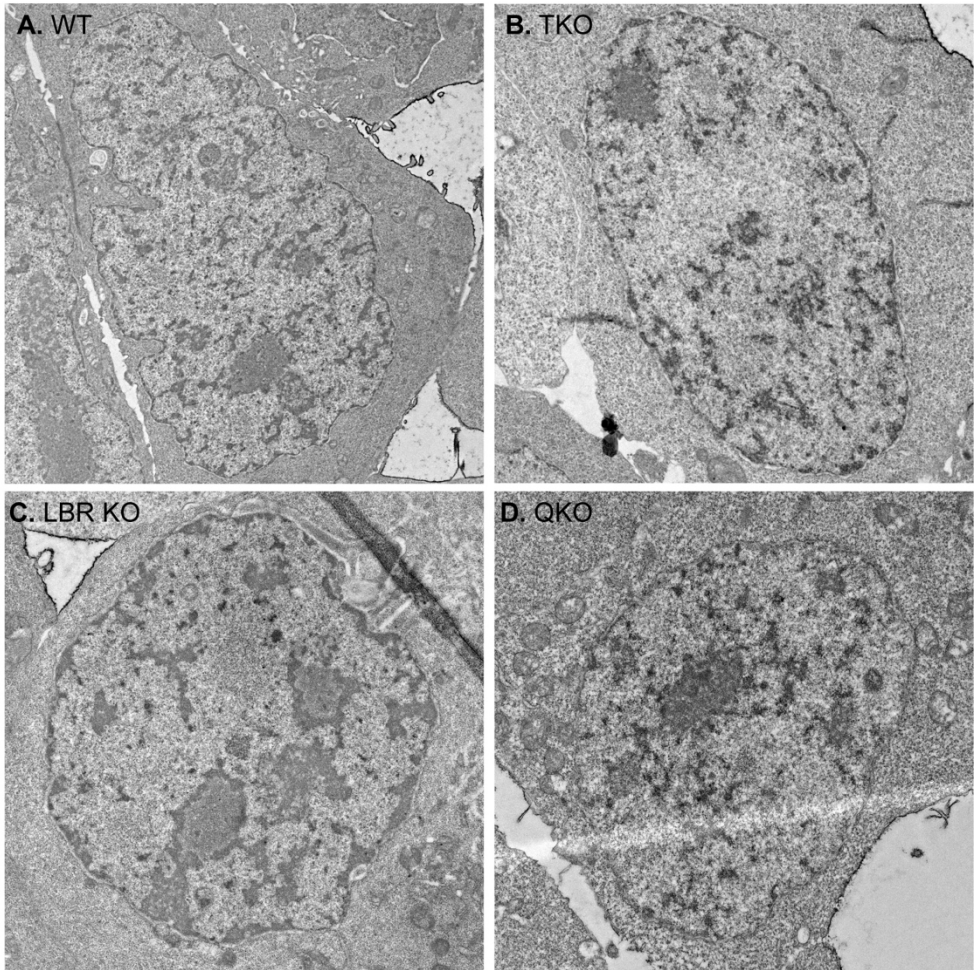
Supplementary Figure 6 Additional phenotypic profiling of mESCs.

(A) Representative brightfield microscopy images of lamin TKO and lamin + LBR QKO mESC colonies grown on either gelatin (colonies more rounded with lower attachment) or cultrex (colonies more flattened with higher attachment) for 2 days. (B) Cell numbers of lamin TKO and lamin + LBR QKO mESCs after 2 days of culture on gelatin or cultrex substrate. ns by one-way ANOVA across all conditions; TKO cell numbers are significantly increased on cultrex vs. gelatin ($p < 0.01$). (C) Analysis of cholesterol levels by Amplex Red assay in WT, lamin TKO, LBR KO, and lamin + LBR QKO mESCs and EpiLCs. $n = 2$ replicates per condition.

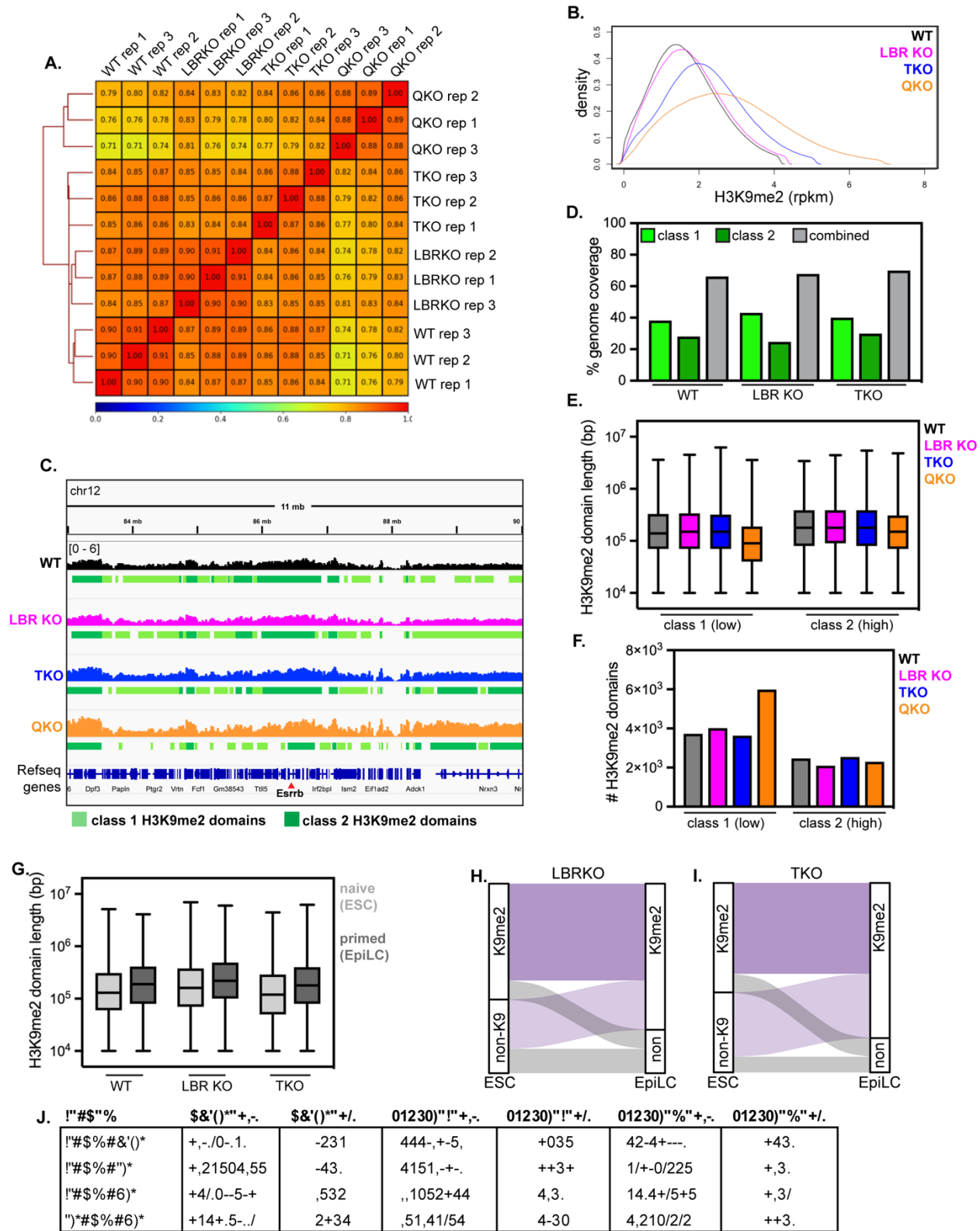


Supplementary Figure 7 Fluorescence and electron microscopy of EpiLCs.

Immunofluorescence of DNA localization (Hoechst stain) compared to the INM protein LAP2b in WT (A), LBR KO (B), lamin TKO (C), and lamin + LBR QKO (D) EpiLCs. (E) Radial intensity analysis of DNA position (vs. LAP2b) in WT, TKO, LBR KO, and QKO EpiLCs. ** $p < 0.01$, WT vs QKO shells 5 – 18, **** $p < 0.0001$, WT vs QKO shells 21-25; * $p < 0.05$, WT vs LBR KO shells 8-10, ** $p < 0.01$, WT vs LBR KO shells 11-17, *** $p < 0.001$, WT vs LBR KO shells 20-25; ** $p < 0.01$, WT vs TKO shells 7-16, *** $p < 0.001$, WT vs TKO shells 21-23. Transmission electron microscopy showing 1.3 mm by 2.6 mm section of the nuclear periphery in WT (F), lamin TKO (G), LBR KO (H), and lamin + LBR QKO (I) EpiLCs. C, cytoplasm; N, nucleus; NE, nuclear envelope; Hc, heterochromatin. (K) Quantification of relative TEM signal intensity at the NE versus the nucleoplasm for WT (n = 13), LBRKO (n = 18), TKO (n = 13), and QKO (n = 12) EpiLCs.



Supplementary Figure 8 Uncropped TEM images of WT, TKO, LBRKO, and QKO EpiLCs.

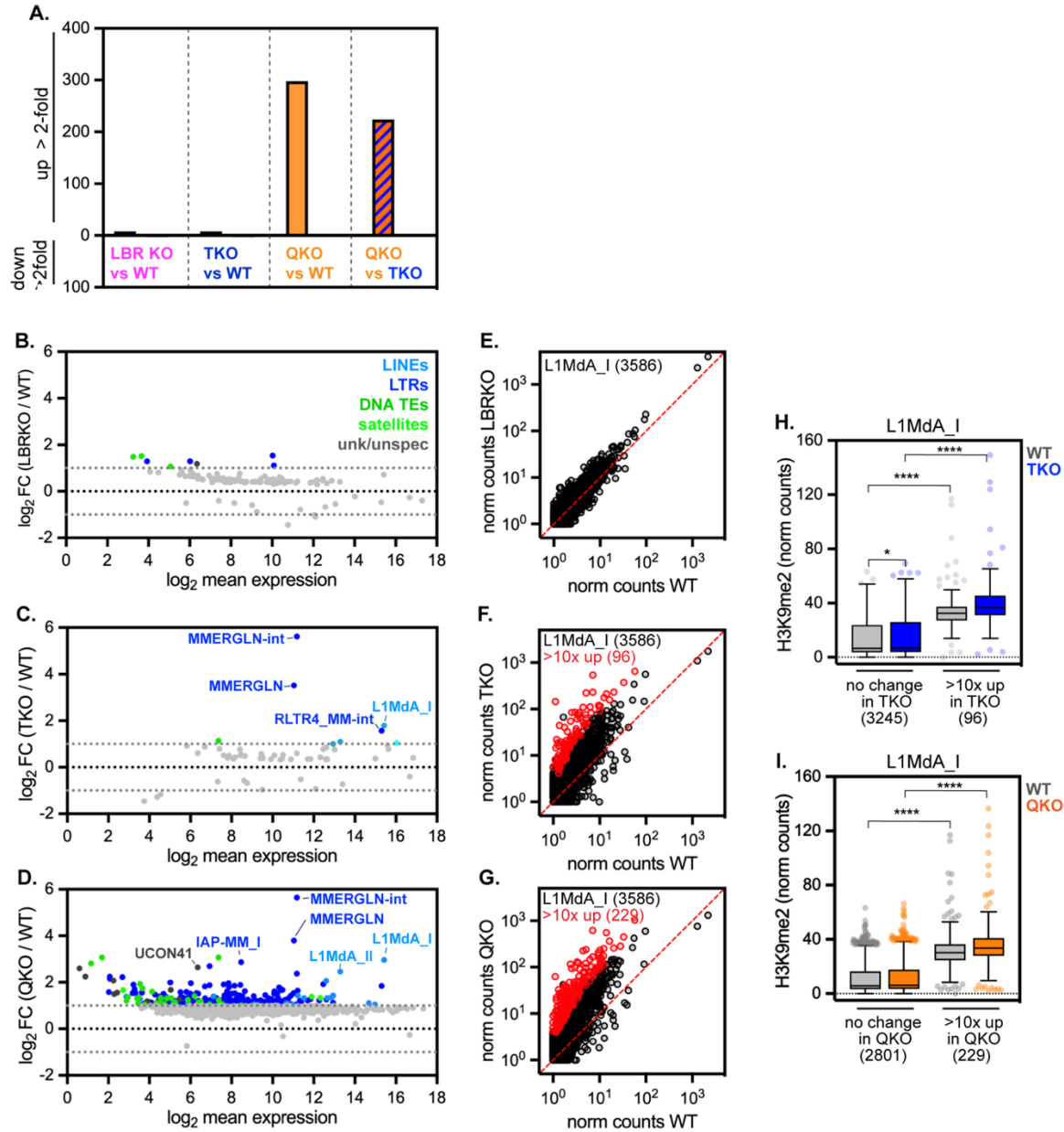


Supplementary Figure 9 Replicate clustering and analysis of H3K9me2 CUT & RUN in EpiLCs.

(Figure caption continued on the next page.)

(Figure caption continued from the previous page.)

(A) Dendrogram and heatmap of individual H3K9me2 CUT & RUN replicates (3 per condition) showing similarity of replicates for each genotype. (B) Histogram of H3K9me2 signal intensity (RPKM) across genotypes. (C) Representative genome tracks and domain calls for H3K9me2 in WT, LBR KO, TKO, and QKO ESCs on a 11 Mb section of chromosome 12, including the *Esrrb* gene. Y-axis range indicated at top left is the same for all tracks shown. Low K9me2 density “class 1” domains are marked in light green and high K9me2 density “class 2” domains are marked in dark green. (D) Total genome coverage statistics for class 1 H3K9me2 domains, class 2 H3K9me2 domains, and merged H3K9me2 domains in each genotype of EpiLCs. (E) Size of class 1 and class 2 domains in each genotype. (F) Number of class 1 and class 2 H3K9me2 domains called in each genotype. (G) Total contiguous merged length of H3K9me2 domains in WT, LBRKO, and TKO EpiLCs versus ESCs. (H-I) Alluvial plots showing movement of genes into and out of H3K9me2 domains as LBRKO (H) and lamin TKO (I) ESCs differentiate into EpiLCs. Genes found in H3K9me2 domains in both ESCs and EpiLCs are referred to as “constitutive” (dark purple) while genes that move into H3K9me2 domains in EpiLCs are referred to as “EpiLC H3K9me2”. (J) Summary of overlapping and unique H3K9me2 domains in pairwise comparisons between genotypes.



Supplementary Figure 10 Analysis of TE expression in WT, TKO, LBRKO, and QKO EpiLCs.

(A) Summary of TEs upregulated >2-fold in LBRKO, TKO, and QKO EpiLCs. (B) MA plot of individual TE expression in LBRKO vs. WT EpiLCs. (B) 119 TEs, (C) 56 TEs, and (D) 950 TEs with $p_{adj} < 0.05$ shown; TEs upregulated at least 2-fold are colored according to TE family. (E-G) Normalized counts for 3586 uniquely mapped L1MdA_I LINE element genomic copies in (E) LBRKO versus WT mESCs, (F) TKO versus WT mESCs, and (G) QKO versus WT mESCs (plotted as $\log_{10}(\text{average} + 1)$). L1MdA_I copies with >10-fold change and significant difference in expression ($p_{adj} < 0.05$) in are colored in red. (H-I) Normalized counts from uniquely mapped reads of H3K9me2 on L1MdA_I LINE elements with unchanged expression versus those upregulated >10-fold in TKO mESCs (H, $n = 96$) and in QKO mESCs (I, $n = 229$). **** indicates $p < 0.0001$ and * indicates $p = 0.0294$ by Kruskal-Wallis multiple comparisons test with Dunn's correction. Box (Tukey) plot center line indicates median; box limits indicate 25th to 75th percentiles; whiskers indicate 1.5x interquartile range; points indicate outlier values.

Materials and Methods

Generation of Knockout and miR-E Expressing mESCs

Lamin triple knockout (vial “TKO97,” passage 12) and littermate wildtype (vial “28538,” passage 9) mESCs were obtained as a generous gift from the laboratory of Dr. Yixian Zheng¹¹⁹. Cell lines tested negative for mycoplasma and they were karyotyped by WiCell. Lamin triple knockout mESCs had an abnormal karyotype with two predominant clonal populations: one having trisomy 8, and the other having trisomy 8 and loss of the Y-chromosome. The population of littermate wildtype cells had a 75% normal ploidy with two aneuploid populations: one with loss of the Y-chromosome, and the other with trisomy 6 and 8 and loss of the Y-chromosome.

Lbr knockout was performed by lipofectamine transfection of the PX458 CRISPR/Cas9 plasmid (Addgene #48138) with one guide targeting exon 2 of Lbr (TCATAATAAAGGGAGCTCCC). Transfections were carried out by lipofectamine 2000 (Invitrogen™ 11668019) for Lbr knockout and by electroporation with the Neon™ Transfection System (Invitrogen™ MPK5000) for Lbr rescue experiments using the manufacturer’s procedures. Cells were allowed to recover for 48hrs, then sorted by GFP fluorescence and seeded on a 10-cm dish at a density of 3,000 cells per dish. mESCs were grown for a week until visible colonies appeared, then colonies were picked by pipetting into 96-well plates for screening and further expansion.

The CRISPR guide for Lbr knockout was designed to overlap a restriction enzyme site *SacI* near the cutting site of Cas9 such that indels would destroy the site. Genotyping was performed by PCR amplification of gDNA with primers flanking the *SacI* site, then followed by *SacI* digestion of the PCR product and running the digest on a 2% agarose gel. Homozygous indels were scored by the presence of one band at 1388bp. Heterozygous indels were scored by the presence of three bands at 1388bp, 938bp, and 450bp. Unedited fragments were scored by the presence of two band at 938bp and 450bp. This strategy yielded 36 homozygous Lbr indel clones out of 78 screened in wildtype mESCs, and 10 homozygous Lbr indel clones out of

85 screened in TKO mESCs. The presence of indels was verified by Sanger sequencing and analysis with CRISP-ID¹²⁰. Lbr protein depletion was validated by Western blot with an LBR antibody (cat. ab232731).

To make mESCs expressing tetracycline-inducible miR-Es targeting Lbr or Luc, puromycin, hygromycin, and neomycin resistance markers were first excised from lamin TKO mESCs by transient expression of Cre recombinase and clonal selection. Cre recombinase was expressed from a plasmid derived from pPGK-Cre-bpA (Addgene #11543) with an SV40polyA sequence instead of the bpA. Then, 97mer oligos were ordered containing miR-E targeting LBR (“LBR634” 5'-TGCTGTTGACAGTGAGCGCCAGATATATAGTTACACAGTATAGTGAAGCCACAGATGATACTGTGTA ACTATATATCTGTTGCCTACTGCCTCGGA-3') and Renilla Luciferase (5'-TGCTGTTGACAGTGAGCGCAGGAATTATAATGCTTATCTATAGTGAAGCCACAGATGTATAGATAAGCATTATAATTCCTATGCCTACTGCCTCGGA-3'). These were amplified by two miR-E universal primers (fwd 5'-CTTAACCCAACAGAAGGCTCGAGAAGGTATATTGCTGTTGACAGTGAGCG-3') (rev 5'-ACAAGATAATTGCTCGAATTCTAGCCCCTTGAAGTCCGAGGCAGTAGGCA-3') and cloned into the XhoI and EcoRI double digested LT3GEPIR lentiviral vector (Addgene #111177). HEK293T cells were transfected with these vectors to produce lentivirus which was then used to transduce lamin TKO mESCs. Cells were selected with puromycin (1µg/mL) for 4 days, then individual clones were selected. Using flow cytometry, GFP signal after doxycycline treatment (1µg/mL) was measured to assess the expression of the RNAi system. Clones with a GFP-positive population greater than 88% were selected for experiments.

mESC culture and EpiLC differentiation

mESCs were cultured in 5% CO₂ and 37°C under normoxic conditions. mESCs were grown in serum- and feeder-free 2i + LIF medium (N2B27 basal medium, 3 µM CHIR-99021 (Selleckchem S1263), 1 µM PD0325901 (Selleckchem S1036), 10³ U/mL LIF (MilliporeSigma™ ESG1107), 55 µM β-mercaptoethanol (Gibco™ 21985023), and 1X PenStrep (GenClone 25-512).) N2B27 medium was made by mixing equal parts of DMEM:F12 (GenClone 25-503) and

Neurobasal medium (Gibco™ 21103049) then adding 1X N-2 (Gibco™ 17502001), 1X B-27 (Gibco™ 17504001) and 2 mM Glutamax (Gibco™ 35050061). Dishes were coated with 0.1% gelatin (MilliporeSigma ES-006-B) for 30 minutes at 37°C before seeding cells. Serum-free 2i + LIF media was replenished every day and cells were passaged every other day, seeding 4×10^5 cells per 6-well (approximately 4.21×10^4 cells/cm²).

Differentiation of mESCs into epiblast-like cells was adapted from a published protocol¹²¹. Briefly, a 6-well was coated with 1 mL of a 1:200 solution of either Geltrex (Gibco™ A1413202) or Cultrex (Bio-Techne 3445-005-01) in N2B27 at 37°C. After one hour, that solution was aspirated and 2×10^5 mESCs were seeded (approximately 2.11×10^4 cells/cm²) with N2B27 media containing a final concentration of 20 ng/mL FGF (Peprotech 100-18B) and 12 ng/mL Activin A (Peprotech 120-14E). This EpiLC media was replenished the next day. For miR-E timepoints followed by RNA-seq, mESCs were seeded at 4.21×10^4 cells/cm² on dishes pre-coated with 0.1% gelatin. mESCs were replenished with fresh 2i + LIF medium every day. Untreated controls were collected after 2 days. Treated cells received doxycycline at 1 µg/mL. For day 4 doxycycline timepoints, mESCs were split at day 2, keeping the same seeding density.

RNA Isolation and Library Preparation for RNA-seq

Four replicates, each consisting of a single 6-well of cells, were used per condition for all RNAseq experiments. Total RNA was isolated using the RNeasy Plus Mini Kit (QIAGEN 74136). RNA was treated with DNase using the TURBO DNA-free kit (Invitrogen™ AM1907) prior to prepping libraries. RNA quality was assessed by electrophoresis on a 1% agarose gel and detecting 28S and 18S rRNA bands with ethidium bromide staining (0.6 µg/mL). Libraries were prepped using the Illumina Stranded Total RNA Prep with Ribo-Zero Plus kit (Illumina 20040525) following the manufacturer's protocol with a starting RNA input of 500ng. Libraries were amplified using 11 cycles on the thermocycler. Each library was uniquely indexed with IDT for Illumina–DNA/RNA UD Indexes (Illumina 20026121), then pooled together in equimolar

amounts. Library concentration was measured using the Qubit dsDNA HS assay kit (Invitrogen Q32851) and Qubit 4 fluorometer. Library size was assayed using the Agilent Bioanalyzer 2100 with the High sensitivity DNA kit (Agilent 5067-4626). Paired-end sequencing was performed on the pooled library using the Illumina NextSeq2000 platform (read length of 150bp and read depth of approximately 50 million reads per library).

For the LBR depletion timecourse, total RNA was isolated using the RNeasy Plus Mini Kit. The Tecan Genomics' Universal Plus mRNA prep kit (Tecan Genomics 0520B-A01) was modified for rRNA depletion by replacing the mRNA isolation in the first segment of the protocol with ribo depletion using FastSelect rRNA (Qiagen 334387) as follows: 200ng of total RNA in 10µL of water was mixed with 10µL of Universal Plus 2X Fragmentation Buffer and 1µL FastSelect. The solutions were fragmented and ribo-depleted simultaneously per the FastSelect protocol. 20µL of the resulting fragmented/ribo depleted RNA were prepped per the Universal Plus protocol starting with First Strand Synthesis. The Universal Plus Unique Dual Index Set B was used, and the samples were quality checked using a MiniSeq benchtop sequencer (Illumina). Normalized pools were made using the corrected protein coding read counts of each. All concentrations and library/pool qualities were measured via Fragment Analyzer (Agilent Technologies). Paired-end sequencing was performed on pooled libraries using the Illumina NovaSeq6000 platform at the UCSF CAT core (read length of 100bp and read depth of approximately 30 million reads per library).

RNA-seq Analysis

Raw sequencing reads were trimmed of the first T overhang using cutadapt¹²² (version 2.5) as suggested by Illumina. Trimmed reads were mapped to the GENCODE primary assembly M30 release of the mouse genome (GRCm39) using STAR¹²³ (version 2.7.10a): --runMode alignReads --readFilesCommand zcat --clip3pAdapterSeq CTGTCTCTTATA CTGTCTCTTATA --clip3pAdapterMMp 0.1 0.1 --outFilterMultimapNmax 1 --outSAMtype BAM SortedByCoordinate --twopassMode Basic. Bam files were indexed with SAMtools¹²⁴ (version

1.10). The deepTools2¹²⁵ (version 3.4.3) function bamCoverage was used to generate RPKM normalized coverage track files. The subread featureCounts¹²⁶ package (version 1.6.4) and GENCODE M30 primary annotation file was used to generate a read counts table for all conditions, which was used as an input for DESeq2¹²⁷ (version 1.40.2) to obtain normalized counts and perform differential gene expression analysis following a published pipeline which we adapted for mouse (doi.org/ 10.5281/zenodo.3985046). The subread featureCounts package was used again for obtaining read counts on uniquely mapped transposable elements using a custom annotation file made by the Hammell lab (https://labshare.cshl.edu/shares/mhammellab/www-data/TEtranscripts/TE_GTF/GRCm39_GENCODE_rmsk_TE.gtf). For Lbr depletion, reads were not trimmed of the first T overhang, but downstream analysis remained the same.

For multimapping of RNA-seq reads, as recommended by the TEtranscripts¹²⁸ authors, STAR parameters were changed from `--outFilterMultimapNmax 1` to the following: `--outFilterMultimapNmax 100 --winAnchorMultimapNmax 100`. A read counts table was generated using the TEcount command from the TEtranscripts package (version 2.2.3) with the following parameters: `--sortByPos --format BAM --mode multi`. The GENCODE M30 primary annotation file was used for gene annotations and a custom annotation file from the Hammell lab for transposable elements were used to generate a read counts table. DESeq2 analysis was carried out as before.

GO term analysis was performed with Gprofiler¹²⁹. Redundant terms were filtered with ReVIGO¹³⁰.

CUT&RUN and Library Preparation

CUT&RUN was performed as described in Skene et al. 2018¹³¹. Live cells were harvested with accutase and washed once with PBS prior to starting the procedure. Three replicates containing 200,000 mESCs or EpiLCs each were used per condition plus 2,000 HEK293T cells as a spike-in control. H3K9me2 antibody (abcam 1220) was used at 1:100

dilution in antibody buffer. Primary antibody incubation was performed at 4°C overnight. Rabbit anti-mouse secondary antibody (abcam ab6709) was used at 1:100 dilution and incubated for 4°C for 1 hour. pA-MNase (batch #6 143µg/mL) generously gifted from the Hennikoff lab was used for the cleavage reaction.

DNA was isolated by phenol-chloroform extraction. Purified DNA was resuspended with 40µL of 1mM Trish-HCl pH 8.0 and 0.1mM EDTA. DNA concentration was measured using the Qubit dsDNA HS assay kit (Invitrogen Q32851) and Qubit 4 fluorometer. DNA quality was assayed using the Agilent Bioanalyzer 2100 with the High sensitivity DNA kit. Libraries were prepared using the NEBNext Ultra II DNA Library Prep with Sample Purification Beads (NEB E7103S) following the manufacturer's protocol with 5ng of starting DNA input. Libraries were amplified using 8 cycles on the thermocycler. Each library was uniquely indexed with NEBNext Multiplex Oligos for Illumina (NEB E6440S), then pooled together in equimolar amounts. Library size was analyzed with the Agilent Bioanalyzer 2100 using the High sensitivity DNA kit. Paired-end sequencing was performed on the pooled library using the Illumina NextSeq2000 platform (read length of 35bp and read depth of approximately 16 million reads per library).

CUT&RUN Analysis

Raw sequencing reads were mapped to the "soft masked" mm39 mouse genome using Bowtie2¹³² (version 2.3.5.1): -X 2000 -N 1 --local --dovetail. SAMtools was used to keep properly paired, primary alignments and filter out unassembled contigs, read duplicates, and reads mapped to mitochondria.

For spike-in control scale factor calculations, raw sequencing reads were mapped to the "soft masked" hg38 human genome. As was done for mm39, Bowtie2 and SAMtools were used for alignment and post-alignment processing, respectively. The SAMtools function flagstat was used to find the number of properly paired reads in hg38 alignments. These were used to calculate a scale factor that was defined by dividing an arbitrary constant number (30,000) by the number of properly paired reads (Zheng Y et al (2020). Protocol.io). The scale factors for

each library were used to generate bigWig files of 1kb and 10kb bin, spike-in normalized RPKM signal coverage tracks with the deepTools2 function bamCoverage. Four-state hidden Markov models were implemented on each 10kb bin bigwig file with the pomegranate¹³³ (version 0.12) package to call four regions of different H3K9me2 signal 1. background signal 2. low signal 3. high signal and 4. very high artifact signal representative of “blacklist” regions. For each condition, replicate BED files containing low (class 1) and high (class 2) H3K9me2 domains were merged using the pybedtools¹³⁴ (version 0.8.1) function multiinter. For each condition, replicate 1kb bigWig files were averaged using deepTools2 function bigwigAverage. From these files, H3K9me2 density in domains were plotted using deepTools2 functions computeMatrix and plotProfile; Kernel density plots were made in base R (version 4.3.1). The subread featureCounts package was used to generate a read counts table for all conditions. For obtaining read counts in genes, the GENCODE M30 primary annotation file was used; for obtaining read counts in transposable elements, the same custom annotation from the Hammell lab was used (see RNA-seq analysis). DESeq2 was used to normalize the raw counts table by library size.

Immunoblot Assay

Frozen cell pellets were lysed with an aqueous buffer containing 8M Urea, 75mM NaCl, 50mM Tris pH 8.0, and one tablet of cOmplete™, Mini, EDTA-free Protease Inhibitor Cocktail (Roche 11836170001). Lysates were run on 4–15% Mini-PROTEAN® TGX™ Precast Gels (BIO-RAD 4561083) and blots were probed with anti-LBR (1:1000, abcam ab232731) and anti-SOX2 (1:1000, abcam ab97959) primary antibodies in 5% milk TBST. Anti-mouse HRP-conjugated (Rockland 610-1302) and anti-rabbit HRP-conjugated (Rockland 611-1302) secondary antibodies were used at 1:5000. Blots were visualized using Pierce™ ECL Western Blotting Substrate (Thermo Scientific™ 32209).

Cholesterol Quantification Assay

mESCs (2×10^6 cells per sample) were lysed in 250 μ L buffer containing 25 mM HEPES pH 7.4, 150 mM NaCl, 1% Triton-X-100, 0.1% SDS, and cOmplete™, Mini, EDTA-free Protease Inhibitor Cocktail (Roche 11836170001). Lysate was clarified by centrifugation at 10,000 rpm for 10 minutes at 4°C. To determine cholesterol levels, 10 μ L of each clarified lysate was analyzed with the Amplex™ Red Cholesterol Assay Kit (Invitrogen A12216) according to the manufacturer's instructions.

Immunofluorescence and Halo Tag Staining

IBIDI chambers (Ibidi USA 80826) were coated with 150 μ L of a 1:200 solution of Geltrex or Cultrex in N2B27 for 1 hour at 37°C. To obtain well-isolated cells for optimal imaging, 3×10^4 cells in 250 μ L media were seeded into each well and allowed to attach in the tissue culture incubator. After approximately 7 hours, mESCs were washed with PBS then fixed with a fresh solution of 4% formaldehyde (Thermo Scientific™ 28908) in PBS for 5 minutes. Cells were washed then stored at 4°C until staining.

For visualizing Halo-tagged constructs, cells were stained before fixation. Briefly, cells were cultured at 37°C 5% CO₂ with 2i + LIF medium containing 200nM of Janelia Fluor 549 HaloTag ligand (Promega GA1110). After 30 minutes, the media was replaced for N2B27 media and cells were incubated for 5 minutes. Finally, to remove background staining, N2B27 was replaced for 2i + LIF medium and cells were cultured for 1 hour in the incubator until fixation. Fixed cells were permeabilized in immunofluorescence buffer containing 0.1% Triton X-100, 0.02% SDS, 10mg/mL BSA in PBS. Primary and secondary antibodies were diluted in immunofluorescence buffer and incubated at room temperature for 2 hours and 1 hour, respectively, with immunofluorescence buffer washes in between antibodies. DNA was stained with Hoechst alongside the secondary antibody incubation. Primary antibodies used were H3K9me2 (1:300, abcam ab1220), H3K9me2 (1:1000, ActiveMotif 39041), LAP2 (1:400, Invitrogen PA5-52519), LBR (1:500, abcam ab232731). Secondary antibodies used were anti-

mouse Alexa Fluor 488 (1:1000, Invitrogen A-11029), anti-rabbit Alexa Fluor 488 (1:1000, Invitrogen A-11008), anti-mouse Alexa Fluor 568 (1:1000, Invitrogen A-11004), anti-rabbit Alexa Fluor 568 (1:1000, Invitrogen A-11011).

Image Acquisition and Analysis

Confocal images were taken using a Nikon spinning disk confocal microscope with a 60 × 1.4 numerical aperture, oil objective. Images were acquired as 0.3µm step Z-stacks with a range of 20 to 50 steps per cell. Unprocessed 16-bit images were saved as ND2 files using the Nikon Elements 5.02 build 1266 software. FIJI was used for cropping, producing max intensity projections, z-slices and converting images to TIFF files. CellProfiler¹³⁵ was used to quantify signal intensity (“MeasureObjectIntensity” module) and radial intensity distribution (“MeasureObjectIntensityDistribution” module). LAP2β staining was used to segment nuclei. Signal intensity was quantified from max intensity projection images. Radial intensity distribution of H3K9me2 was quantified from a manually selected z-slice that was in the middle of the nucleus. Output values were processed with RStudio and graphed with Prism.

Transmission Electron Microscopy and Image Analysis

mESCs were seeded at density of approximately 4.21×10^4 cells/cm² on 18mm circular coverslips coated with Geltrex (Gibco™ A1413202) in a 12-well dish. EpiLC differentiation was stopped after 32 hours. Cells were fixed in Karnovsky’s fixative: 2% Glutaraldehyde (EMS Cat# 16000) and 4% Formaldehyde (EMS Cat# 15700) in 0.1M Sodium Cacodylate (EMS Cat# 12300) pH 7.4 for 1 hour, chilled and sent to Stanford’s CSIF on ice. They were then post-fixed in cold 1% Osmium tetroxide (EMS Cat# 19100) in water and allowed to warm for 2 hours in a hood, washed 3X with ultra-filtered water, then en bloc stained 2 hours in 1% Uranyl Acetate at RT. Samples were then dehydrated in a series of ethanol washes for 10 minutes each at RT beginning at 30%, 50%, 70%, 95%, changed to 100% 2X, then Propylene Oxide (PO) for 10 minutes. Samples are infiltrated with EMBED-812 resin (EMS Cat#14120) mixed 1:1, and 2:1

with PO for 2 hours each. The samples are then placed into EMbed-812 for 2 hours opened then placed into flat molds with labels and fresh resin and placed into 65C oven overnight. Cells of interest were located using the grid pattern and cut out with a gem saw and remounted on pre-labeled resin blocks with fresh resin and polymerized overnight again. Once full polymerized the glass coverslip is etched away using hydrofluoric acid for 20 minutes. Using the finder grid pattern left behind the block faces were trimmed down allowing for serial sectioning of the cells of interest.

Sections were taken around 90nm, picked up on formvar/Carbon coated slot Cu grids, stained for 40 seconds in 3.5% Uranyl Acetate in 50% Acetone followed by staining in 0.2% Lead Citrate for 6 minutes. Observed in the JEOL JEM-1400 120kV and photos were taken using a Gatan Orius 2k X 2k digital camera.

Electron signal from TEM images were quantified using FIJI¹³⁶. Forty coordinates were each manually selected for regions beneath the nuclear envelope and the nucleoplasm. Using a FIJI macro, a 0.2 μ m x 0.2 μ m square was drawn centered at each coordinate point, and the integrated signal density was measured. Data from the 40 squares were averaged and used to generate the plot for nuclear envelope to nucleoplasm signal ratio.

Data Availability

The GEO accession numbers for the RNA-seq and CUT&RUN data reported in this paper are GSE264599, GSE264602, and GSE264603.

CHAPTER 3:

PRELIMINARY RESULTS, SPECULATIONS, AND FUTURE DIRECTIONS

Abstract

This chapter entails a mix of scientific explorations on the effect of peripheral heterochromatin displacement on nuclear shape, the heterochromatin marks H3K9me3, HP1 α and HP1 β , an attempt at building an inducible LBR degon cell line, and structure-function analysis of key residues in LBR that could play a role in recruitment of H3K9me2 to the nuclear periphery.

Results

Nuclear Size and Shape in Lamin + Lbr KO mESCs

The nuclear lamina gives structural shape to the nucleus. Knockout and knockdown studies of nuclear lamins often result in deformations in nuclear shape⁴. Additionally, studies in mouse cells lacking peripheral heterochromatin show that their nuclei tend to be smaller in size compared to cells that have peripheral heterochromatin¹³⁷. To study how heterochromatin position affects nuclear size and shape in stem cells, we reanalyzed immunofluorescence data from wildtype (WT), lamin triple knockout (TKO), LBR knockout (LBR KO), and lamin + Lbr quadruple knockout (QKO) mESCs in Figure 1, Chapter 2. This analysis shows two different results in nuclear size and shape. When cells are plated for 8 hours, there are no significant changes in nuclear size between mutant genotypes compared to WT (Fig 1A-B). As mESCs differentiate to EpiLCs, nuclear size significantly increases but only in the mutant cell lines (Figure 1B). EpiLC nuclei are less circular than their mESC counterpart except for LBR KO cells (Fig. 1C). EpiLC nuclei tend to become more elliptical in shape but only QKO EpiLCs were significantly more elliptical than their mESC counterpart (Fig. 1D). Nuclei are segmented by LAP2 β staining for this analysis, but DNA staining gives similar results in terms of nuclear cross-sectional area (Fig 1E-F). We did not have LAP2 β staining in the next set of experiments, so we segmented nuclei by DNA staining. Four separate immunofluorescence experiments were

performed. Each experiment pertains to a different set of wells in a 96-well imaging dish, and each experiment was imaged on separate days. Experiment 1 and 2 were performed five months apart from experiments 3 and 4. When cells are plated for 24 hours, we observe significant changes in nuclear size in mutant genotypes compared to WT (Fig 2A). Since mESCs tend to grow in colonies after plating for 24 hours, segmentation yielded many clumped objects falsely called as nuclei. Properly segmented nuclei were filtered by having a circularity value above 0.7; however, this meant we could not fully assess changes in nuclei shape (Fig 2B). Nuclear size measurements varied among experiments except for QKO mESCs which consistently showed a significant decrease in cross-sectional area compared to WT (Fig 2A).

Measurements of H3K9me3, HP1 α And HP1 β foci in Lamin + Lbr Knockout mESCs

Since we observed changes to H3K9me2 localization in QKO mESCs (Figure 1 Chapter 2), we wondered if there would be changes in the localization of a chemically similar modification, H3K9me3. To this end, we performed H3K9me3 immunofluorescence. H3K9me3 localizes to pericentromeric DNA and can be visualized as bright foci in mESCs. In rod photoreceptor cells of nocturnal mammals, heterochromatin coalesces to one focus at the center of the nucleus and it is marked by H3K9me3¹⁵. H3K9me2 and H3K9me3 are also bound by heterochromatin proteins HP1 α and HP1 β ^{26,27}. We performed immunofluorescence of H3K9me3, HP1 α and HP1 β in WT, TKO, LBR KO, and QKO mESCs to look at their distribution after release of peripheral heterochromatin (Fig 3 and 4). Since our LAP2 β antibody would cross-react with our H3K9me3 antibody, we could not use it as a nuclear envelope marker, so we used DNA to segment nuclei. We generated max intensity projection images and implemented a 2-D speckles pipeline using CellProfiler to identify H3K9me3, HP1 α and HP1 β foci per nucleus and perform count, size and shape measurements. Compared to WT, the number of H3K9me3 and HP1 β foci per nucleus did not change significantly in all mutant genotypes (Fig 3A, 4D), while in two out of three experiments, the number of HP1 α foci per nucleus significantly decreased in QKO mESCs in two out of three experiments (Fig 3A).

Consistently across experiments, compared to WT, there was no significant difference in the cross-sectional area of HP1 α and HP1 β foci per nucleus in all mutant genotypes (Fig 4B, 4E). Compared to WT, there were inconsistent results between experiments in the size of H3K9me3 foci per nucleus in TKO and LBR KO, but QKO remained consistently unchanged (Fig 3B). The mean intensity per focus was analyzed by measuring the mean intensity per pixel in foci and in their parent nucleus (including foci), then taking the ratio of foci to nucleus. H3K9me3 and HP1 α have very bright foci which yield ratio values greater than 1 (Fig 3C and 4C) while HP1 β foci are not as bright (Fig 4F). This analysis yielded inconsistent results for H3K9me3 foci intensity, especially for QKO mESCs which show a significant decrease in experiment 2 and a significant increase in experiment 3 (Fig. 3C). This analysis showed a consistent increase in HP1 α signal in LBR KO clone 1B4 and QKO mESCs (Fig 4C). As for HP1 β , the only consistent finding was an increase in signal in QKO mESCs (Fig 4F).

Tagging the Endogenous Locus of LBR with the dTAG Degron System

Acute depletion of LBR by RNAi in lamin TKO mESCs leads to changes in H3K9me2 localization and gene expression (Supplemental figure 3 Chapter 2). However, the timing of LBR depletion is not fast enough to explore immediate consequences of peripheral heterochromatin displacement such as effects within one cell cycle. To this end, we made an inducible LBR degron cell line in WT and TKO background mESCs. We set out to tag LBR at the endogenous locus with the dTAG degron system¹³⁸. First, we tagged the dTAG degron cassette to the N-terminus of LBR (see methods) and observed rapid depletion of LBR protein after addition of dTAG-13 within an hour (Fig 5A). Western blotting showed less LBR protein in the edited cell line compared to the parental TKO cell line, even in the absence of dTAG-13. We performed immunofluorescence for H3K9me2 and observed peripheral localization of H3K9me2 before and after LBR depletion in WT background mESCs which agrees with our knockout data (Figure 1 Chapter 2, Fig 5B). However, H3K9me2 displayed less peripheral localization in TKO mESC background before the addition of dTAG-13 (Fig 5C). This was observed in two additional clonal

lines (Fig 5D). We tried C-terminal tagging of the dTAG degron system (see methods). However, this approach did not lead to degradation of LBR after addition of dTAG-13 (data not shown).

H3K9me2 Radial Distribution Rescued by Different LBR Constructs

Peripheral displacement of H3K9me2 is reversible by exogenous expression of LBR (Figure 1 Chapter 2). LBR has a chromatin binding domain, Tudor, and a sterol reductase domain in its transmembrane domain¹⁸. These domains may play a role in heterochromatin recruitment to the periphery either by chromatin binding or modifying the lipid environment of the inner nuclear membrane. To test whether these domains played a role in H3K9me2 positioning, we generated stable QKO mESCs that constitutively expressed Halo-tagged LBR constructs harboring different truncations and point mutations, then performed immunofluorescence for H3K9me2 (Fig 6A). Radial intensity analysis showed different degrees of peripheral H3K9me2 rescue. QKO mESCs expressing either full length LBR (QKO Halo-LBR) or LBR with a catalytically dead sterol reductase mutation¹³⁹ (QKO Halo-LBR^{N558D}) recovered significant peripheral H3K9me2 enrichment but not to the degree of lamin TKO mESCs in the second and third to last peripheral shell. QKO mESCs expressing either the nucleoplasmic domain of LBR (Halo-LBR^{NP}) or LBR with two point mutations in the aromatic cage of its Tudor domain²³ (Halo-LBR^{W16A-Y23A}) did not rescue peripheral H3K9me2 enrichment to the degree of lamin TKO mESCs, but they did rescue better than a nuclear localized Halo peptide (Halo-NLS) (Fig 6B-D).

Discussion, Speculations and Future Directions

Preliminary analysis of nuclear cross-sectional area in lamin + LBR quadruple mESCs shows contradictory results between two independent experiments that might be explained by time of cell plating before fixation. The nucleus is connected to forces in the cytoskeleton by the LINC complex¹⁴⁰. Nuclear size might not change in cells that were recently plated (8 hours) because cells are still in the process of attaching to their dish and cytoskeletal forces might be minimal on the nucleus. Data from figure 1 was used to quantify H3K9me2 radial distribution, and isolated cells are ideal for this type of analysis; however, one of the primary characteristics

of mESCs is that they grow in clumps of colonies. Mutant mESCs that were plated for 24 hours and allowed to grow into colonies showed a significant decrease in nuclear cross-sectional area (Fig 2A). This might represent a more accurate depiction of nuclear size since the cells are at steady state. Another difference between experiments that could influence cell and nuclear shape is the use of Geltrex (Fig. 1) which is a higher attachment substrate than gelatin (Fig. 2). One caveat is the use of DNA as a mask for image analysis for mutant cells that have lost peripheral heterochromatin (QKO). Future experiments could use LAP2 β instead of DNA to mark the nuclear boundary, and future analysis could explore 3-dimensional measurements such as nuclear volume and surface area.

In mouse cells that do not have peripheral heterochromatin, regions of dense heterochromatin called chromocenters coalesce to one focus, and they are also marked by H3K9me3¹⁴¹. Our analysis of H3K9me3 foci in QKO mESCs does not show a decrease in foci number nor an increase in size (Fig 3A-B). Although peripheral heterochromatin is released in QKO mESCs, the rapid doubling time of mESCs might prevent heterochromatin to fully converge into one focus. Our analysis of HP1 α and HP1 β foci in QKO mESCs also does not show a decrease in foci number nor increase in size (Fig 4A-B, 4D-E), also for the same reason as H3K9me3. Our analysis of HP1 α and HP1 β intensity in QKO mESCs, however, shows a consistent increase in signal (Fig 4C 4D). Additional experiments with our inducible LBR RNAi system could validate these findings and further explore if these changes are on the same timescale as H3K9me2 displacement.

Degron tagging of LBR without basal degradation will require a systematic approach at cell editing. Our data shows that it is possible to target both alleles of LBR with the dTAG system and induce rapid degradation (Fig. 5A). Three factors alone or in combination could explain why LBR protein levels were lowered after gene editing. 1. It might be that a double stranded break from CRISPR/Cas9 editing so close to the endogenous promoter disrupted transcriptional output after DNA repair and homologous recombination. 2. Leaky degradation

from the dTAG system. 3. The N-terminal tag could be destabilizing to LBR protein. Future attempts at degron tagging LBR could overcome these challenges by shortening the degron tag from the one that was used (see methods) or use newer, optimized degron systems^{142,143}.

Lastly, we are beginning to tackle the molecular mechanism of how LBR recruits peripheral heterochromatin. We have shown that LBR alone can localize H3K9me2 to the nuclear periphery (Fig. 6). Our preliminary rescue experiments suggest that the sterol reductase activity of LBR is not necessary for it to localize H3K9me2 to the nuclear periphery. Our data also suggests that the methyllysine-binding property of the Tudor domain is necessary for H3K9me2 localization. This suggests an interaction between LBR's Tudor domain and H3K9me2 although it might be indirect. The radial intensity curve for this construct does not look like that of QKO mESCs suggesting a slight partial rescue. This would indicate that other domains in LBR can recruit H3K9me2. Additionally, the nucleoplasmic domain of LBR cannot fully rescue H3K9me2 localization; however, the radial intensity curve looks very much like that of the LBR Tudor double point mutant (Fig 6C). These results suggest that LBR can weakly localize H3K9me2 to the periphery without its transmembrane domain. It is tempting to speculate that nucleoplasmic LBR could weakly interact with another inner nuclear membrane protein and still partially recruit H3K9me2. Lap2 β or Emerin might sound like potential candidates, but these proteins have not been shown to interact with LBR¹⁷. These experiments were performed on a population of cells with varying expression of LBR constructs, although all were positive for the integration of the constructs. Future experiments with clonal lines controlling for LBR levels that resemble that of the parental TKO mESCs will validate these findings. This work will expand our understanding of regions of LBR that are important for recruitment of H3K9me2 to the nuclear periphery and how this affects its roles in gene expression and cell differentiation.

Materials and Methods

Immunofluorescence

Data from figure 1 in this chapter is the same as the one from figure 1 in chapter 2. Immunofluorescence and Halo tag staining for figure 6 was performed as in figure 1 of chapter 2 except Janelia Fluor 552 was used to stain for the Halo tag (see methods for Immunofluorescence and Halo tag staining). Primary antibodies used were H3K9me2 (1:300, abcam ab1220) and LAP2 (1:400, Invitrogen PA5-52519). Secondary antibodies used were anti-rabbit Alexa Fluor 488 (1:1000, Invitrogen A-11008), anti-mouse Alexa Fluor 568 (1:1000, Invitrogen A-11004).

For figures 2-5, 96-well imaging dishes (Thermo Scientific 165305) were coated with gelatin for 30min at 37°C. 1×10^4 cells in 100 μ L media were seeded into each well and allowed to attach in the tissue culture incubator. After approximately 24 hours, mESCs were washed with PBS then fixed with a fresh solution of 4% formaldehyde (Thermo Scientific™ 28908) in PBS for 5 minutes. Cells were washed then stored at 4°C until staining. Fixed cells were permeabilized in immunofluorescence buffer containing 0.1% Triton X-100, 0.02% SDS, 10mg/mL BSA in PBS. Primary and secondary antibodies were diluted in immunofluorescence buffer and incubated at room temperature. For experiments 1 and 2, primary antibody incubation was done for 5 hours, and secondary antibody incubation was done for 1.5 hours. For experiments 3 and 4, primary antibody incubation was done for 2 hours, and secondary antibody incubation was done for 45 minutes. mESCs were washed three times with immunofluorescence buffer between antibody incubations. DNA was stained with Hoechst alongside the secondary antibody incubation. Primary antibodies used were HP1 α (1:1000, Sigma-Aldrich 05-689), H3K9me3 (1:500, abcam ab8898), HP1 β (1:50, abcam ab10811), H3K9me2 (1:1000, ActiveMotif 39041), and LBR (1:1000, abcam ab232731). Secondary antibodies used were anti-mouse IgG Alexa Fluor 488 (1:1000, Invitrogen A-11029), anti-rabbit IgG Alexa Fluor 568 (1:1000, Invitrogen A-11011), and anti-rat IgG Alexa Fluor 647 (1:1000, Invitrogen A-21247, experiment 3 and 4).

Image Acquisition and Analysis

Data from figure 1 in this chapter is the same as the one from figure 1 in chapter 2, and images were acquired in the same way as in chapter 2 (see methods for image acquisition and analysis).

For figures 2-5, FIJI was used for cropping, producing max intensity projections, z-slices and converting raw ND2 images to TIFF files. For figures 2-4, a CellProfiler¹³⁵ pipeline for “Speckle Counting” was downloaded from their website and modified to measure counts, size and signal intensity of H3K9me3, HP1 α , and HP1 β in nuclei and foci. DNA staining was used to segment nuclei. Signal intensity was quantified from max intensity projection images. Output values were processed with RStudio and graphed with Prism.

For figure 6, H3K9me2 radial intensity analysis was performed as in chapter 2 (see methods for Image acquisition and analysis).

Immunoblot assay

Immunoblot assay was carried out as described in Chapter 2 (see immunoblot assay methods). Primary antibodies used were anti-LBR (1:1000, abcam ab232731) and anti-GAPDH (GeneTex, GTX300041). Anti-mouse HRP-conjugated (Rockland 610-1302) and anti-rabbit HRP-conjugated (Rockland 611-1302) secondary antibodies were used at 1:5000 in 5% milk TBST.

Endogenous Tagging of LBR with Inducible dTAG Degron

N-terminal tagging was performed by transient transfection of a px330 CRISPR/Cas9 vector (Addgene 42230) containing a CRISPR guide (5'-CCCTCAACAACTTCCTACT-3') targeting exon 2, near the start codon, of mouse LBR and a repair plasmid containing the dTAG degron cassette which consisted of a selectable marker encoding blasticidin resistance, a T2A ribosome skipping peptide, two HA tags, and the FKBP-V degron peptide sequence, all flanked by homology arms to the endogenous LBR locus. The FKBP-V degron cassette, “BlastR-T2A-2xHA-FKBPV,” was PCR-amplified from a plasmid shared by Elphege Nora’s lab which was

derived from pLEX_305-N-dTAG (addgene # 91797) (fwd primer: 5'-TTTTTCAGACTAATTTTAGAAAATGCCAAGTATGgccaagcctttgtctcaag-3', rev primer: 5'-TCTGACCACTTCACCCTCAACAAACTTCTtgaTGGCATtccggagccacccgaccc-3'). Wildtype mESC genomic DNA was used as template to PCR-amplify the left homology arm (fwd primer: 5'-cgacgttgtaaacgacggccagtTCGCGAAAAGATGTTACAGTTGGAGTAG-3', rev primer: 5'-ggattcttcttgagacaaaggcttggcCATACTTGGCATTCTTCTAAAATTAGTC-3') and the right homology arm (fwd primer: 5'-tcgggscggtggtgggtcgggtggctccggaatgccatcaAGGAAGTTTGTGAGGGTG-3', rev primer: 5'-aacagctatgaccatgattacgccATGCATgaagaggaagagaggatgaag-3'). Capital letters indicate regions that bind the genomic locus except for the ATGCAT sequence, which is an NsiI restriction enzyme site for future cloning of this construct. A synonymous mutation to the third wildtype codon, AGT for Serine-3, was switched to TCA to prevent CRISPR guide from recutting. The repair plasmid was assembled by Gibson cloning into a pUC19 vector. The NGG PAM site was not destroyed. Transfections were performed using the 100µL tips from the Neon electroporation system. One million cells were electroporated with a solution of 2.5µg total CRISPR/Cas9 plasmid and 15µg of repair plasmid. Electroporation settings were 1400V, 10ms, 3 pulses. The edited pool of cells was split sparsely to isolate colonies while undergoing blasticidin selection for a week. Three primers were used to genotype for cassette insertion and heterozygosity (fwd primer: 5'-GATGTATGGAGACTTGCTCAGC-3'; rev primer 1: 5'-GGCCTATACCTCACTCCCATAC-3'; rev primer 2: 5'-TCTTCAGAGATGGGGATGCTGT-3'). "Rev primer 2" targets the blasticidin resistance marker. Expected product(s) for the unedited wildtype locus is 1500bp, for both alleles edited are 1303bp and 2409bp, and for one allele tagged are 1303bp, 1500bp and 2409bp.

C-terminal tagging was performed by transient transfection of a px330 CRISPR/Cas9 vector containing a CRISPR guide (5'-GCACAGGTCAGTAAATGTAG-3') targeting exon 14, near the stop codon, of mouse LBR and a repair plasmid containing the FKBPV degenon fragment and homology arms. A FKBP-V cassette containing "SerGlyLinker-2xHA-FKBPV-

eGFP-T2A-BlastR” for C-terminal tagging was built from a base vector shared by Elphege Nora’s lab and the N-terminal dTAG-LBR donor plasmid. The serine-glycine linker was added in the primers during cloning. This cassette was cloned into a base vector for C-terminal tagging (Buchwalter lab plasmid E00284). Wildtype mESC genomic DNA was used as template to PCR-amplify the left homology arm (fwd primer: 5'-cggccagttcgcgactcgagAAGAATCCCACTGATCCAAAGC-3', rev primer: 5'-gatccaccacctgatccaccGTAAATGTAGGGGAATATGCGG-3') and the right homology arm (fwd primer: 5'-gttatgtgtggagggctaaTGACCTGTGCTGCTTGCCTG-3', rev primer: 5'-attacgccgaattcatgcatACCTGCAAATTGAGGTAGCAAAGC-3'). Capital letters indicate regions that bind the genomic locus. The CRISPR guide covers LBR’s stop codon and thus is destroyed by the tagging strategy. Degradation of tagged LBR was induced by adding dTAG-13 (Sigma-Aldrich SML2601) to the culture media at a final concentration of 500nM.

Figures

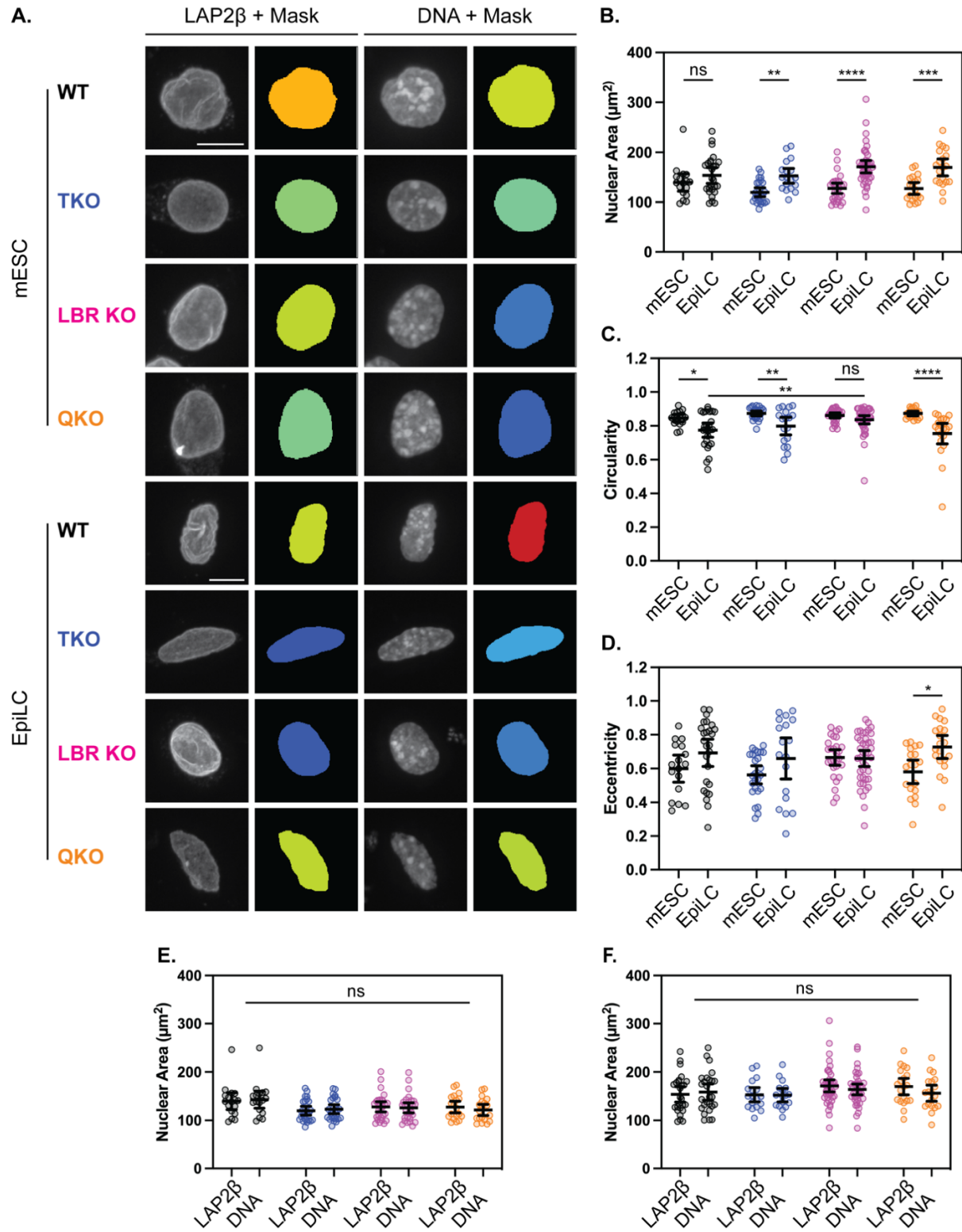


Figure 1 Nuclear shape analysis in Lamins + Lbr KO mESCs and EpiLCs after plating for 8 hours.

(Figure caption continued on the next page.)

(Figure caption continued from the previous page.)

(A) Immunofluorescence of LAP2 β in wildtype (WT) naïve mESCs (n = 17) and EpiLCs (n = 26), Lamin triple knockout (TKO) naïve mESCs (n = 25) and EpiLCs (n = 17), LBR knockout (LBR KO) naïve mESCs (n = 28) and EpiLCs (n = 39), and lamin + Lbr quadruple knockout (QKO) naïve mESCs (n = 19) and EpiLCs (n = 19). Images are max intensity projections. Masks were produced with CellProfiler using LAP2 β or DNA staining. Scale bar (10 μ m). mESCs and EpiLCs have different scaling. **(B-D)** 2-D measurements using LAP2 β masks of nuclear cross-sectional area, circularity, and eccentricity in mESCs and EpiLCs. **(E-F)** Nuclear cross-sectional area in naïve mESCs **(E)** and EpiLCs **(F)** using either LAP2 β or DNA staining as a mask. Points indicate mean and error bars indicate 95% confidence intervals. Two-way ANOVA was performed to compare the mean values followed by pairwise comparison to WT using Dunnett's multiple comparisons test. Genotypes are color coded, WT black, TKO blue, LBR KO magenta, and QKO tangerine. Asterisks denote statistical significance with adjusted p-values, **** p < 0.0001, *** p < 0.001, ** p < 0.01, * p < 0.05, ns not significant. Pairwise comparisons that are not displayed indicate that no significance was found.

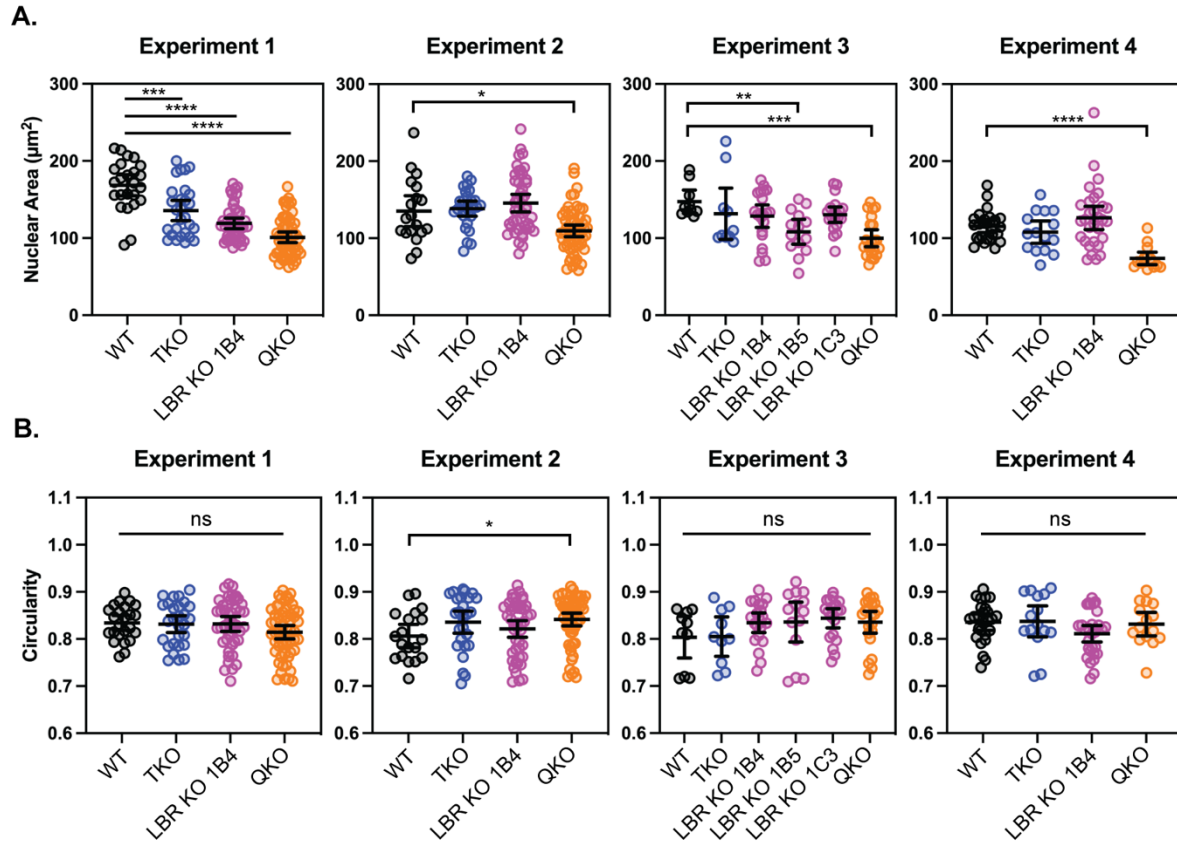


Figure 2 Nuclear shape analysis in Lamins + Lbr KO mESCs after plating for 24 hours.

(A) Nuclear cross-sectional area and **(B)** circularity from four independent immunofluorescence experiments in wildtype (WT), Lamin triple knockout (TKO), LBR knockout (LBR KO), and lamin + Lbr quadruple knockout (QKO) mESCs. Independent isolated LBR KO clones are denoted as 1B4, 1B5, and 1C3. 2-D measurements from max intensity projections using DNA staining to mask the nucleus. Points indicate mean and error bars indicate 95% confidence intervals. Samples sizes, for experiment 1, WT (n = 24), TKO (n = 28), LBR KO 1B4 (n = 45), and QKO (n = 57); for experiment 2, WT (n = 19), TKO (n = 27), LBR KO 1B4 (n = 45), and QKO (n = 57); for experiment 3, WT (n = 10), TKO (n = 10), LBR KO 1B4 (n = 21), LBR KO 1B5 (n = 14), LBR KO 1C3 (n = 20), and QKO (n = 22); for experiment 4, WT (n = 26), TKO (n = 15), LBR KO 1B4 (n = 30), and QKO (n = 15). Two-way ANOVA was performed to compare the mean values followed by pairwise comparison to WT using Dunnett's multiple comparisons test. Genotypes are color coded, WT black, TKO blue, LBR KO magenta, and QKO tangerine. Asterisks denote statistical significance with adjusted p-values, **** p < 0.0001, *** p < 0.001, ** p < 0.01, * p < 0.05, ns not significant. Pairwise comparisons that are not displayed indicate no significant difference.

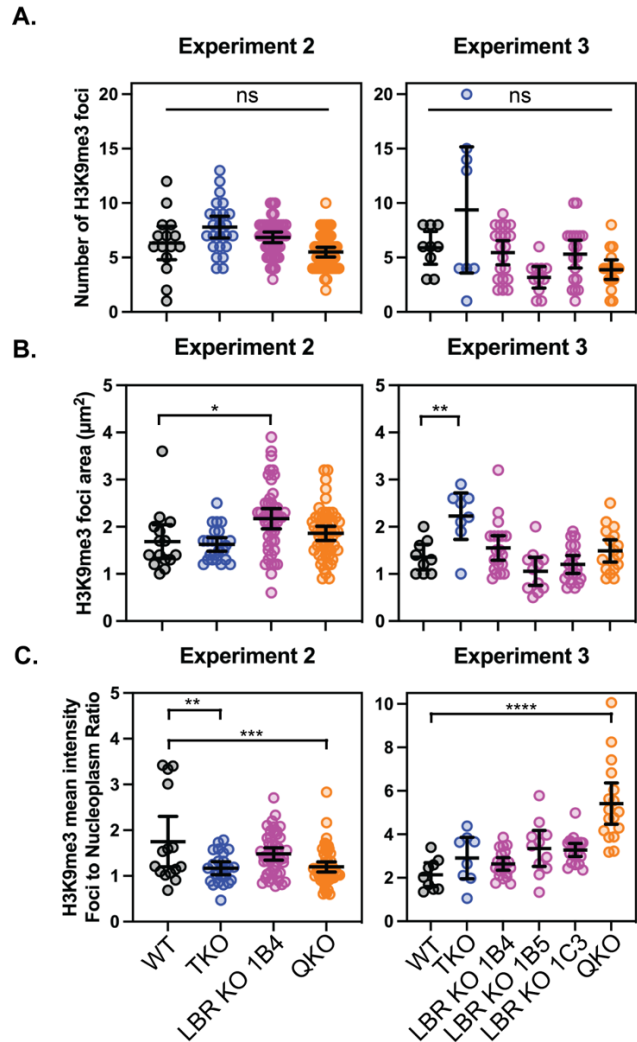
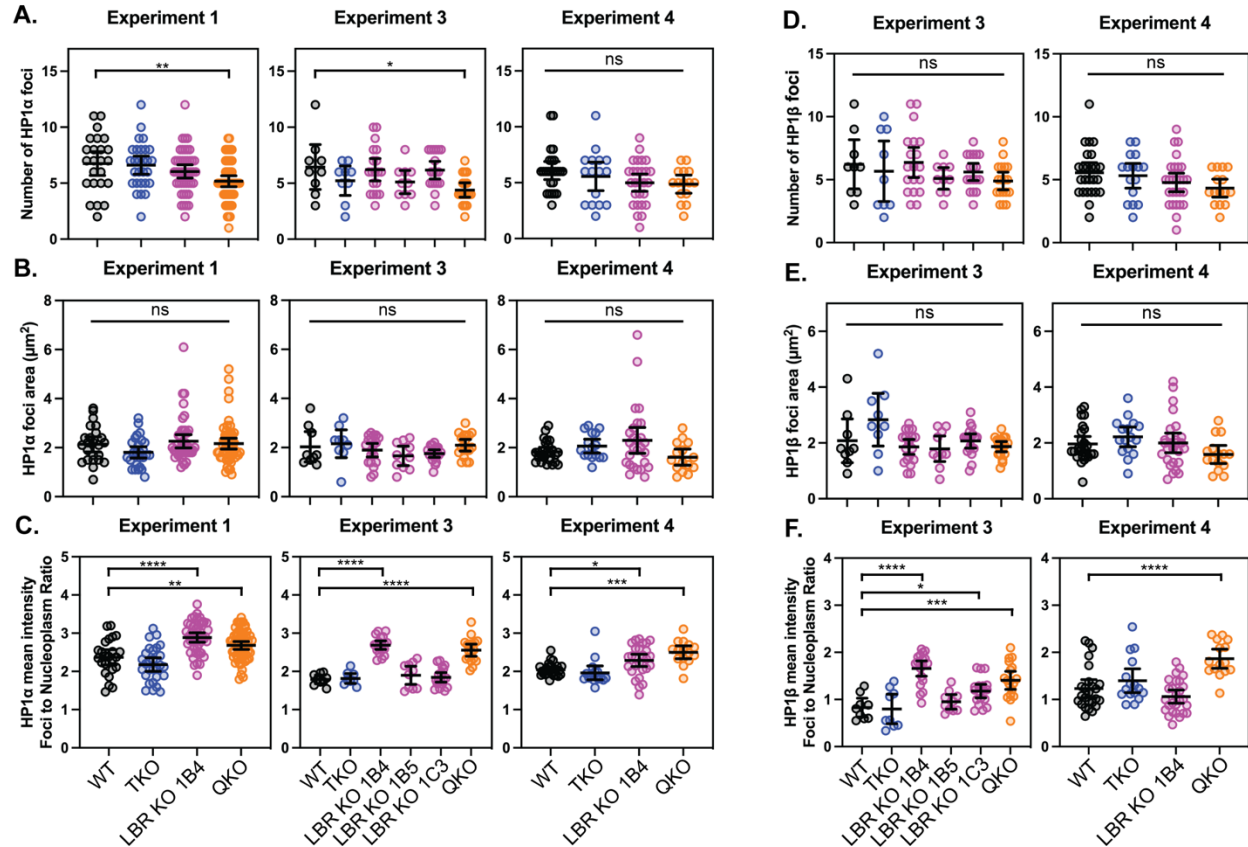


Figure 3 H3K9me3 foci analysis.

(A) Number of H3K9me3 foci per nucleus, **(B)** mean cross-sectional area of H3K9me3 foci per nucleus, and **(C)** mean pixel intensity ratio between foci and nucleoplasm per nucleus from two independent immunofluorescence experiments in wildtype (WT), Lamin triple knockout (TKO), LBR knockout (LBR KO), and lamin + Lbr quadruple knockout (QKO) mESCs. Independent isolated LBR KO clones are denoted as 1B4, 1B5, and 1C3. 2-D measurements from max intensity projections using DNA staining to mask the nucleus. Points indicate mean and error bars indicate 95% confidence intervals. Only nuclei with at least one identified H3K9me3 foci were included. Samples sizes, for experiment 2, WT (n = 15), TKO (n = 24), LBR KO 1B4 (n = 46), and QKO (n = 52); for experiment 3, WT (n = 9), TKO (n = 8), LBR KO 1B4 (n = 20), LBR KO 1B5 (n = 11), LBR KO 1C3 (n = 19), and QKO (n = 17). Two-way ANOVA was performed to compare the mean values followed by pairwise comparison to WT using Dunnett's multiple comparisons test. Genotypes are color coded, WT black, TKO blue, LBR KO magenta, and QKO tangerine. Asterisks denote statistical significance with adjusted p-values, **** $p < 0.0001$, *** $p < 0.001$, ** $p < 0.01$, * $p < 0.05$, ns not significant. Pairwise comparisons that are not displayed indicate that no significance was found.



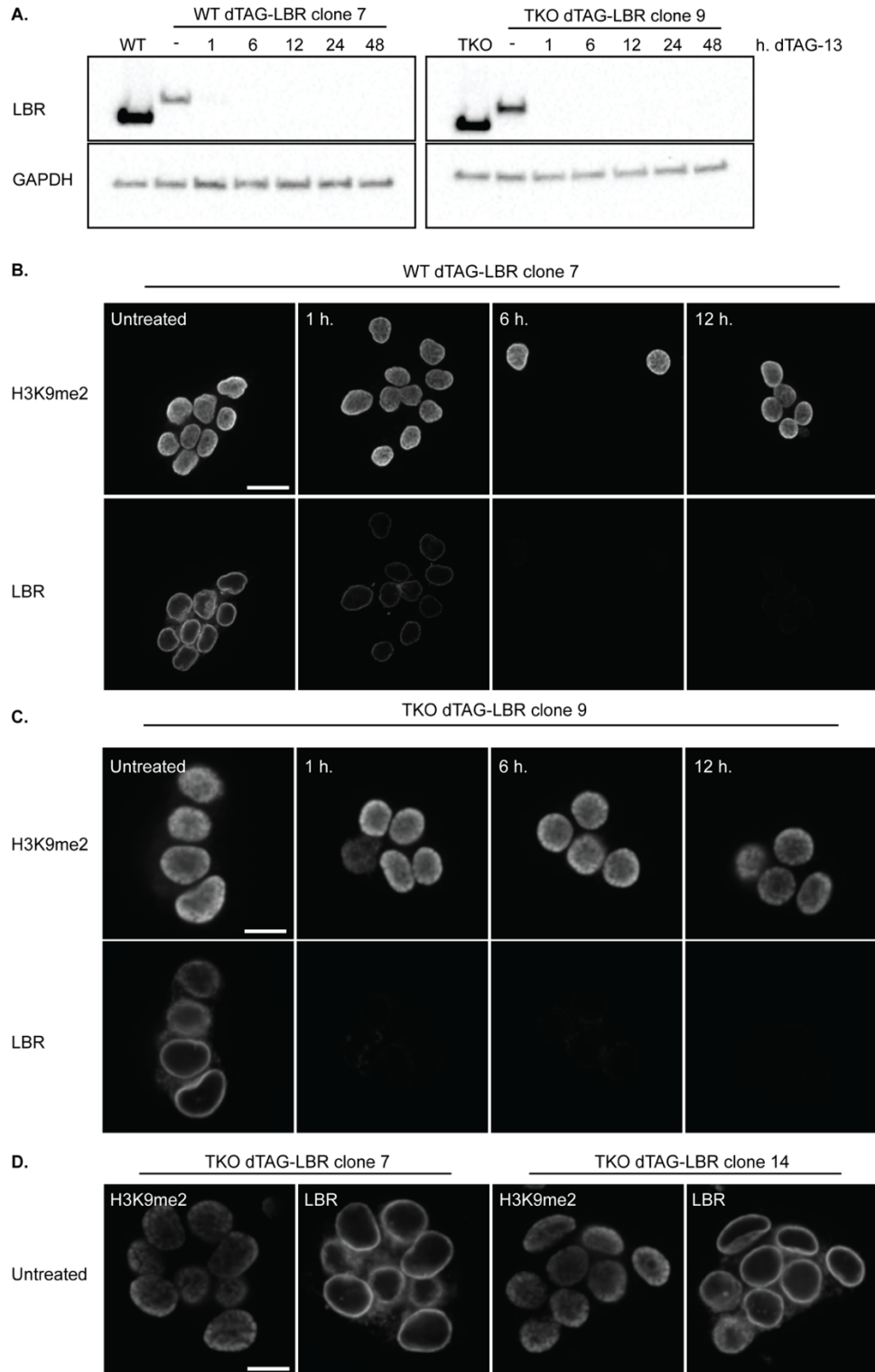


Figure 5 N-terminal tagging of FKBPV degron to the endogenous locus of mouse LBR. (A) Western blot showing time course depletion of FKBPV-LBR in wildtype (WT) and lamin triple knockout (TKO) background mESCs. (B) Immunofluorescence of H3K9me2 and LBR after FKBPV-LBR depletion in an isolated WT clone, and (C) an isolated TKO clone. (D) Immunofluorescence of H3K9me2 and LBR in two different FKBPV-LBR TKO clones, untreated indicates DMSO vehicle control. A central z-slice (XY) is shown. Scale bar 20 μ m.

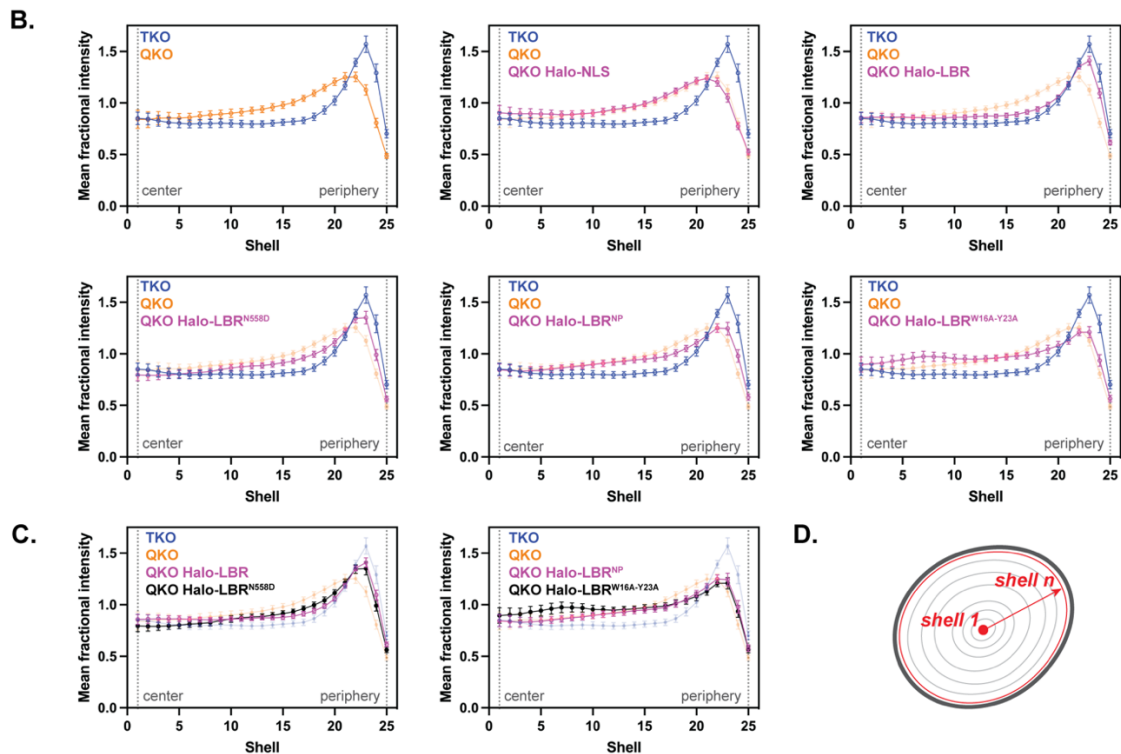
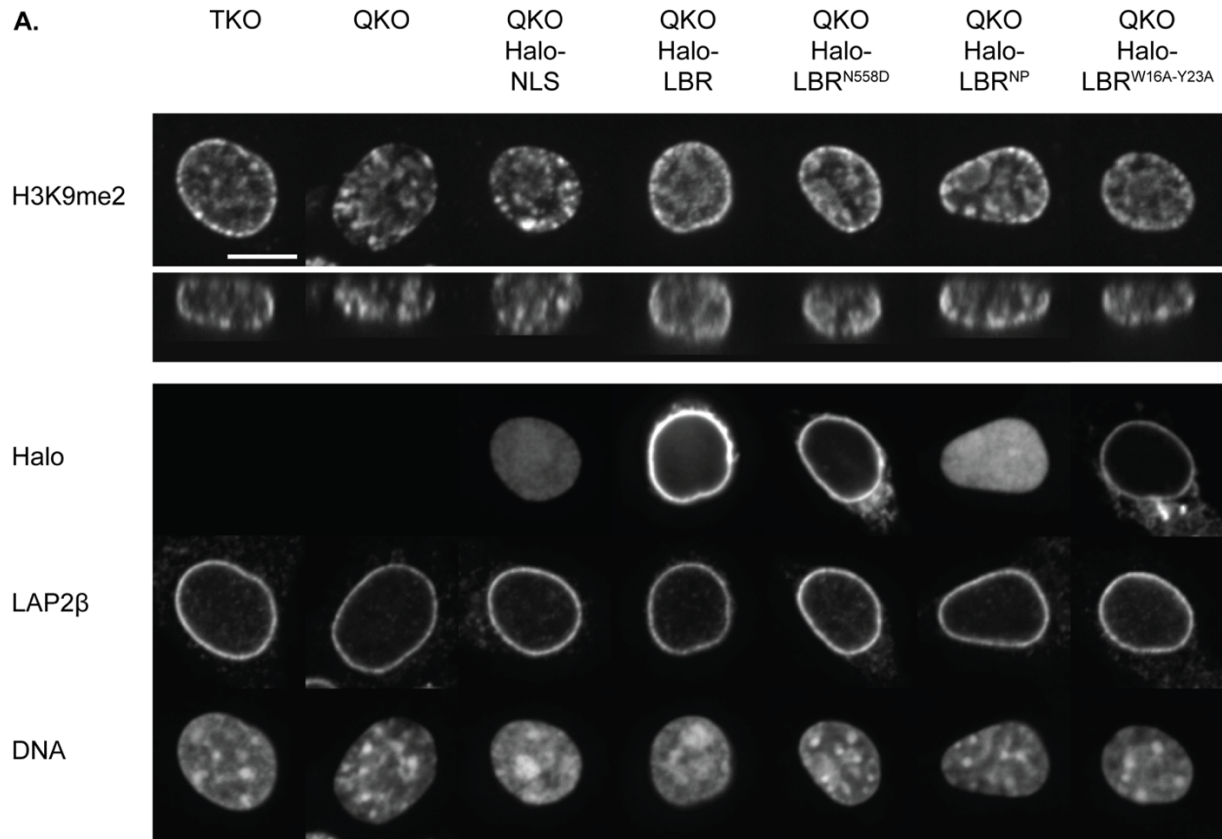


Figure 6 H3K9me2 radial distribution in Lamin + Lbr quadruple knockout mESCs stably expressing different LBR constructs.
 (Figure caption continued on the next page.)

(Figure caption continued from the previous page.)

(A) Immunofluorescence of H3K9me2 localization in Lamin TKO (TKO), Lamin + Lbr quadruple knockout (QKO), and QKO mESCs stably expressing different Halo-tagged constructs such as a nuclear localized signal (Halo-NLS), full-length LBR (Halo-LBR), LBR point mutant in its sterol reductase active site (Halo-LBR^{N558D}), the nucleoplasmic domain of LBR (Halo-LBR^{NP}), and LBR double point mutant in the aromatic cage of its Tudor domain (Halo-LBR^{W16A-Y23A}). A central z-slice (XY) and a central Y-slice (XZ) are shown for H3K9me2. Scale bar, 5 μ m. **(B)** Radial intensity analysis of H3K9me2 position compared to the inner nuclear membrane protein LAP2 β in TKO (n = 36), QKO (n = 38), QKO Halo-NLS (n = 51), QKO Halo-LBR (n = 95), QKO Halo-LBR^{N558D} (n = 75), QKO Halo-LBR^{NP} (n = 56), and QKO Halo-LBR^{W16A-Y23A} (n = 42) mESCs. Two-way ANOVA was performed to compare the mean values at each shell position followed by pairwise comparison to TKO using Dunnett's multiple comparisons test. **** p < 0.0001, TKO vs QKO, shells 14-20, 23-25; **** p < 0.0001, TKO vs QKO Halo-NLS, shells 12-20, 22-25; **** p < 0.0001, TKO vs QKO Halo-LBR, shells 23-24; **** p < 0.0001, TKO vs QKO Halo-LBR^{N558D}, shells 17-18, 23-25; **** p < 0.0001, TKO vs QKO Halo-LBR^{NP}, shells 13-18, 22-24; **** p < 0.0001, TKO vs QKO Halo-LBR^{W16A-Y23A}, shells 6-18, 22-24. **(C)** Radial intensity analysis of H3K9me2 position plots showing QKO Halo-LBR compared to QKO Halo-LBR^{N558D} mESCs, and QKO Halo-LBR^{NP} compared to QKO Halo-LBR^{W16A-Y23A} mESCs. Two-way ANOVA was performed to compare mean values at each shell position followed by Dunnett's multiple comparisons test. **** p < 0.0001, QKO Halo-LBR vs QKO Halo-LBR^{N558D}, shell 24; *** p < 0.001, QKO Halo-LBR^{NP} vs QKO Halo-LBR^{W16A-Y23A}, shell 7. Points indicate mean and error bars indicate 95% confidence intervals. **(D)** Diagram of radial intensity segmentation.

REFERENCES

1. Cutter, A. R. & Hayes, J. J. A brief review of nucleosome structure. *FEBS Lett.* 589, 2914–2922 (2015).
2. Passarge, E. Emil Heitz and the concept of heterochromatin: longitudinal chromosome differentiation was recognized fifty years ago. *Am. J. Hum. Genet.* 31, 106–15 (1979).
3. Cremer, T. et al. Role of Chromosome Territories in the Functional Compartmentalization of the Cell Nucleus. *Cold Spring Harb. Symp. Quant. Biol.* 58, 777–792 (1993).
4. Gruenbaum, Y. & Foisner, R. Lamins: Nuclear Intermediate Filament Proteins with Fundamental Functions in Nuclear Mechanics and Genome Regulation. *Annu. Rev. Biochem.* 84, 1–34 (2015).
5. Hirsch, J. G. & Fedorko, M. E. ULTRASTRUCTURE OF HUMAN LEUKOCYTES AFTER SIMULTANEOUS FIXATION WITH GLUTARALDEHYDE AND OSMIUM TETROXIDE AND “POSTFIXATION” IN URANYL ACETATE. *J. Cell Biol.* 38, 615–627 (1968).
6. Steensel, B. van & Belmont, A. S. Lamina-Associated Domains: Links with Chromosome Architecture, Heterochromatin, and Gene Repression. *Cell* 169, 780–791 (2017).
7. González-Melendi, P. et al. Histones and DNA Ultrastructural Distribution in Plant Cell Nucleus: A Combination of Immunogold and Cytochemical Methods. *Exp. Cell Res.* 242, 45–59 (1998).
8. Krüger, A. et al. Characterization of NE81, the first lamin-like nucleoskeleton protein in a unicellular organism. *Mol. Biol. Cell* 23, 360–370 (2012).
9. Manzo, S. G., Dauban, L. & Steensel, B. van. Lamina-associated domains: Tethers and looseners. *Curr. Opin. Cell Biol.* 74, 80–87 (2022).
10. Marshall, W. F. Order and Disorder in the Nucleus. *Curr. Biol.* 12, R185–R192 (2002).
11. Pickersgill, H. et al. Characterization of the *Drosophila melanogaster* genome at the nuclear lamina. *Nat. Genet.* 38, 1005–1014 (2006).

12. Guelen, L. et al. Domain organization of human chromosomes revealed by mapping of nuclear lamina interactions. *Nature* 453, 948–951 (2008).
13. Poleshko, A. et al. Genome-Nuclear Lamina Interactions Regulate Cardiac Stem Cell Lineage Restriction. *Cell* 171, 573-587.e14 (2017).
14. Peric-Hupkes, D. et al. Molecular Maps of the Reorganization of Genome-Nuclear Lamina Interactions during Differentiation. *Mol. Cell* 38, 603–613 (2010).
15. Solovei, I. et al. LBR and Lamin A/C Sequentially Tether Peripheral Heterochromatin and Inversely Regulate Differentiation. *Cell* 152, 584–598 (2013).
16. Worman, H. J., Yuan, J., Blobel, G. & Georgatos, S. D. A lamin B receptor in the nuclear envelope. *Proc. Natl. Acad. Sci.* 85, 8531–8534 (1988).
17. Olins, A. L., Rhodes, G., Welch, D. B. M., Zwerger, M. & Olins, D. E. Lamin B receptor: multi-tasking at the nuclear envelope. *Nucl. (Austin, Tex)* 1, 53–70 (2009).
18. Nikolakaki, E., Mylonis, I. & Giannakouros, T. Lamin B Receptor: Interplay between Structure, Function and Localization. *Cells* 6, 28 (2017).
19. Lu, R. & Wang, G. G. Tudor: a versatile family of histone methylation ‘readers.’ *Trends Biochem. Sci.* 38, 546–555 (2013).
20. Botuyan, M. V. & Mer, G. Chromatin Signaling and Diseases. Sect. II: Histone Mark Read. 149–165 (2016) doi:10.1016/b978-0-12-802389-1.00008-3.
21. Makatsori, D. et al. The Inner Nuclear Membrane Protein Lamin B Receptor Forms Distinct Microdomains and Links Epigenetically Marked Chromatin to the Nuclear Envelope*. *J. Biol. Chem.* 279, 25567–25573 (2004).
22. Ye, Q. & Worman, H. J. Interaction between an Integral Protein of the Nuclear Envelope Inner Membrane and Human Chromodomain Proteins Homologous to *Drosophila* HP1*. *J. Biol. Chem.* 271, 14653–14656 (1996).
23. Hirano, Y. et al. Lamin B Receptor Recognizes Specific Modifications of Histone H4 in Heterochromatin Formation*. *J. Biol. Chem.* 287, 42654–42663 (2012).

24. Liokatis, S. et al. Solution Structure and Molecular Interactions of Lamin B Receptor Tudor Domain*. *J. Biol. Chem.* 287, 1032–1042 (2012).
25. Ye, Q., Callebaut, I., Pezhman, A., Courvalin, J.-C. & Worman, H. J. Domain-specific Interactions of Human HP1-type Chromodomain Proteins and Inner Nuclear Membrane Protein LBR*. *J. Biol. Chem.* 272, 14983–14989 (1997).
26. Bannister, A. J. et al. Selective recognition of methylated lysine 9 on histone H3 by the HP1 chromo domain. *Nature* 410, 120–124 (2001).
27. Lachner, M., O'Carroll, D., Rea, S., Mechtler, K. & Jenuwein, T. Methylation of histone H3 lysine 9 creates a binding site for HP1 proteins. *Nature* 410, 116–120 (2001).
28. Lechner, M. S., Schultz, D. C., Negorev, D., Maul, G. G. & Rauscher, F. J. The mammalian heterochromatin protein 1 binds diverse nuclear proteins through a common motif that targets the chromoshadow domain. *Biochem. Biophys. Res. Commun.* 331, 929–937 (2005).
29. Paquin, K. L. & Howlett, N. G. Understanding the histone DNA repair code: H4K20me2 makes its mark. *Mol. Cancer Res.* 16, molcanres.0688.2018 (2018).
30. Rea, S. et al. Regulation of chromatin structure by site-specific histone H3 methyltransferases. *Nature* 406, 593–599 (2000).
31. Peters, A. H. F. M. et al. Partitioning and Plasticity of Repressive Histone Methylation States in Mammalian Chromatin. *Mol. Cell* 12, 1577–1589 (2003).
32. Matsui, T. et al. Proviral silencing in embryonic stem cells requires the histone methyltransferase ESET. *Nature* 464, 927–931 (2010).
33. Karimi, M. M. et al. DNA Methylation and SETDB1/H3K9me3 Regulate Predominantly Distinct Sets of Genes, Retroelements, and Chimeric Transcripts in mESCs. *Cell Stem Cell* 8, 676–687 (2011).
34. Falandry, C. et al. CLLD8/KMT1F Is a Lysine Methyltransferase That Is Important for Chromosome Segregation*. *J. Biol. Chem.* 285, 20234–20241 (2010).

35. Tachibana, M. et al. G9a histone methyltransferase plays a dominant role in euchromatic histone H3 lysine 9 methylation and is essential for early embryogenesis. *Genes Dev.* 16, 1779–1791 (2002).
36. Tachibana, M. et al. Histone methyltransferases G9a and GLP form heteromeric complexes and are both crucial for methylation of euchromatin at H3-K9. *Genes Dev.* 19, 815–826 (2005).
37. Peters, A. H. F. M. et al. Loss of the Suv39h Histone Methyltransferases Impairs Mammalian Heterochromatin and Genome Stability. *Cell* 107, 323–337 (2001).
38. Montavon, T. et al. Complete loss of H3K9 methylation dissolves mouse heterochromatin organization. *Nat. Commun.* 12, 4359 (2021).
39. Collins, R. E. et al. In Vitro and in Vivo Analyses of a Phe/Tyr Switch Controlling Product Specificity of Histone Lysine Methyltransferases*. *J. Biol. Chem.* 280, 5563–5570 (2005).
40. Jih, G. et al. Unique roles for histone H3K9me states in RNAi and heritable silencing of transcription. *Nature* 547, 463–467 (2017).
41. Poleshko, A. et al. H3K9me2 orchestrates inheritance of spatial positioning of peripheral heterochromatin through mitosis. *eLife* 8, e49278 (2019).
42. Kind, J. et al. Single-Cell Dynamics of Genome-Nuclear Lamina Interactions. *Cell* 153, 178–192 (2013).
43. See, K. et al. Histone methyltransferase activity programs nuclear peripheral genome positioning. *Dev. Biol.* 466, 90–98 (2020).
44. Padeken, J., Methot, S. P. & Gasser, S. M. Establishment of H3K9-methylated heterochromatin and its functions in tissue differentiation and maintenance. *Nat Rev Mol Cell Biology* 1–18 (2022) doi:10.1038/s41580-022-00483-w.
45. Marshall, W. F., Dernburg, A. F., Harmon, B., Agard, D. A. & Sedat, J. W. Specific interactions of chromatin with the nuclear envelope: positional determination within the nucleus in *Drosophila melanogaster*. *Mol. Biol. Cell* 7, 825–842 (1996).

46. Andrusis, E. D., Neiman, A. M., Zappulla, D. C. & Sternglanz, R. Perinuclear localization of chromatin facilitates transcriptional silencing. *Nature* 394, 592–595 (1998).
47. Croft, J. A. et al. Differences in the Localization and Morphology of Chromosomes in the Human Nucleus. *J. Cell Biol.* 145, 1119–1131 (1999).
48. Falk, M. et al. Heterochromatin drives compartmentalization of inverted and conventional nuclei. *Nature* 570, 395–399 (2019).
49. Borsos, M. et al. Genome–lamina interactions are established de novo in the early mouse embryo. *Nature* 1–21 (2019).
50. Holla, S. et al. Positioning Heterochromatin at the Nuclear Periphery Suppresses Histone Turnover to Promote Epigenetic Inheritance. *Cell* 1–31 (2019).
51. Reddy, K. L., Zullo, J. M., Bertolino, E. & Singh, H. Transcriptional repression mediated by repositioning of genes to the nuclear lamina. *Nature* 452, 243–247 (2008).
52. Zullo, J. M. et al. DNA Sequence-Dependent Compartmentalization and Silencing of Chromatin at the Nuclear Lamina. *Cell* 149, 1474–1487 (2012).
53. Wang, H. et al. CRISPR-Mediated Programmable 3D Genome Positioning and Nuclear Organization. *Cell* 175, 1405–1417.e14 (2018).
54. Guelen, L. et al. Domain organization of human chromosomes revealed by mapping of nuclear lamina interactions. *Nature* 453, 948–951 (2008).
55. Peric-Hupkes, D. et al. Molecular Maps of the Reorganization of Genome-Nuclear Lamina Interactions during Differentiation. *Molecular Cell* 38, 603–613 (2010).
56. Gonzalez-Sandoval, A. et al. Perinuclear Anchoring of H3K9-Methylated Chromatin Stabilizes Induced Cell Fate in *C. elegans* Embryos. *Cell* 163, 1333–1347 (2015).
57. Poleshko, A. et al. Genome-Nuclear Lamina Interactions Regulate Cardiac Stem Cell Lineage Restriction. *Cell* 171, 573–580.e14 (2017).
58. Poleshko, A. et al. H3K9me2 orchestrates inheritance of spatial positioning of peripheral heterochromatin through mitosis. *eLife* 8, 61 (2019).

59. See, K. et al. Histone methyltransferase activity programs nuclear peripheral genome positioning. *Dev Biol* 466, 90–98 (2020).
60. Towbin, B. D. et al. Step-Wise Methylation of Histone H3K9 Positions Heterochromatin at the Nuclear Periphery. *Cell* 150, 934–947 (2012).
61. Kind, J. et al. Single-Cell Dynamics of Genome-Nuclear Lamina Interactions. *Cell* 153, 178–192 (2013).
62. Tachibana, M. et al. G9a histone methyltransferase plays a dominant role in euchromatic histone H3 lysine 9 methylation and is essential for early embryogenesis. *Gene Dev* 16, 1779–1791 (2002).
63. Tachibana, M. et al. Histone methyltransferases G9a and GLP form heteromeric complexes and are both crucial for methylation of euchromatin at H3-K9. *Gene Dev* 19, 815–826 (2005).
64. Leung, D. C. et al. Lysine methyltransferase G9a is required for de novo DNA methylation and the establishment, but not the maintenance, of proviral silencing. *Proc. Natl. Acad. Sci.* 108, 5718–5723 (2011).
65. Macfarlan, T. S. et al. Embryonic stem cell potency fluctuates with endogenous retrovirus activity. *Nature* 487, 57–63 (2012).
66. Maksakova, I. A. et al. Distinct roles of KAP1, HP1 and G9a/GLP in silencing of the two-cell-specific retrotransposon MERVL in mouse ES cells. *Epigenetics Chromatin* 6, 15 (2013).
67. Zyllicz, J. J. et al. Chromatin dynamics and the role of G9a in gene regulation and enhancer silencing during early mouse development. *eLife* 4, e09571 (2015).
68. Jiang, Q. et al. G9a Plays Distinct Roles in Maintaining DNA Methylation, Retrotransposon Silencing, and Chromatin Looping. *Cell Reports* 33, 108315 (2020).
69. Jih, G. et al. Unique roles for histone H3K9me states in RNAi and heritable silencing of transcription. *Nature* 547, 463–467 (2017).

70. Smith, C. L., Poleshko, A. & Epstein, J. A. The nuclear periphery is a scaffold for tissue-specific enhancers. *Nucleic Acids Res.* 49, gkab392- (2021).
71. Smith, C. L., Lan, Y., Jain, R., Epstein, J. A. & Poleshko, A. Global chromatin relabeling accompanies spatial inversion of chromatin in rod photoreceptors. *Sci. Adv.* 7, eabj3035 (2021).
72. Cabianca, D. S. et al. Active chromatin marks drive spatial sequestration of heterochromatin in *C. elegans* nuclei. *Nature Publishing Group* 1–20 (2019).
73. Solovei, I. et al. LBR and Lamin A/C Sequentially Tether Peripheral Heterochromatin and Inversely Regulate Differentiation. *Cell* 152, 584–598 (2013).
74. Wu, R., Terry, A. V., Singh, P. B. & Gilbert, D. M. Differential Subnuclear Localization and Replication Timing of Histone H3 Lysine 9 Methylation States. *Mol. Biol. Cell* 16, 2872–2881 (2005).
75. Yokochi, T. et al. G9a selectively represses a class of late-replicating genes at the nuclear periphery. *Proc. Natl. Acad. Sci.* 106, 19363–19368 (2009).
76. Shah, P. P. et al. An atlas of lamina-associated chromatin across twelve human cell types reveals an intermediate chromatin subtype. *Genome Biol* 24, 16 (2023).
77. Kim, Y., Zheng, X. & Zheng, Y. Proliferation and differentiation of mouse embryonic stem cells lacking all lamins. *Nature Publishing Group* 23, 1420–1423 (2013).
78. Amendola, M. & Steensel, B. Nuclear lamins are not required for lamina-associated domain organization in mouse embryonic stem cells. *Embo Rep* 16, 610–617 (2015).
79. Zheng, X. et al. Lamins Organize the Global Three-Dimensional Genome from the Nuclear Periphery. *Mol Cell* 71, 802-815.e7 (2018).
80. Fellmann, C. et al. An Optimized microRNA Backbone for Effective Single-Copy RNAi. *CellReports* 5, 1704–1713 (2013).
81. Skene, P. J. & Henikoff, S. An efficient targeted nuclease strategy for high-resolution mapping of DNA binding sites. *eLife* 6, e21856 (2017).

82. Spracklin, G. & Pradhan, S. Protect-seq: genome-wide profiling of nuclease inaccessible domains reveals physical properties of chromatin. *Nucleic Acids Res.* 48, e16–e16 (2020).
83. Finlan, L. E. et al. Recruitment to the Nuclear Periphery Can Alter Expression of Genes in Human Cells. *PLoS Genet.* 4, e1000039 (2008).
84. Leemans, C. et al. Promoter-Intrinsic and Local Chromatin Features Determine Gene Repression in LADs. *Cell* 177, 852-864.e14 (2019).
85. Kosak, S. T. et al. Subnuclear Compartmentalization of Immunoglobulin Loci During Lymphocyte Development. *Science* 296, 158–162 (2002).
86. Therizols, P. et al. Chromatin decondensation is sufficient to alter nuclear organization in embryonic stem cells. *Science* 346, 1238–1242 (2014).
87. Meuleman, W. et al. Constitutive nuclear lamina–genome interactions are highly conserved and associated with A/T-rich sequence. *Genome Res.* 23, 270–280 (2013).
88. Jin, Y., Tam, O. H., Paniagua, E. & Hammell, M. Tetrascripts: a package for including transposable elements in differential expression analysis of RNA-seq datasets. *Bioinformatics* 31, 3593–3599 (2015).
89. Sookdeo, A., Hepp, C. M., McClure, M. A. & Boissinot, S. Revisiting the evolution of mouse LINE-1 in the genomic era. *Mob. DNA* 4, 3 (2013).
90. Karimi, M. M. et al. DNA Methylation and SETDB1/H3K9me3 Regulate Predominantly Distinct Sets of Genes, Retroelements, and Chimeric Transcripts in mESCs. *Cell Stem Cell* 8, 676–687 (2011).
91. Montavon, T. et al. Complete loss of H3K9 methylation dissolves mouse heterochromatin organization. *Nat. Commun.* 12, 4359 (2021).
92. Wen, B., Wu, H., Shinkai, Y., Irizarry, R. A. & Feinberg, A. P. Large histone H3 lysine 9 dimethylated chromatin blocks distinguish differentiated from embryonic stem cells. *Nature Genetics* 41, 246–250 (2009).

93. Hayashi, K., Ohta, H., Kurimoto, K., Aramaki, S. & Saitou, M. Reconstitution of the Mouse Germ Cell Specification Pathway in Culture by Pluripotent Stem Cells. *Cell* 146, 519–532 (2011).
94. Buecker, C. et al. Reorganization of Enhancer Patterns in Transition from Naive to Primed Pluripotency. *Cell Stem Cell* 14, 838–853 (2014).
95. Holmer, L., Pezhman, A. & Worman, H. J. The Human Lamin B Receptor/Sterol Reductase Multigene Family. *Genomics* 54, 469–476 (1998).
96. Kalukula, Y., Stephens, A. D., Lammerding, J. & Gabriele, S. Mechanics and functional consequences of nuclear deformations. *Nat. Rev. Mol. Cell Biol.* 23, 583–602 (2022).
97. Cuellar, T. L. et al. Silencing of retrotransposons by SETDB1 inhibits the interferon response in acute myeloid leukemia. *J. Cell Biol.* 216, 3535–3549 (2017).
98. Chiappinelli, K. B. et al. Inhibiting DNA Methylation Causes an Interferon Response in Cancer via dsRNA Including Endogenous Retroviruses. *Cell* 162, 974–986 (2015).
99. Yap, G. L. R. et al. Annexin-A1 promotes RIG-I-dependent signaling and apoptosis via regulation of the IRF3–IFNAR–STAT1–IFIT1 pathway in A549 lung epithelial cells. *Cell Death Dis.* 11, 463 (2020).
100. Piliszek, A. E., Plusa, B., Frankenberg, S., Artus, J. & Hadjantonakis, A.-K. Distinct sequential cell behaviours direct primitive endoderm formation in the mouse blastocyst. *Dev. Biol.* 319, 537–538 (2008).
101. Chazaud, C., Yamanaka, Y., Pawson, T. & Rossant, J. Early Lineage Segregation between Epiblast and Primitive Endoderm in Mouse Blastocysts through the Grb2-MAPK Pathway. *Dev. Cell* 10, 615–624 (2006).
102. Clowney, E. J. et al. Nuclear Aggregation of Olfactory Receptor Genes Governs Their Monogenic Expression. *Cell* 151, 724–737 (2012).
103. Wang, Y. et al. Lamin A/C-dependent chromatin architecture safeguards naïve pluripotency to prevent aberrant cardiovascular cell fate and function. *Nat. Commun.* 13, 6663 (2022).

104. Poleshko, A. et al. The Human Protein PRR14 Tethers Heterochromatin to the Nuclear Lamina during Interphase and Mitotic Exit. *CellReports* 5, 292–301 (2013).
105. Robson, M. I. et al. Tissue-Specific Gene Repositioning by Muscle Nuclear Membrane Proteins Enhances Repression of Critical Developmental Genes during Myogenesis. *Mol. Cell* 62, 834–847 (2016).
106. Ye, Q., Callebaut, I., Pezhman, A., Courvalin, J. C. & Worman, H. J. Domain-specific interactions of human HP1-type chromodomain proteins and inner nuclear membrane protein LBR. *Journal of Biological Chemistry* 272, 14983–14989 (1997).
107. Liokatis, S. et al. Solution Structure and Molecular Interactions of Lamin B Receptor Tudor Domain*. *J Biol Chem* 287, 1032–1042 (2012).
108. Hirano, Y. et al. Lamin B Receptor Recognizes Specific Modifications of Histone H4 in Heterochromatin Formation*. *J. Biol. Chem.* 287, 42654–42663 (2012).
109. Chen, H., Zheng, X., Xiao, D. & Zheng, Y. Age-associated de-repression of retrotransposons in the *Drosophila* fat body, its potential cause and consequence. *Aging Cell* 15, 542–552 (2016).
110. Lenain, C. et al. Massive reshaping of genome–nuclear lamina interactions during oncogene-induced senescence. *Genome Res.* 27, 1634–1644 (2017).
111. Vazquez, B. N. et al. SIRT7 mediates L1 elements transcriptional repression and their association with the nuclear lamina. *Nucleic Acids Res.* 47, 7870–7885 (2019).
112. Valle, F. D. et al. LINE-1 RNA causes heterochromatin erosion and is a target for amelioration of senescent phenotypes in progeroid syndromes. *Sci. Transl. Med.* 14, eabl6057 (2022).
113. Fueyo, R., Judd, J., Feschotte, C. & Wysocka, J. Roles of transposable elements in the regulation of mammalian transcription. *Nat. Rev. Mol. Cell Biol.* 23, 481–497 (2022).
114. Macfarlan, T. S. et al. Endogenous retroviruses and neighboring genes are coordinately repressed by LSD1/KDM1A. *Genes Dev.* 25, 594–607 (2011).

115. Gagnier, L., Belancio, V. P. & Mager, D. L. Mouse germ line mutations due to retrotransposon insertions. *Mob. DNA* 10, 15 (2019).
116. Wang, R. et al. Mouse Embryonic Stem Cells Are Deficient in Type I Interferon Expression in Response to Viral Infections and Double-stranded RNA*. *J. Biol. Chem.* 288, 15926–15936 (2013).
117. Filion, G. J. & Steensel, B. van. Reassessing the abundance of H3K9me2 chromatin domains in embryonic stem cells. *Nat Genet* 42, 4–4 (2010).
118. Kurimoto, K. et al. Quantitative Dynamics of Chromatin Remodeling during Germ Cell Specification from Mouse Embryonic Stem Cells. *Cell Stem Cell* 16, 517–532 (2015).
119. Kim, Y., Zheng, X. & Zheng, Y. Proliferation and differentiation of mouse embryonic stem cells lacking all lamins. *Cell Res.* 23, 1420–3 (2013).
120. Dehairs, J., Talebi, A., Cherifi, Y. & Swinnen, J. V. CRISP-ID: decoding CRISPR mediated indels by Sanger sequencing. *Sci. Rep.* 6, 28973 (2016).
121. Samanta, M. & Kalantry, S. Generating primed pluripotent epiblast stem cells: A methodology chapter. *Curr. Top. Dev. Biol.* 138, 139–174 (2020).
122. Martin, M. Cutadapt removes adapter sequences from high-throughput sequencing reads. *EMBnetJ.* 17, 10–12 (2011).
123. Dobin, A. et al. STAR: ultrafast universal RNA-seq aligner. *Bioinformatics* 29, 15–21 (2013).
124. Danecek, P. et al. Twelve years of SAMtools and BCFtools. *GigaScience* 10, giab008 (2021).
125. Ramírez, F. et al. deepTools2: a next generation web server for deep-sequencing data analysis. *Nucleic Acids Res.* 44, W160–W165 (2016).
126. Liao, Y., Smyth, G. K. & Shi, W. featureCounts: an efficient general purpose program for assigning sequence reads to genomic features. *Bioinformatics* 30, 923–930 (2014).

127. Love, M. I., Huber, W. & Anders, S. Moderated estimation of fold change and dispersion for RNA-seq data with DESeq2. *Genome Biol.* 15, 550 (2014).
128. Jin, Y., Tam, O. H., Paniagua, E. & Hammell, M. TEtranscripts: a package for including transposable elements in differential expression analysis of RNA-seq datasets. *Bioinformatics* 31, 3593–3599 (2015).
129. Reimand, J., Kull, M., Peterson, H., Hansen, J. & Vilo, J. g:Profiler—a web-based toolset for functional profiling of gene lists from large-scale experiments. *Nucleic Acids Res.* 35, W193–W200 (2007).
130. Supek, F., Bošnjak, M., Škunca, N. & Šmuc, T. REVIGO Summarizes and Visualizes Long Lists of Gene Ontology Terms. *PLoS ONE* 6, e21800 (2011).
131. Skene, P. J., Henikoff, J. G. & Henikoff, S. Targeted in situ genome-wide profiling with high efficiency for low cell numbers. *Nat. Protoc.* 13, 1006–1019 (2018).
132. Langmead, B. & Salzberg, S. L. Fast gapped-read alignment with Bowtie 2. *Nat. Methods* 9, 357–359 (2012).
133. Schreiber, J. Pomegranate: fast and flexible probabilistic modeling in python. *arXiv* (2017) doi:10.48550/arxiv.1711.00137.
134. Dale, R. K., Pedersen, B. S. & Quinlan, A. R. Pybedtools: a flexible Python library for manipulating genomic datasets and annotations. *Bioinformatics* 27, 3423–3424 (2011).
135. Stirling, D. R. et al. CellProfiler 4: improvements in speed, utility and usability. *BMC Bioinform.* 22, 433 (2021).
136. Schindelin, J. et al. Fiji: an open-source platform for biological-image analysis. *Nat. Methods* 9, 676–682 (2012).
137. Solovei, I. et al. Nuclear Architecture of Rod Photoreceptor Cells Adapts to Vision in Mammalian Evolution. *Cell* 137, 356–368 (2009).
138. Nabet, B. et al. The dTAG system for immediate and target-specific protein degradation. *Nat. Chem. Biol.* 14, 431–441 (2018).

139. Tsai, P.-L., Zhao, C., Turner, E. & Schlieker, C. The Lamin B receptor is essential for cholesterol synthesis and perturbed by disease-causing mutations. *eLife* 5, e16011 (2016).
140. Chang, W., Worman, H. J. & Gundersen, G. G. Accessorizing and anchoring the LINC complex for multifunctionality. *J. Cell Biol.* 208, 11–22 (2015).
141. Eberhart, A. et al. Epigenetics of eu- and heterochromatin in inverted and conventional nuclei from mouse retina. *Chromosom. Res.* 21, 535–554 (2013).
142. Nabet, B. et al. Rapid and direct control of target protein levels with VHL-recruiting dTAG molecules. *Nat. Commun.* 11, 4687 (2020).
143. Yesbolatova, A. et al. The auxin-inducible degron 2 technology provides sharp degradation control in yeast, mammalian cells, and mice. *Nat. Commun.* 11, 5701 (2020).

Publishing Agreement

It is the policy of the University to encourage open access and broad distribution of all theses, dissertations, and manuscripts. The Graduate Division will facilitate the distribution of UCSF theses, dissertations, and manuscripts to the UCSF Library for open access and distribution. UCSF will make such theses, dissertations, and manuscripts accessible to the public and will take reasonable steps to preserve these works in perpetuity.

I hereby grant the non-exclusive, perpetual right to The Regents of the University of California to reproduce, publicly display, distribute, preserve, and publish copies of my thesis, dissertation, or manuscript in any form or media, now existing or later derived, including access online for teaching, research, and public service purposes.

DocuSigned by:

Harold Cesar Marin

2C090CCC01BF4C4...

Author Signature

5/30/2024

Date